

A new angle on light-sheet microscopy and real-time image processing

Bálint Balázs



Pázmány Péter Catholic University
Faculty of Information Technology and Bionics
Roska Tamás Doctoral School of Sciences and Technology

Advisor: Balázs Rózsa, *M.D., Ph.D.*

A thesis submitted for the degree of
Doctor of Philosophy
2017

Abstract

Light-sheet fluorescence microscopy, also called single plane illumination microscopy, has numerously proven its usefulness for long term imaging of embryonic development. This thesis tackles two challenges of light-sheet microscopy: high resolution isotropic imaging of delicate, light-sensitive samples, and real-time image processing and compression of light-sheet microscopy images.

A symmetric light-sheet microscope is presented, featuring two high numerical aperture objectives arranged in 120°. Both objectives are capable of illuminating the sample with a tilted light-sheet and detecting the fluorescence signal. This configuration allows for multi-view, isotropic imaging of delicate samples where rotation is not possible. The optical properties of the microscope are characterized, and its imaging capabilities are demonstrated on *Drosophila melanogaster* embryos and mouse zygotes.

To address the big data problem of light-sheet microscopy, a real-time, GPU-based image processing pipeline is presented. Alongside its capability of performing commonly required preprocessing tasks, such as image fusion of opposing views immediately during image acquisition, it also contains a novel, high-speed image compression method. This algorithm is suitable for both lossless and noise-dependent lossy image compression, the latter allowing for a significantly increased compression ratio, without affecting the results of any further analysis. A detailed performance analysis is presented of the different compression modes for various biological samples and imaging modalities.

Contents

Abstract	ii
List of Figures	vi
List of Tables	vii
List of Abbreviations	viii
Introduction	1
1 Live imaging in three dimensions	3
1.1 Wide-field fluorescence microscopy	3
1.2 Point scanning methods	10
1.3 Light-sheet microscopy	14
1.4 Light-sheet imaging of mammalian development	21
2 Image compression	29
2.1 Basics of information theory	29
2.2 Entropy coding	30
2.3 Decorrelation	34
3 Dual Mouse-SPIM	38
3.1 Microscope design concept	39
3.2 Optical layout	42
3.3 Optical alignment	47
3.4 Control unit	51
3.5 Results	54
3.6 Methods	62
3.7 Discussion	63

4 GPU-accelerated image processing and compression	66
4.1 Challenges in data handling for light-sheet microscopy	66
4.2 Real-time preprocessing pipeline	67
4.3 B ³ D image compression	76
4.4 Discussion	88
5 Conclusions	90
5.1 New scientific results	90
5.2 Application of the results	92
Appendix	94
A Bill of materials	94
B Supplementary Tables	96
C Light collection efficiency of an objective	98
D 3D model of Dual Mouse-SPIM	99
References	101
Acknowledgements	113

List of Figures

1.1	Tradeoffs in fluorescence microscopy for live imaging	4
1.2	Excitation and emission spectrum of enhanced green fluorescent protein (EGFP)	4
1.3	Wide-field fluorescence microscope	6
1.4	Axial cross section of the PSF and OTF of a wide-field microscope	8
1.5	Airy pattern	9
1.6	Resolution of a wide-field microscope	11
1.7	Basic optical components of a confocal laser scanning and confocal-theta microscope	12
1.8	Axial cross section of the PSF and OTF of a confocal laser scanning microscope	13
1.9	Basic concept of single-plane illumination microscopy	14
1.10	Different optical arrangements for light-sheet microscopy	16
1.11	Basic optical components of a SPIM	17
1.12	Light-sheet dimensions	20
1.13	DSLM illumination	21
1.14	Inverted light-sheet microscope for multiple early mouse embryo imaging.	23
1.15	Imaging mouse post-implantation development	25
1.16	Imaging adult mouse brain with light-sheet microscopy.	26
2.1	Building the binary Huffman tree	33
2.2	Context for pixel prediction	36
3.1	Dual view concept with high NA objectives	39
3.2	Lateral and axial resolution of a multi-view optical system	41
3.3	Dual Mouse-SPIM optical layout	43
3.4	The core unit of the microscope	44
3.5	Illumination branch splitting unit	46
3.6	Detection branch switching unit	48
3.7	Microscope control hardware and software architecture	53

LIST OF FIGURES

3.8	Digital and analog control signals	53
3.9	Completed DualMouse-SPIM	55
3.10	Stability measurements of view switcher unit	56
3.11	Illumination beam profile	57
3.12	Simulated and measured PSF of Dual Mouse-SPIM	58
3.13	Combined PSF of 2 views	59
3.14	Maximum intensity projection of a <i>Drosophila melanogaster</i> embryo recording	60
3.15	Multi-view recording of a mouse zygote	61
4.1	Experiment sizes and data rate of different imaging modalities	67
4.2	Real-time image processing pipeline for multiview light-sheet microscopy	67
4.3	Operating principle of MuVi-SPIM	68
4.4	multiview fusion methods for light-sheet microscopy	70
4.5	Classes of LVCUDA library	71
4.6	Applying mask to remove background	72
4.7	Comparison of 3D and 2D fusion of beads	73
4.8	GPU fused images of a <i>Drosophila melanogaster</i> embryo	75
4.9	Image contrast depending on z position for raw and fused stacks	75
4.10	B ³ D algorithm schematics	78
4.11	Options for noise-dependent lossy compression	80
4.12	Theoretical and measured increase in image noise for WNL compression	81
4.13	Compression performance	82
4.14	Image quality of a WNL compressed dataset	82
4.15	Compression error compared to image noise	83
4.16	Influence of noise-dependent lossy compression on 3D nucleus segmentation	83
4.17	Influence of noise-dependent lossy compression on 3D membrane segmentation	84
4.18	Influence of noise-dependent lossy compression on single-molecule localization	85
4.19	Change in localization error only depends on selected quantization step	85
C1	Light collection efficiency of an objective	98
D1	3D model of DualMouse-SPIM	100

List of Tables

2.1	Examples of a random binary code (#1) and a prefix-free binary code (#2)	31
2.2	Letters to be Huffman coded and their probabilities	32
2.3	Huffman code table	34
B1	Data sizes in microscopy	96
B2	Lossless compression performance	96
B3	Datasets used for benchmarking compression performance	97

List of Abbreviations

2D two-dimensional.

3D three-dimensional.

BFP back focal plane.

CCD charge coupled device.

CLSM confocal laser scanning microscopy.

CMOS complementary metal oxide semiconductor.

CPU central processing unit.

DCT discrete cosine transform.

DFT discrete fourier transform.

DPCM differential pulse code modulation.

DSLM digitally scanned light-sheet microscopy.

dSTORM direct stochastic optical reconstruction microscopy.

DWT discrete wavelet transform.

eCSD electronic confocal slit detection.

EM-CCD electron multiplying CCD.

FEP fluorinated ethylene propylene.

FN field number.

FOV field of view.

FPGA field programmable gate array.

fps frames per second.

FWHM full width at half maximum.

GFP green fluorescent protein.

GPU graphics processing unit.

HEVC high efficiency video codec.

ICM inner cell mass.

JPEG joint photographic experts group.

LSFM light-sheet fluorescence microscopy.

MIAM multi-imaging axis microscopy.

MuVi-SPIM Multiview SPIM.

NA numerical aperture.

OPFOS orthogonal plane fluorescent optical sectioning.

OTF optical transfer function.

PEEK polyether ether ketone.

PSF point spread function.

RESOLFT reversible saturable optical fluorescence transitions.

ROI region of interest.

sCMOS scientific CMOS.

SMLM single molecule localization microscopy.

SNR signal-to-noise ratio.

SPIM single-plane illumination microscopy.

STED stimulated emission depletion.

TE trophoectoderm.

TLSM thin light-sheet microscopy.

WNL within noise level.

YFP yellow fluorescent protein.

Introduction

Imaging techniques are one of the most extensively used tools in medical and biological research. The reason for this is simple: visualizing something invisible to the naked eye is an extremely powerful way to gain insight into its inner workings. Our brain has evolved to receive and process a multitude of signals from various sensors, and arguably the most powerful of these is vision.

As a branch of optics, microscopy (from ancient Greek *mikros*, “small” and *skopein*, “to see”) is based on observing the interactions of light with an object of interest, such as a cell. To be able to see these interactions, the optics of the microscope magnifies the image of the sample, which can be recorded on a suitable device. For the first microscopes in the 17th century, this was just an eye at the end of the ocular, and the recording was a drawing of the observed image [1].

Microscopy is a truly multidisciplinary field: even in its simplest form, just using a single lens, the principles of physics are applied to gain a deeper understanding of biology and nature. Today, microscopy encompasses most of natural sciences and builds on various technological advancements. While physics and biology are still in the main focus, the principles of chemistry (fluorescent molecules), engineering (automation) and computer science (image analysis) are all integrated in a modern microscopy environment.

Light-sheet fluorescence microscopy (LSFM), also called single-plane illumination microscopy (SPIM), is a relatively new addition to the arsenal of tools that comprise light microscopy methods, and is especially suitable for live imaging of embryonic samples over extended periods of time [2–5]. It is also easily adapted to the sample, allowing to image a large variety of specimens, from entire organs [6], to the subcellular processes occurring inside cultured cells [7]. Due to its ability to bridge large scales in space and time, light-sheet microscopy can provide an unprecedented amount of information on biological processes. Despite its indubitable benefits, operating such a microscope can pose serious infrastructural challenges, as a single overnight experiment can generate tens of terabytes of data.

This work tackles two challenges in light-sheet microscopy: high-resolution live imaging of delicate samples, such as mouse embryos, and real-time image processing and compression of large light-sheet datasets. Before discussing the work in detail, Chapter 1

and Chapter 2 will give a short introduction to the concepts this thesis builds on. The basics of fluorescence microscopy, light-sheet microscopy, information theory and image compression will be covered.

Chapter 3 is devoted to presenting a new light-sheet microscope, the Dual Mouse-SPIM, designed for isotropic imaging of light-sensitive specimens. This microscope is based on two identical objectives positioned in 120° as opposed to the conventional 90° orientation used in light-sheet microscopy, and it offers dual-view detection through both lenses. We discuss the benefits of this arrangement and the design principles and optical layout of the microscope. After characterizing the optical properties of the microscope, we demonstrate its imaging capabilities on various samples.

In Chapter 4 we present a GPU-based real-time image processing pipeline designed to efficiently handle large amounts of microscopy data. As 3D imaging is gaining more and more traction, image datasets are generated at a faster pace than ever. We present a real-time preprocessing solution for multiview light-sheet microscopy, and a new image compression algorithm to significantly reduce data size by taking image noise into account. The theory behind these methods will be discussed before demonstrating their capabilities and evaluating their performance on multiple biological samples.

Finally, Chapter 5 will give a summary of the new results presented in this thesis, and discuss the potential future applications.

Chapter 1

Live imaging in three dimensions

Live imaging is indispensable to understand the processes at the interface of cell and developmental biology. In an ideal setting, the ultimate microscope would be able to record a continuous, three dimensional (3D), multicolor dataset of any biological process of interest with the highest possible resolution. Due to several limitations in physics and biology this is not possible. Therefore, a compromise is necessary. The diffractive nature of light, the lifetime of fluorescent probes and the photosensitivity of biological specimens all require microscopy to be adapted so that the question at hand may be answered.

In order to acquire useful data, one has to choose a tradeoff between spatial and temporal resolution and signal contrast, while making sure the biology is not affected by the imaging process itself [8]. This challenge can be illustrated by a pyramid where each corner represents one of these criteria (Figure 1.1), while a point inside the pyramid corresponds to the imaging conditions. As soon as we try to optimize one condition, *i.e.*, we move the point closer to one of the corners, it will move further from all the others due to the limited photon budget. In order to make a fundamental difference and move the corners of the pyramid closer together, a change in microscope design is necessary.

1.1 Wide-field fluorescence microscopy

Fluorescence microscopy [9, 10], as a subset of light microscopy, is one of the few methods that allow subcellular imaging of live specimens with specific labeling. The first use of the term fluorescence is credited to George Gabriel Stokes [11], and it refers to the phenomenon of light emission following the absorption of light or other electromagnetic radiation. As the name fluorescence microscopy suggests, this method collects fluorescent light from the specimens. Since biological tissues are usually not fluorescent, except for some autofluorescence mostly at shorter wavelengths, fluorescent dyes or proteins have to be introduced to the system in order to be able to collect the necessary information. The advantage of this is that the signal of the labeled structures will be of very high

1.1 Wide-field fluorescence microscopy

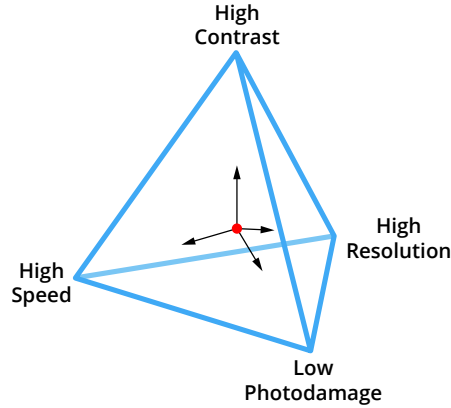


Figure 1.1: Tradeoffs in fluorescence microscopy for live imaging. Also called the “pyramid of frustration”. When optimizing the imaging conditions (red dot), a tradeoff has to be made between resolution, contrast, and imaging speed, while avoiding photodamage. One can only be improved at the expense of the others due to the limited photon budget of the fluorescent molecules. Adapted from [8].

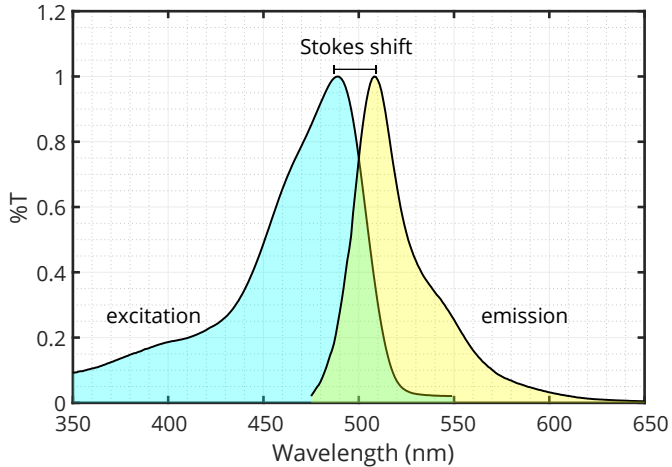


Figure 1.2: Excitation and emission spectrum of enhanced green fluorescent protein (EGFP). Excitation spectrum in blue, emission spectrum in yellow. The separation between the two spectra is due to the Stokes shift, which is 19 nm for EGFP. Emission and excitation light can be separated by a long-pass filter at 500 nm. Data from [12].

ratio compared to the background.

A fluorescent molecule is capable of absorbing photons in a given wavelength range (excitation spectrum) and temporarily store its energy by having an electron in a higher energy state, *i.e.*, in an excited state. This excited state, however, is not stable, and the electron quickly returns to the ground state while emitting a photon. The energy of the absorbed and emitted photons are not the same, as energy loss occurs due to internal relaxation events, and the emitted photon has lower energy than the absorbed photon. This phenomenon is called the Stokes shift, or red shift, and can be exploited in microscopy to drastically increase the signal-to-noise ratio by filtering out the illumination light (Figure 1.2).

1.1.1 Fluorescent proteins

Traditionally, synthetic fluorescent dyes were used to label certain structures in the specimens. Some of these directly bind to their target, and others can be used when conjugated to an antibody specific to the structure or protein of interest. A requirement for these methods is that the fluorescent label has to be added to the sample from an external source, and, in many cases, this also necessitates sample preparation techniques incompatible with live imaging, such as fixation [13].

The discovery of fluorescent proteins has revolutionized fluorescence microscopy. Since these molecules are proteins, they can be produced directly by the organism if the proper genetic modifications are performed. Even though this was a hurdle at the time of discovering the green fluorescent protein (GFP) [14], genetic engineering techniques evolved since then [15], and not only has its gene been successfully integrated in the genome of a multitude of organisms [16–18], but many variants have been also engineered by introducing mutations to increase fluorescence intensity, and to change the fluorescence spectrum to allow multicolor imaging [18–21]. The usefulness and impact of these proteins are so profound, that in 2008 the Nobel Prize in chemistry was awarded to Osamu Shimomura, Martin Chalfie, and Roger Tsien “for the discovery and development of the green fluorescent protein, GFP” [22].

1.1.2 Wide-field image formation

By imaging fluorescently labelled specimens, a wide-field fluorescence microscope has the capability of discriminating illumination light from emitted fluorescent light due to the Stokes shift described in the previous section. The microscope’s operating principle is depicted in Figure 1.3.

Light from a source, typically a mercury lamp is focused on the back focal plane of the objective to create even illumination of the sample. Before entering the objective, the light is filtered, so only the wavelengths that correspond to the excitation properties of the observed fluorophores are transmitted. Since the same objective is used for both illumination and detection, a dichroic mirror is utilized to decouple the illumination and detection paths. The emitted light is filtered again to make sure any reflected and scattered light from the illumination source is blocked to increase signal-to-noise ratio. Finally, light is focused by a tube lens to create a magnified image on the camera sensor.

This type of arrangement is called infinity-corrected optics, since the back focal point of the objective is in “infinity”, meaning that the light from a point source exiting the back aperture is parallel. This is achieved by placing the sample exactly at the focal point of the objective. Infinity-corrected optics have the advantage that they allow placing various additional optical elements in the infinity space, (*i.e.*, the space between the objective and the tube lens) without affecting the image quality. In this example such elements

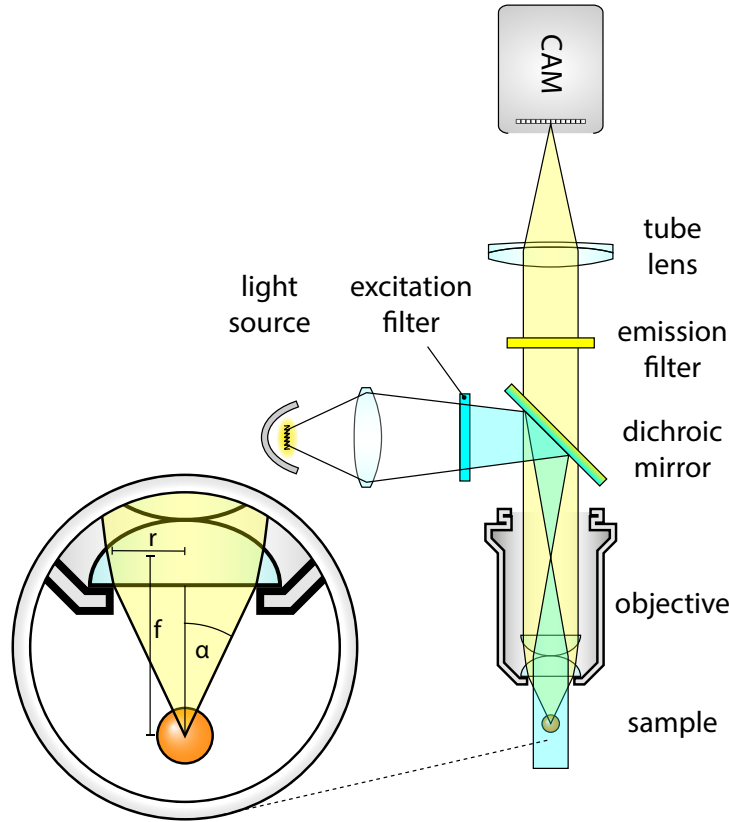


Figure 1.3: Wide-field fluorescence microscope. The light source is focused on the back focal plane of the objective to provide an even illumination to the sample. Emitted photons are collected by the objective, and are separated from the illumination light by a dichroic mirror. Inset: Light collection of an objective lens. α : light collection half-angle; f : focal length; r : radius of aperture.

are the dichroic mirror and the emission filter.

The combination of the objective and tube lens together will determine the optical magnification of the system, which will be the ratio of the focal lengths of these lenses:

$$M = \frac{f_{TL}}{f_{OBJ}}. \quad (1.1)$$

The final field of view (FOV) of the microscope will depend on the magnification, the size of the imaging sensor (D), and the objective field number (FN , specified by the manufacturer, the diameter of the view field in the image plane):

$$FOV = \frac{\min(D, FN)}{M}. \quad (1.2)$$

Apart from the magnification, the most important property of the objective is the half-angle of the light acceptance cone, α (Figure 1.3, inset). This not only determines the amount of collected light, but also the achievable resolution of the system (see Section 1.1.3). This angle depends on the size of the lens relative to its focal length. In other

words it depends on the aperture of the lens, which is why the expression *numerical aperture* (NA) is more commonly used to express this property of the objective:

$$\text{NA} = n \cdot \sin \alpha. \quad (1.3)$$

where n is the refractive index of the medium, and describes the light propagation speed in the medium relative to the speed of light in vacuum. For vacuum and air $n = 1$, for water $n_{\text{H}_2\text{O}} = 1.33$, and for the commonly used optical glass BK7 $n_{\text{BK7}} = 1.52$.

For small α angles, the following approximation holds true: $\sin \alpha \approx \tan \alpha \approx \alpha$. Thus, the numerical aperture can also be expressed as a ratio of the radius of the lens and the focal length:

$$\text{NA} \approx n \frac{r}{f}, \quad \text{when } \alpha \ll 1. \quad (1.4)$$

1.1.3 Resolution of a wide-field microscope

The resolution of an optical system depends on the size of the smallest distinguishable feature on the image. A practical way of quantifying this is by measuring the smallest resolved distance, *i.e.*, the minimum distance between two point-like objects so that the two objects can still be distinguished. This mainly depends on two factors: the NA of the objective, and the pixel size of the imaging sensor.

Even if the imaging sensor would have infinitely fine resolution, it is not possible to reach arbitrarily high resolutions due to the wave nature of light and diffraction effects that occur at the aperture of the objective. This means that depending on the wavelength of the light, any point source will have a finite size on the image, it will be spread out, limiting the resolution. The shape of this image is called the *point spread function*, or PSF (Figure 1.4), as this function describes the behavior of the optical system when imaging a point-like source. This property of lenses was already discovered by Abbe in 1873 [23], when he constructed his famous formula:

$$\delta = \frac{\lambda}{2 \cdot \text{NA}}. \quad (1.5)$$

where δ is the smallest distance between two distinguishable features.

Another representation of the optical performance, is the *optical transfer function*, or OTF (Figure 1.4), which is the Fourier transform of the PSF:

$$\text{OTF} = \mathcal{F}(\text{PSF}). \quad (1.6)$$

As this function operates in the frequency space, it describes how the different spatial frequencies are affected by the system. The resolution can also be defined as the maximum of the support of the OTF, since this describes the highest frequency that is still

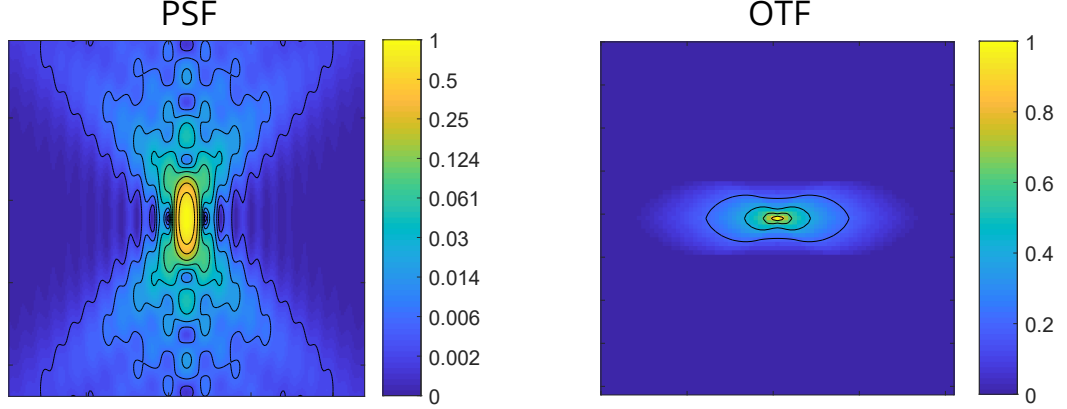


Figure 1.4: Axial cross section of the PSF and OTF of a wide-field microscope. Simulated PSF (left) and OTF (right) for a wide-field microscope with a water immersion objective ($n = 1.33$). $NA = 1.1$, $\lambda = 510 \text{ nm}$. Intensity has been normalized relative to the maximum, and is visualized with different colors (see colorbar). For better visualization, the logarithm of the intensity is displayed for the PSF.

transmitted by the optical system. Any pattern with higher frequency will be lost, thus lies beyond the resolution limit. For circularly symmetric PSFs, the OTF will have real values. However, if this is not the case, the Fourier transform also introduces complex components.

Abbe's formula can be derived from the scalar theory of diffraction using a paraxial approximation (Fraunhofer diffraction, [24]). It is useful to define the following optical coordinates instead of the commonly used Cartesian coordinates x , y and z :

$$v = \frac{2\pi nr}{\lambda_0} \sin \alpha, \quad u = \frac{8\pi nz}{\lambda_0} \sin^2 \frac{\alpha}{2} \quad (1.7)$$

where $r = \sqrt{x^2 + y^2}$ is the distance from the optical axis, and α is the light collection angle as shown on Figure 1.3. In this system the intensity of the electric field in the focus of a lens is [25]:

$$H(u, v) = C_0 \left| \int_0^1 J_0(vr) e^{-i\frac{1}{2} \cdot ur^2} r dr \right|^2, \quad (1.8)$$

where C_0 is a normalization constant, and J_0 is the zeroth-order Bessel function of the first kind.

To determine the lateral resolution of the system, let's substitute $u = 0$ as the axial optical coordinate, and evaluate Equation 1.8 which will give the intensity distribution in the focal plane:

$$H(0, v) = C_0 \left| \int_0^1 J_0(vr) r dr \right|^2 = \left(2 \frac{J_1(v)}{v} \right)^2, \quad (1.9)$$

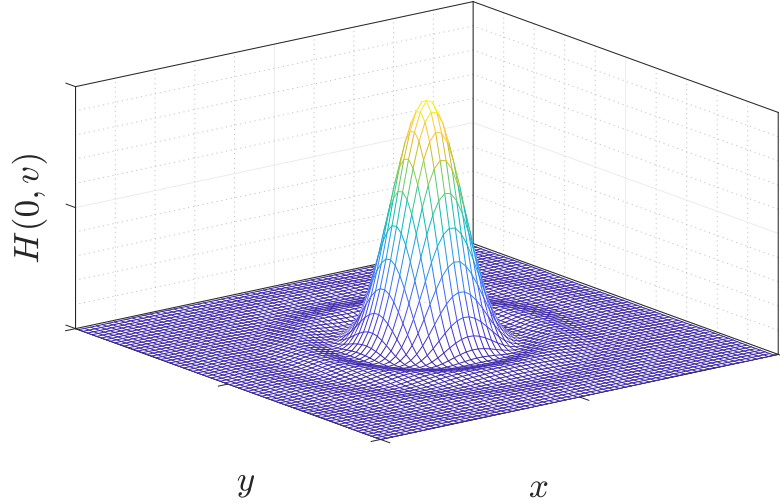


Figure 1.5: Airy pattern. Airy pattern calculated in Matlab based on Equation 1.9

where J_1 is the first-order Bessel function of the first kind. This equation describes the famous Airy pattern (Figure 1.5) which will be the shape of the PSF in the focal plane. The width of this pattern will define the smallest resolvable distance, and although there are multiple definitions for this, the most commonly accepted is the Rayleigh criterion [24, 26]. It defines the resolution as the distance between the central peak and the first local minimum. As this lies at $v = 0.338$, the resolution can be expressed by substituting this value into Equation 1.7 and solving it for r :

$$\delta_{xy} = r(v = 0.338) = \frac{3.83}{2\pi} \frac{\lambda_0}{n \cdot \sin \alpha} \approx 0.61 \frac{\lambda_0}{NA}, \quad (1.10)$$

which is equivalent to Abbe's original formula (Equation 1.5). The only difference is the scaling factor which is due to the slightly different interpretations of the width of the Airy disk as mentioned earlier.

Similarly, to calculate the intensity distribution along the axial direction, let's substitute $v = 0$ to Equation 1.8:

$$H(u, 0) = C_0 \left(\frac{\sin \frac{u}{4}}{\frac{u}{4}} \right)^2. \quad (1.11)$$

For this expression the first minimum lies at $u = 4\pi$. Converting back to Cartesian coordinates, the axial resolution can be expressed as:

$$\delta_z = \frac{2n\lambda_0}{NA^2}. \quad (1.12)$$

So far we only considered a single, point-like emitter. As the intensity function describes how an optical system “spreads out” the image of a point, it is also called the

Point Spread Function (PSF, Figure 1.4). In a more realistic scenario, however the emitters are neither point-like, nor single. Effectively, however, for every emitter the PSF would be imaged on the sensor, and this creates the final image. In mathematical terms, this can be expressed as a convolution operation between the underlying fluorophore distribution of the object (O) and the PSF (H):

$$I(u, v) = O(u, v) * H(u, v). \quad (1.13)$$

The effective result of this kind of diffraction-limited image formation is a blurred image with a finite resolution of δ_{xy} in the lateral direction, and δ_z in the axial direction.

The PSF is further affected by the illumination pattern as well. Since the number of emitted fluorescent photons are roughly proportional to the illumination intensity, the illumination pattern will have an effect on the overall PSF of the system, which can be expressed as:

$$H_{sys} = H_{ill} \cdot H_{det}, \quad (1.14)$$

where H_{ill} is the point spread function of the illumination, and H_{det} is the point spread function of the detection.

1.2 Point scanning methods

In most cases, a wide-field microscope is used to image a layer of cultured cells, or a sectioned sample, thus axial resolution is not a concern. Imaging live specimens, however is not so straightforward, as these samples are usually much thicker than a typical section. For these samples 3-dimensional (3D) imaging is highly beneficial, which necessitates the use of optical sectioning instead of physical sectioning to be able to discriminate the features at different depths.

Due to the design of the wide-field microscope, any photons emitted from outside the focal plane will also be detected by the sensor, however as these are not originating from the focus, only a blur will be visible. This blur potentially degrades image quality and signal-to-noise ratio to such an extent that makes imaging thick samples very difficult if not impossible in a wide-field microscope.

Evaluating Equations 1.10 and 1.12 for a range of possible numerical apertures reveals the significant differences in lateral and axial resolution for any objective (Figure 1.6). Especially for low NAs, this can be significant, a factor of ~ 20 difference. For higher (>0.8) NAs the axial resolution increases faster than the lateral, however they will only be equal when $\alpha = 180^\circ$. This means that isotropic resolution with a single lens is only possible if the lens is collecting all light emitting from the sample, which seems hardly possible, and would be highly impractical. For commonly used high NA objectives the

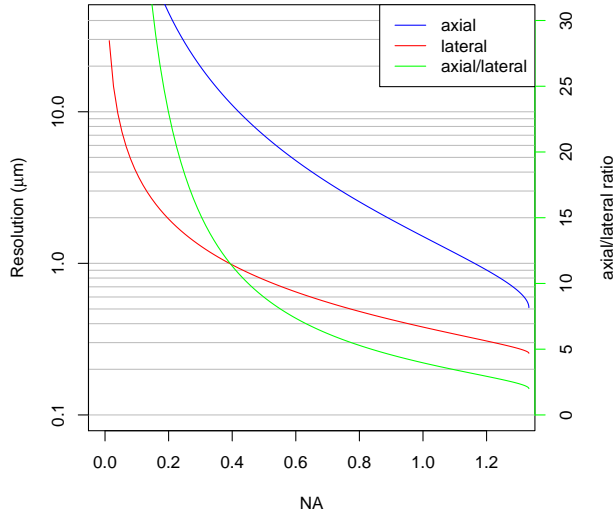


Figure 1.6: Resolution of a wide-field microscope. Axial (blue) and lateral (red) resolutions of a wide-field microscope are shown with respect to the numerical aperture (NA). Resolutions are calculated with $\lambda = 510\text{nm}$, the emission maximum of GFP and $n = 1.33$, the refractive index of water, for water dipping objectives.

lateral to axial ratio will be around 3–6.

Instead of using a single lens to achieve isotropic resolution, it is more practical to image the sample from multiple directions to complement the missing information from different views. When rotating the sample by 90° for example, the lateral direction of the second view will correspond to the axial direction of the first view. If rotation is not possible, using multiple objectives can also achieve similar results, such as in the case of Multi-Imaging Axis Microscopy (MIAM) [27, 28]. This microscope consisted of 4 identical objectives arranged in a tetrahedral fashion to collect as much light as possible from multiple directions, and provide isotropic 3D resolution, albeit at the expense of extremely difficult sample handling, since the sample was surrounded by objectives from all directions.

1.2.1 Confocal laser scanning microscopy

Confocal laser scanning microscopy (CLSM) [29, 30] addresses most of the problems of wide-field microscopy we mentioned in the previous section. It is capable of optical sectioning by rejecting out-of-focus light, which makes it a true 3D imaging technique. Furthermore, the light rejection also massively reduces out-of-focus background, and increases contrast.

This is achieved by two significant modifications compared to the wide-field optical path. To be able to reject the out-of-focus light, an adjustable pinhole is placed at the

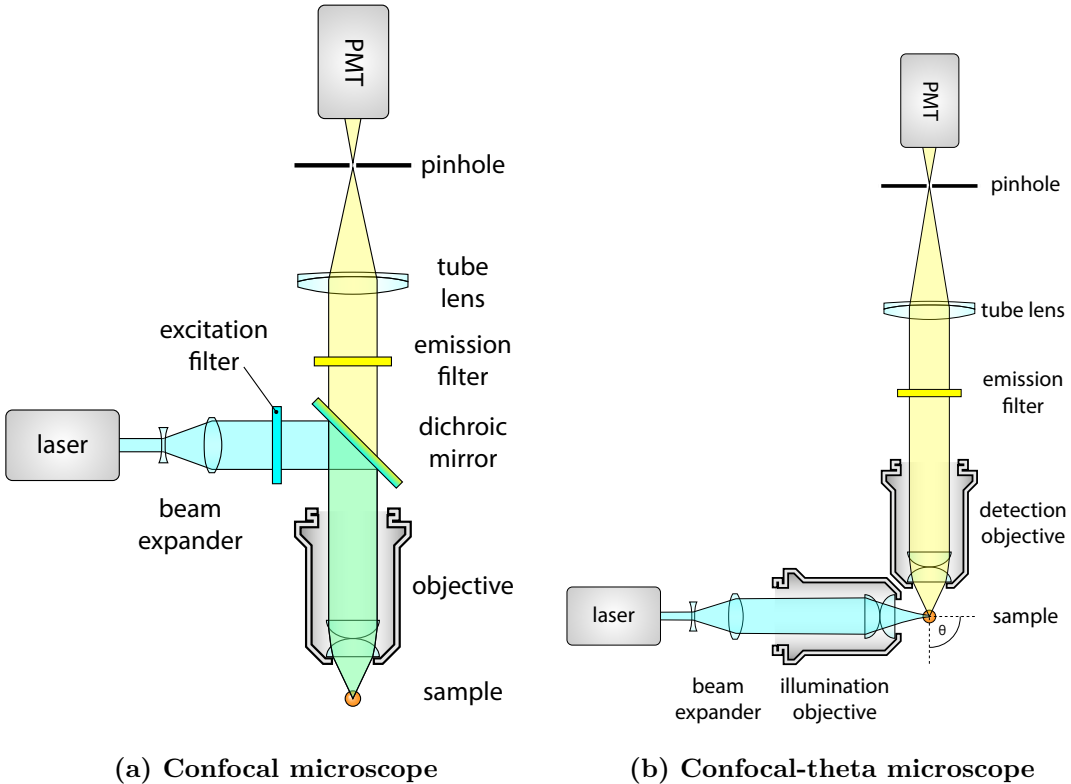


Figure 1.7: Basic optical components of a confocal laser scanning and confocal-theta microscope. Both types of microscopes use confocal image detection, which means that a pinhole is used to exclude light coming from out-of-focus points. Light intensity is measured by a photomultiplier for every point in the region of interest. The final image is generated on a computer using the positions and recorded intensity values. A regular confocal microscope (a) uses the same objective for illumination and detection, while a confocal-theta microscope (b) uses a second objective that is rotated by θ around the focus. In this case, $\theta = 90^\circ$.

focus of the tube lens. Light rays originating from the focal point will meet here, and are able to pass through the pinhole. However, out-of-focus light will converge either before or after the aperture, and thus the aperture blocks these rays. To maximize the fluorescence readout efficiency for the single focal point, a photomultiplier tube is used instead of an area sensor (Figure 1.7a).

As only a small focal volume is detected at a time, the illumination light is also focused here by coupling an expanded laser beam through the back aperture of the objective. This not only increases illumination efficiency (since other, not detected points are not illuminated), but has the added benefit of increasing the resolution as well. This is due to the combined effect of illumination and detection PSFs as described in Equation 1.14 (Figure 1.8). For Gaussian-like PSFs, the final resolution (along a single direction) can be calculated in the following way:

$$\frac{1}{\delta_{sys}^2} = \frac{1}{\delta_{ill}^2} + \frac{1}{\delta_{det}^2}, \quad (1.15)$$

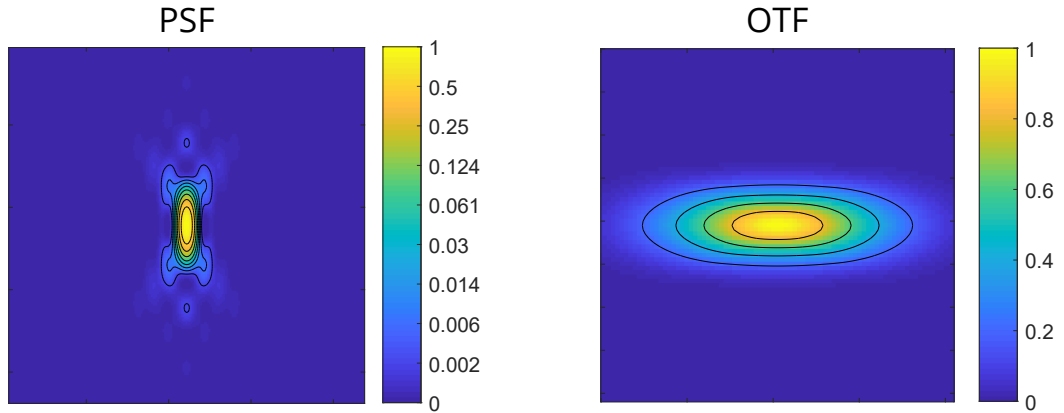


Figure 1.8: Axial cross section of the PSF and OTF of a confocal laser scanning microscope. Simulated PSF and OTF for a laser scanning confocal microscope with a water immersion objective ($n = 1.33$). $NA = 1.1$, $\lambda = 510\text{ nm}$. Intensity has been normalized relative to the maximum, and is visualized with different colors (see colorbar). For better visualization, the logarithm of the intensity is displayed for the PSF.

where δ_{ill} and δ_{det} are the resolutions for the illumination and detection, respectively. Since the same objective is used for both illumination and detection, and the difference in wavelength is almost negligible, $\delta_{ill} = \delta_{det} = \delta$, the final system resolution will be:

$$\delta_{sys} = \frac{1}{\sqrt{2}}\delta. \quad (1.16)$$

This means that the distinguishable features in a confocal microscope are ~ 0.7 times smaller than in a wide-field microscope using the same objective.

Because of the different detection method in a confocal microscope, direct image formation on an area sensor is not possible, since at any given time only a single point is interrogated in the sample. Instead, it is necessary to move the illumination and detection point in synchrony (or in a simpler, albeit slower solution, to move the sample) to scan the entire field of view. The image can be later computationally reconstructed by a computer program that records the fluorescence intensity of every point in the field of view, and displays these values as a raster image.

1.2.2 Variants of confocal microscopy

Although confocal microscopy already has 3D capabilities, its axial resolution is still limited compared to the lateral, since it uses only one objective. An alternative realization of the confocal microscope, the confocal theta microscope [31] introduces a second objective to the system that is used to illuminate the sample (Figure 1.7b). Since this decouples the illumination and detection, using a dichroic mirror is no longer necessary. The second objective is rotated by θ around the focus, this is where the name of this



Figure 1.9: Basic concept of single-plane illumination microscopy. The sample is illuminated from the side by laser light shaped to a light-sheet (blue). This illuminates the focal plane of the detection lens, that collects light in a wide-field mode (yellow). The image is recorded, and the sample is translated through the light-sheet to acquire an entire 3D stack.

setup originates from.

As in the case of standard confocal microscopy, the system PSF is improved by the illumination pattern. Here, however, the axial direction of the detection coincides with the lateral direction of the illumination, which results in a dramatic improvement of axial resolution compared to standard confocal microscopy. Lateral resolution will also be increased, but by a smaller extent, resulting in an almost isotropic PSF and equal axial and lateral resolutions. Although this is a big improvement to confocal microscopy in terms of resolution, this technique did not reach a widespread adoption as it complicates sample handling, while still suffering from two drawbacks of confocal microscopy that limit its live imaging capabilities, namely phototoxicity and imaging speed.

One improvement to address these drawbacks is the use of a spinning disk with a specific pattern of holes (also called Nipkow disk) to generate multiple confocal spots at the same time [60]. If these spots are far enough from each other, confocal rejection of out-of-focus light can still occur. As the disk is spinning, the hole pattern will sweep the entire field of view, eventually covering all points [62]. The image is recorded by an area detector, such as a CCD or EM-CCD, which speeds up image acquisition [63].

1.3 Light-sheet microscopy

A selective-plane illumination microscope (SPIM) uses a light-sheet to illuminate only a thin section of the sample (Figure 1.9). This illumination plane is perpendicular to the imaging axis of the detection objective and coincides with the focal plane. This way, only the section in focus will be illuminated, thus providing much better signal-to-noise ratio. In case of conventional wide-field fluorescence microscopy, where the whole specimen

1.3 Light-sheet microscopy

is illuminated, out-of-focus light contributes to a significant background noise. With selective-plane illumination, this problem is intrinsically solved, and it also provides a true optical sectioning capability. This makes SPIM especially suitable for 3D imaging.

The main principle behind single-plane illumination microscopy, that is illuminating the sample from the side by a thin light-sheet, dates back to the early 20th century, when Siedentopf and Zsigmondy first described the ultramicroscope [36]. This microscope used sunlight as an illumination source that was guided through a precision slit to generate a thin light-sheet. This allowed Zsigmondy to visualize gold nanoparticles floating in and out of the light-sheet by detecting the scattered light from the particles. Since these particles were much smaller than the wavelength of the light, the device was called an ultramicroscope. His studies with colloids and the development of the ultramicroscope led Zsigmondy to win the Nobel Prize in 1925.

After Zsigmondy this method was forgotten until rediscovered in the 1990s, when Voie *et al.* constructed their Orthogonal-plane Fluorescent Optical Sectioning (OPFOS) microscope [37]. They used it to image a fixed, optically cleared and fluorescently labelled guinea pig cochlea. In order to acquire a 3D dataset, the sample was illuminated from the side with a light-sheet generated by a cylindrical lens, then rotated around the center axis to obtain multiple views. Although they only reached a lateral resolution of around 10 µm and axial resolution of 26 µm, this method allowed them to generate a 3D reconstruction of the guinea pig cochlea [38].

Later, in 2002, Fuchs *et al.* developed Thin Light-Sheet Microscopy (TLSM) [39] and used this technique to investigate the microbial life in seawater samples without disturbing their natural environment (by, *e.g.*, placing them on a coverslip). Their light-sheet was similar to the one utilized in OPFOS, being 23 µm thin, and providing a 1 mm × 1 mm field of view.

Despite these early efforts, the method did not gain larger momentum. The real breakthrough in light-sheet imaging happened at the European Molecular Biology Laboratory (EMBL) in 2004, where Huisken *et al.* [40] combined the advantages of endogenous fluorescent proteins and the optical sectioning capability of light-sheet illumination to image Medaka fish embryos, and the complete embryonic development of a *Drosophila melanogaster* embryo. They called this Selective-Plane Illumination Microscopy (SPIM), and it quickly became popular to investigate developmental biological questions.

Since then, light-sheet-based imaging has gained more and more popularity, as it can be adapted and applied to a wide variety of problems. Although sample mounting can be challenging because of the objective arrangement, this can also be an advantage, since new microscopes can be designed with the sample in mind [3, J3] (Figure 1.10). This made it possible to adapt the technique for numerous other specimens, such as zebrafish larvae [49], *C. elegans* embryos [42], mouse brain [6], and even mouse embryos [J2, 50,

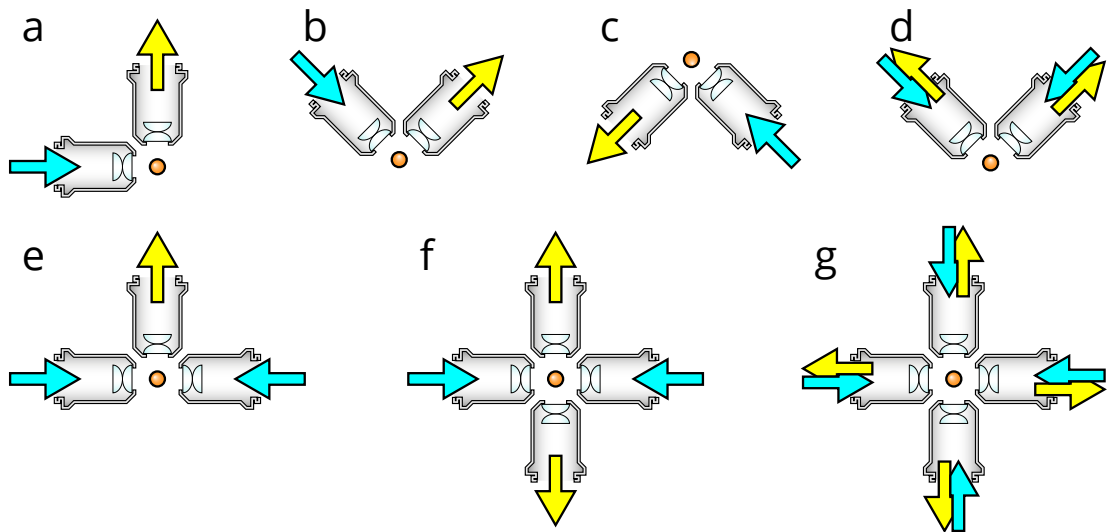


Figure 1.10: Different optical arrangements for light-sheet microscopy. (a) Original SPIM design with a single lens for detection and illumination. [40] (b) Upright SPIM to allow for easier sample mounting such as using a petri dish (iSPIM, [41, 42, J1]). (c) Inverted SPIM, where the objectives are below the sample, which is held by a thin foil [J2]. (d) Dual-view version of the upright configuration, where both objective can be used for illumination and detection (diSPIM, [43]). (e) Multidirectional-SPIM (mSPIM) for even illumination of the sample with two objectives for illumination [44]. (f) Multi-view SPIM with two illumination and detection objectives for *in toto* imaging of whole embryos (MuVi-SPIM [45], SimView [46], Four-lens SPIM [47]). (g) A combination of (d) and (f), using four identical objectives, where both can illuminate and detect in a sequential manner, to achieve isotropic resolution without sample rotation (IsoView [48]).

51].

As many of these specimens require very different conditions and mounting techniques, these microscopes have been adapted to best accommodate them. An upright objective arrangement (Figure 1.10b), for example, allows imaging samples on a cover-slip, while its inverted version is well suited for mouse embryos, where a foil is separating the samples from the immersion medium (Figure 1.10c). A modified version of the upright arrangement allows for multi-view imaging using both objectives for illumination and detection in a sequential manner (Figure 1.10d) [52].

To achieve a more even illumination in larger samples, two objectives can be used from opposing directions to generate two light-sheets (Figure 1.10e) [44]. This arrangement can further be complemented by a second detection objective, to achieve parallelized multi-view imaging (Figure 1.10f) [45–47]. For ultimate speed, 4 identical objectives can be used to achieve almost instantaneous views from 4 different directions by using all objectives for illumination and detection (Figure 1.10g) [48].

Furthermore, because of the wide-field detection scheme it is possible to combine SPIM with many superresolution techniques, such as single molecule localization [53], STED [54], RESOLFT [J1], or structured illumination [7, 55, 56].

Since illumination and detection for light-sheet microscopy are decoupled, two inde-

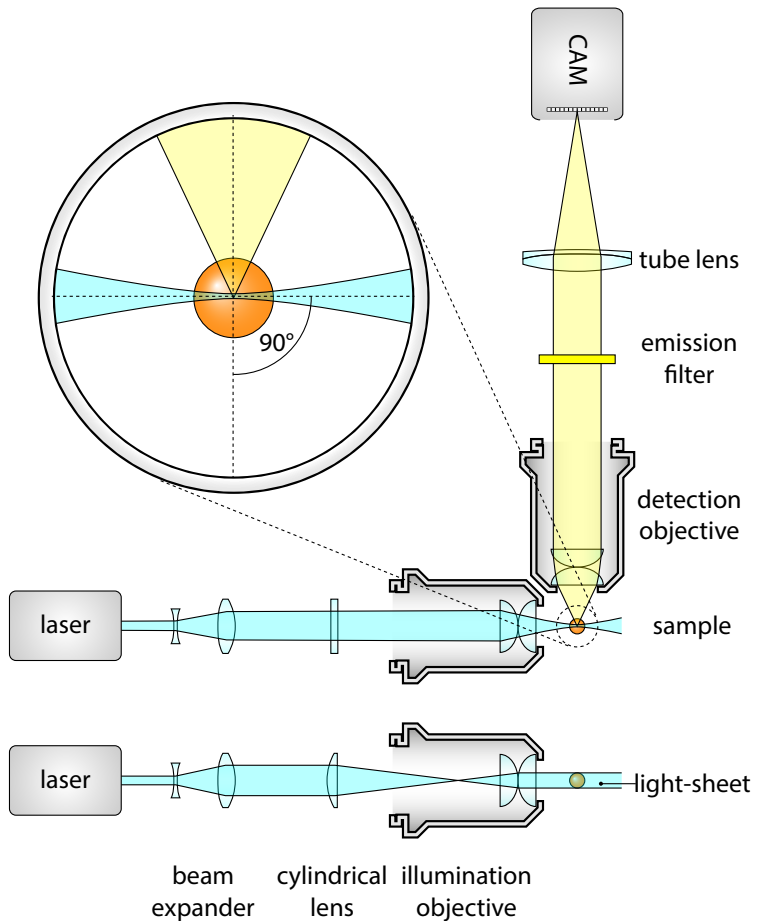


Figure 1.11: Basic optical components of a SPIM. A dedicated illumination objective is used to generate the light-sheet, which is an astigmatic Gaussian beam, focused along one direction. Astigmatism is introduced by placing a cylindrical lens focusing on the back focal plane of the objective. Detection is performed at a right angle, with a second, detection objective. Scattered laser light is filtered out, and a tube lens forms the image on an area sensor, such as an sCMOS camera.

pendent optical paths are implemented.

The detection unit of a SPIM is largely equivalent to a detection unit of a wide-field microscope without the dichroic mirror (Figure 1.11). The most important components are the objective together with the tube lens, filter wheel, and a sensor, typically a charge coupled device (CCD) or scientific complementary metal–oxide–semiconductor (sCMOS) camera.

The resolution of a light-sheet microscope mainly depends on the detection objective. Since imaging biological specimens usually requires a water-based solution, the objectives also need to be directly submerged in the medium to minimize spherical aberrations. As the refraction index of water ($n = 1.33$) is greater than the refraction index of air, these objectives tend to have a higher NA, resulting in higher resolution. As the illumination

is decoupled in this system, the light-sheet thickness also has an influence on the axial resolution. Finally, the resolution also depends on the pixel size of the sensor which determines the spatial sampling rate of the image.

Although image quality and resolution greatly depend on the detection optics, the real strength of light-sheet microscopy is the inherent optical sectioning which is due to the specially aligned illumination pattern that confines light to the vicinity of the detection focal plane.

There are two most commonly used options to generate a light-sheet: either by using a cylindrical lens to illuminate the whole field of view with a static light-sheet, as in the original SPIM concept [40]; or by quickly scanning a thin laser beam through the focal plane, thus resulting in a virtual light-sheet. This method is called Digitally Scanned Light-sheet Microscopy (DSLM) [49].

1.3.1 Static light-sheet illumination

For a static light-sheet, the normally circular Gaussian laser beam needs to be shaped in an astigmatic manner, *i.e.*, either expanded or squeezed along one direction, to shape it into a sheet instead of a beam. This effect can be achieved by using a cylindrical lens, which, as the name suggests, has a curvature in one direction, but is flat in the other, thus focusing a circular beam to a sheet (Figure 1.11).

However, to achieve light-sheets that are sufficiently thin for optical sectioning, one would need to use a cylindrical lens with a very short focal length, and these are hardly accessible in well corrected formats. For this reason, it is more common to use a longer focal length cylindrical lens in conjunction with a microscope objective, which is well corrected for chromatic and spherical aberrations [57]. This way, the light-sheet length, thickness and width can be adjusted for the specific imaging tasks.

Light-sheet dimensions

The shape of the illumination light determines the optical sectioning capability and the field of view of the microscope, so it is important to be able to quantify these measures. The most commonly used illumination source is a laser beam coupled to a single mode fiber, thus its properties can be described by Gaussian beam optics.

For paraxial waves, *i.e.*, waves with nearly parallel wavefront normals, the general wave equation can be approximated with the paraxial Helmholtz equation [58]

$$\nabla_T^2 U + i2k \frac{\partial U}{\partial z} = 0 \quad (1.17)$$

where $\nabla_T^2 = \frac{\partial^2}{\partial x^2} + \frac{\partial^2}{\partial y^2}$, $U(\vec{r})$ is the wave function, $k = \frac{2\pi}{\lambda}$ is the wavenumber and z is in the direction of the light propagation.

1.3 Light-sheet microscopy

A simple solution to this differential equation is the Gaussian beam:

$$U(r, z) = A_0 \cdot \frac{W_0}{W(z)} \cdot e^{-\frac{r^2}{W^2(z)}} \cdot e^{-i \cdot \phi(r, z)} \quad (1.18)$$

where A_0 is the amplitude of the wave, W_0 is the radius of the beam waist (the thinnest location on the beam), $r = \sqrt{x^2 + y^2}$ is the distance from the center of the beam, $W(z)$ is the radius of the beam at distance z from the waist, and $\phi(r, z)$ is the combined phase part of the wave-function. Furthermore:

$$W(z) = W_0 \sqrt{1 + \left(\frac{z}{z_R}\right)^2} \quad (1.19)$$

where the parameter z_R is called the Rayleigh-range, and is defined the following way:

$$z_R = \frac{\pi W_0^2}{\lambda}. \quad (1.20)$$

Apart from the circular Gaussian beam, the elliptical Gaussian beam is also an eigenfunction of Helmholtz equation (Equation 1.17) which describes the beam shape after a cylindrical lens:

$$U(x, y, z) = A_0 \cdot \sqrt{\frac{W_{0,x}}{W_x(z - z_{0,x})}} \sqrt{\frac{W_{0,y}}{W_y(z - z_{0,y})}} \cdot e^{-\frac{x^2}{W_x^2(z - z_{0,x})}} \cdot e^{-\frac{y^2}{W_y^2(z - z_{0,y})}} \cdot e^{-i \cdot \phi(x, y, z)} \quad (1.21)$$

This beam still has a Gaussian profile along the x and y axes, but the radii ($W_{0,x}$ and $W_{0,y}$), and the beam waist positions ($z_{0,x}$ and $z_{0,y}$) are uncoupled, which results in an elliptical and astigmatic beam. The beam width can now be described by two independent equations for the two orthogonal directions:

$$W_x(z) = W_{0,x} \sqrt{1 + \left(\frac{z}{z_{R,x}}\right)^2} \quad \text{and} \quad W_y(z) = W_{0,y} \sqrt{1 + \left(\frac{z}{z_{R,y}}\right)^2}. \quad (1.22)$$

Since the beam waist is different along the two axes, the Rayleigh range is also different:

$$z_{R,x} = \frac{\pi W_{x,0}^2}{\lambda}, \quad z_{R,y} = \frac{\pi W_{y,0}^2}{\lambda}. \quad (1.23)$$

Based on these equations, the light-sheet dimensions and usable field of view can be specified (Figure 1.12a). The light-sheet thickness will depend on the beam waist, $W_{0,y}$ (if we assume the cylindrical lens is focusing along y), and the length of the light-sheet can be defined as twice the Rayleigh range, $2 \cdot z_{R,y}$ (Figure 1.12b). As these are coupled (see Equation 1.23), having a thin light-sheet for better sectioning also means that its length will be relatively short. Fortunately, because of the quadratic relation, to increase

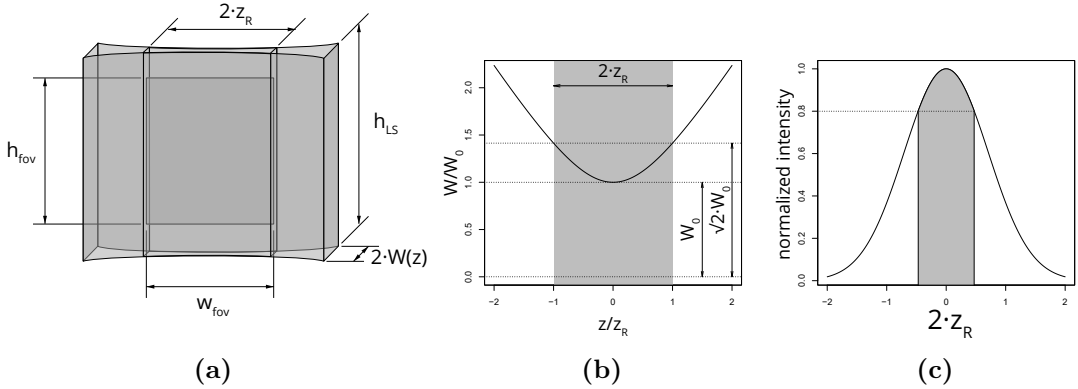


Figure 1.12: Light-sheet dimensions. (a) The light-sheet, with the field of view indicated. Since the light-sheet intensity is uneven, the field of view has to be confined to a smaller region. (b) The width and thickness of the field of view depends on the Rayleigh length of the beam ($z_{R,y}$) and the beam waist (W_0). (c) The height of the field of view is determined by the Gaussian profile of the astigmatic beam.

the field of view by a factor of two, the light-sheet thickness only needs to increase by a factor of $\sqrt{2}$.

Light-sheet height is determined by the intensity profile of the beam along the vertical axis (Figure 1.12c). Since this is a Gaussian function (see Equation 1.18), only a small part in the middle can be used for imaging, because towards the sides the intensity dramatically drops. When allowing a maximum 20% drop-off in intensity at the edges, the light-sheet height becomes $h_{fov} = 2 \cdot 0.472 \cdot W_{x,0} = 0.944 \cdot W_{x,0}$.

1.3.2 Digitally scanned light-sheet illumination

Although generating a static light-sheet is relatively straightforward with the simple addition of a cylindrical lens to the light path, it has some drawbacks. As already mentioned in the previous section, the light intensity distribution along the field of view is not constant, as the light-sheet is shaped from a Gaussian beam. Furthermore, along the lateral direction of the light-sheet the illumination NA is extremely low, resulting in effectively collimated light. Because of this, shadowing artifacts can deteriorate the image quality [44].

A more flexible way of creating a light-sheet is by scanning a focused beam in the focal plane to generate a virtual light-sheet (digital scanned light-sheet microscopy, DSLM [49]). Although this method might require higher peak intensities, it solves both drawbacks of the cylindrical lens illumination. By scanning the beam, the light-sheet height can be freely chosen, and a homogenous illumination will be provided. Focusing the beam in all directions evenly introduces more angles in the lateral direction as well, which shortens the length of the shadows.

The basic optical layout of a DSLM is shown on Figure 1.13. A galvanometer controlled mirror that can quickly turn around its axis is used to alter the beam path, which

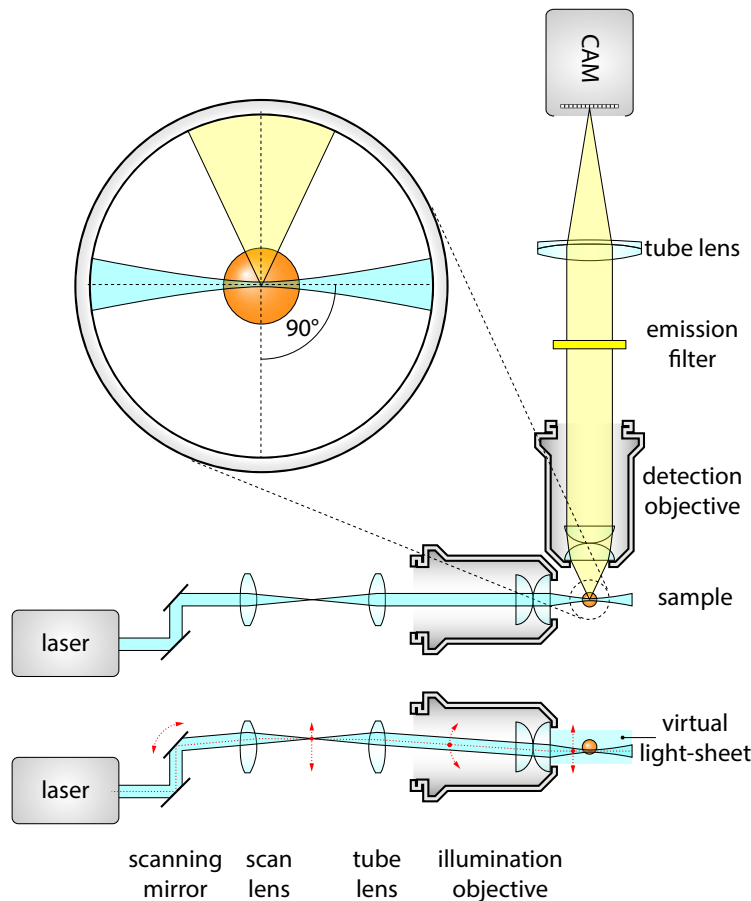


Figure 1.13: DSLM illumination. DSLM illuminates a specimen by a circularly-symmetric beam that is scanned over the field of view. This creates a virtual light-sheet, which illuminates a section of a specimen just like the SPIM. The light-sheet in DSLM is uniform over the whole field of view and its height can be dynamically altered by changing the beam scan range.

will result in an angular sweep of the laser beam. To change the angular movement to translation, a scan lens is used to generate an intermediate scanning plane. This plane is then imaged to the specimen by the tube lens and the illumination objective, resulting in a scanned focused beam at the detection focal plane. The detection unit is identical to the wide-field detection scheme, similarly to the static light-sheet illumination. By scanning the beam at a high frequency, a virtual light-sheet is generated, and the fluorescence signal is captured by a single exposure on the camera, resulting in an evenly illuminated field of view.

1.4 Light-sheet imaging of mammalian development

Live imaging of mammalian embryos is an especially challenging task due to the intrauterine nature of their development. As the embryos are not accessible in their natural

1.4 Light-sheet imaging of mammalian development

environment, it is necessary to replicate the conditions as closely as possible by providing an appropriate medium, temperature, and atmospheric composition. Moreover, these embryos are extremely sensitive to light, which poses a further challenge for microscopy [67]. Illumination with high laser power for an extended time frame can result in bleaching of the fluorophores, which in turn will lower the signal at later times. Furthermore, any absorbed photon has the possibility to modify the chemical bonds inside the specimen, which can lead to phototoxic effects, disrupting the proper development of the embryo.

Because of its optical sectioning capabilities combined with the high specificity of fluorescent labels, confocal microscopy has had an immense influence on biological research, and has been the go-to technique for decades for many discoveries [60, 59, 61]. Imaging live specimens for an extended period of time with confocal microscopy, although possible [32, 33], is not ideal. Due to the use of a single objective, for each voxel imaged, a large portion of the specimen has to be illuminated below and above the focal plane as well. This results in a high dose of radiation on the sample that can be as much as 30–100 times larger than the dose used for the actual imaging [34], depending on the number of planes recorded. Moreover, the usage of the pinhole, although rejects out-of-focus light, also decreases the detectable signal intensity, thus it can have a negative impact on image contrast [35].

In contrast to confocal microscopy, light-sheet microscopy uses a much more efficient illumination scheme, as only the vicinity of the focal plane is illuminated. To achieve 3D imaging, the sample is translated relative to the light-sheet, while snapshots are taken from each plane. The total irradiation in this case will be proportional to the thickness of the light-sheet, and will not depend on the number of planes recorded.

Another benefit of light-sheet microscopy lies in the parallel readout of the fluorescence due to the wide-field detection scheme. Since the whole focal plane is captured at the same time, this can be considerably faster compared to the point-scanning method of confocal microscopy.

In the next sections we will review the possible strategies for imaging mouse specimens with light-sheet microscopy in different stages of development: pre-implantation and post-implantation embryos, and also adult mice.

1.4.1 Imaging mammalian pre-implantation development

Pre-implantation is the first phase of mouse embryonic development that starts right after fertilization. The embryo in this phase is still in the oviduct, travelling towards the uterus, where it will implant into the uterine wall. The developmental stage between fertilization and implantation is called the pre-implantation stage. Here the embryo divides, and already the first cell fate specifications start when forming the trophoectoderm (TE) and the inner cell mass (ICM) at the blastocyst stage. ICM cells will form the embryo

1.4 Light-sheet imaging of mammalian development

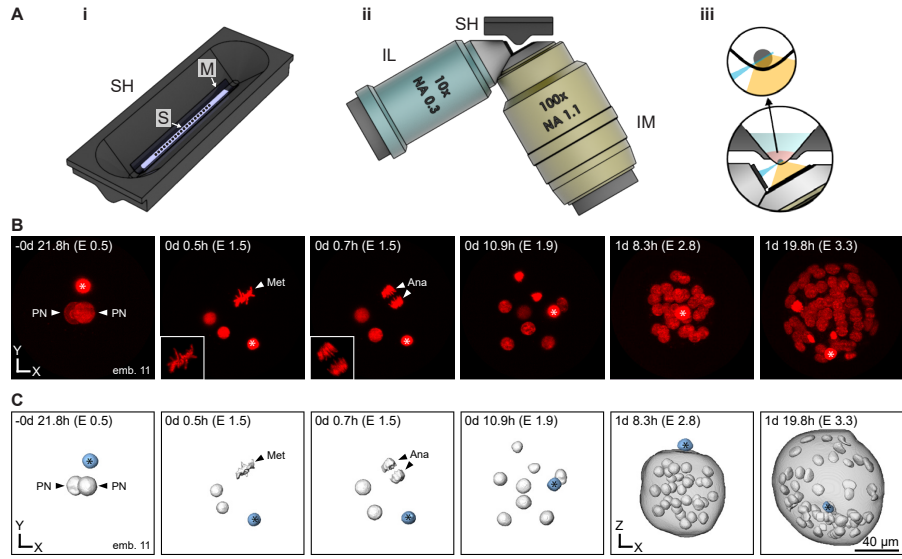


Figure 1.14: Inverted light-sheet microscope for multiple early mouse embryo imaging. (i) A sample holder (SH), containing a transparent FEP membrane (M) allows multiple embryo samples (S) to be placed in line for multisample imaging. (ii) Inverted objective orientation with side view of the sample holder. One possible configuration is to use a 10×0.3 NA illumination objective (IL) and another 100×1.1 NA detection objective placed at a right angle to the illumination. (iii) Close up on side view of sample on FEP membrane with both objectives. Since the FEP membrane is transparent on water, it provides no hindrance to the illumination beam in penetrating the sample or for the emitted fluorescence on reaching the detection objective. (B) Still images of one particular timelapse experiment, and (C) corresponding segmented nuclei. The star depicts the polar body. Adapted from Strnad *et al.* [J2]

proper, while TE cell will contribute to the formation of the extraembryonic tissues.

During this process the embryo is still self-sufficient, which makes it possible to image this stage in an *ex vivo* embryo culture by providing the proper conditions [69]. Long term imaging, however, is extremely challenging due to the very high light sensitivity of the specimens. Imaging these embryos in a confocal microscope will lead to incomplete development, even if the imaging frequency is minimized to every 15 mins [J2].

Imaging for just a few hours is already enough to investigate important processes, such as cell fate patterning [70]. Other approaches aim to lower the phototoxicity by either using 2-photon illumination which operates at longer wavelengths [71–73], or by lowering imaging frequency as a compromise [74]. These approaches, however, either require highly specialized equipment, such as an ultra-short pulsed laser, or are compromising on the time resolution.

Light-sheet microscopy, on the other hand, drastically lowers the phototoxic effects by using a much more efficient illumination scheme (see Section 1.3), and thus makes a better use of the photon budget. Using this technique, it is possible to image the full pre-implantation development at high spatial and temporal resolution without any negative impact on the developmental process. Such a microscope was developed by Strnad *et al.* at EMBL [J2], who used it to understand when exactly the first cell fate specification is decided in the embryonic cells.

1.4 Light-sheet imaging of mammalian development

As a mouse embryo culture is not compatible with the standard agarose-based sample mounting techniques, a completely new approach was taken, which resulted in a microscope designed around the sample. The sample holder forming a V-shape was built with a bottom window, and it is lined with a thin FEP (fluorinated ethylene propylene) foil that supports the embryos (Figure 1.14A, i). This arrangement allows the utilization of the standard microdrop embryo culture, while providing proper viewing access for the objectives. As the embryos are relatively small (100 µm) and transparent, a single illumination and single detection objective arrangement is enough for high quality imaging. A low resolution (NA=0.3) objective is used to generate the scanned light-sheet, and a high resolution (NA=1.1) objective is detecting the fluorescence at 50× magnification (Figure 1.14A, ii). As the foil is curved, it allows unrestricted access to the embryo, while separating the imaging medium from the immersion liquid (Figure 1.14A, iii). Furthermore, its refractive index is matching the refractive index of water, so optical aberrations are minimized.

Using this setup, Strnad *et al.* were able to pinpoint the exact timing of the first cell fate decision that leads either to ICM or TE cells. More than 100 embryos expressing nuclear (H2B-mCherry) and membrane (mG) markers were imaged for the entire 3 days of pre-implantation development (Figure 1.14B). The image quality was sufficient to segment all nuclei in the embryos (Figure 1.14C), and track them from 1 to 64 cell stage, building the complete lineage tree. Based on the lineage trees and the final cell fate assignments, it was determined that at the 16 cell stage the final specification is already decided, while earlier than this it is still random.

1.4.2 Imaging mammalian post-implantation development

After the initial 3 days of pre-implantation, the embryo undergoes the implantation process, during which it is inaccessible to microscopical investigations. Although a new method was recently developed that allows the *in vitro* culturing of the embryos embedded in a 3D gel [76], this has not reached wider adoption yet. Hence, developmental processes during implantation have only been investigated in fixed embryos.

Following the implantation process, at the post-implantation phase, *ex vivo* embryo culturing becomes possible again [77, 78], and these embryos can be kept alive for several days in an artificial environment. During this process especially interesting stages are the late blastocyst (~E4.5), gastrulation (~E6.5), and somite formation (~E8.5). Before live imaging techniques became available, these stages were mostly investigated using *in situ* visualization techniques to shed light on several developmental processes [79]. Many pathways playing important roles have been identified this way, however, live imaging is still necessary to validate these results and ensure continuity in the same specimen [80].

Light-sheet microscopy is a good choice for imaging these stages, just like in the case

1.4 Light-sheet imaging of mammalian development

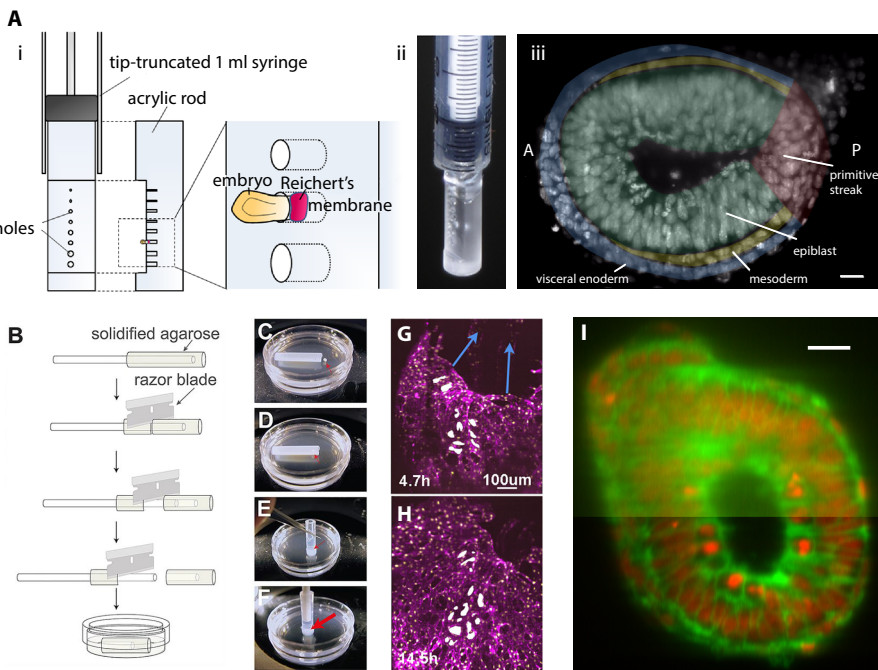


Figure 1.15: Imaging mouse post-implantation development. (A) (i, ii) Mounting technique for E5.5 to E6.5 embryos. A tip-truncated 1 mL syringe holds an acrylic rod, cut and drilled with holes of different size in order to best fit the mouse embryo by its Reichert's membrane, leaving the embryo free inside the medium. (iii) Maximum intensity projection of a 13 µm thick slice at 78 µm from distal end of an E6.5 mouse embryo. The different tissues corresponding to the rudimentary body plan are annotated. Scale bar: 20 µm. (B) For stages ranging between E6.5 and E8.5, mounting using a hollow agarose cylinder has also successfully been proposed. Optimal sizes for the corresponding embryonic stage to be imaged can be produced, so that the embryo can grow with least hindrance. (C–F) Steps for mounting the mouse embryo inside the agarose cylinder. The inner volume of the cylinder can be filled with optimal medium, allowing the much larger chamber volume to have less expensive medium. (G–H) Example images of a 9.8 h timelapse with the mounting shown in (B) where the expansion of the yolk sac can be observed in direction of the blue arrows. (I) In order to aid multiview light-sheet setups in overcoming the higher scattering properties of embryos at this stage, and to allow faster and easier data recording, electronic confocal slit detection allows better quality images to be taken at shorter acquisition times. Scale bar: 20 µm. Adapted from Ichikawa *et al.* [50], Udan *et al.* [51] and de Medeiros and Norlin *et al.* [75].

of pre-implantation embryos. These embryos, however, present new challenges for sample handling and culturing. Owing to their extreme sensitivity, dissection can be difficult, especially for earlier stages (E4.5). Furthermore, since the embryo is also growing during development, gel embedding is not an option, as this might constrain proper development. Thus, special handling and mounting techniques had to be developed in order to allow live 3D imaging of these specimens.

Ichikawa *et al.* [50] designed a custom mounting apparatus manufactured from acrylic in the shape of a rod that fits in a standard 1 mL tip-truncated syringe (Figure 1.15A, i). Several holes were drilled in the rod with different sizes, which can accommodate different sized embryos. The embryos are held by an extraembryonic tissue, the Reichert's membrane (Figure 1.15A, ii). Mounting this way doesn't disturb the embryo itself, and it can freely develop in the culturing medium, while it is also stationary for the purpose of imaging. Using this technique, Ichikawa *et al.* were able to image through several stages of

1.4 Light-sheet imaging of mammalian development

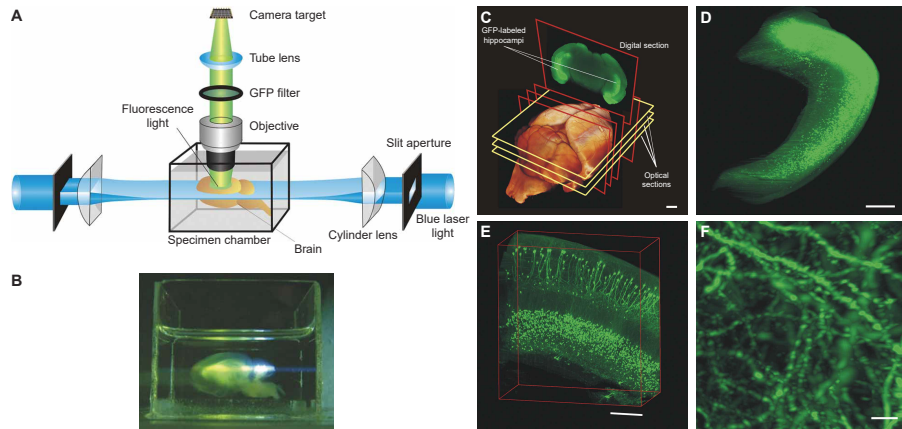


Figure 1.16: Imaging adult mouse brain with light-sheet microscopy. (A) Schematics of the ultramicroscope for brain imaging. The specimen is embedded in clearing medium to ensure necessary imaging depth. Illumination is applied from two sides to achieve even illumination for the whole field of view. Light-sheet is generated by a slit aperture followed by a cylindrical lens. The specimen is imaged from the top using wide-field detection method. (B) Photograph of the imaging chamber with a mounted cleared specimen and light-sheet illumination. (C) Surface rendering of a whole mouse brain, reconstructed from 550 optical sections. GFP and autofluorescence signal was recorded. Hippocampal pyramidal and granule cell layers are visible in the digital section. Scale bar: 1 mm. Objective: Planapochromat 0.5×. (D) Reconstruction of an excised hippocampus from 410 sections. Note that single cell bodies are visible. Scale bar: 500 μm. Objective: Fluar 2.5×. (E) 3D reconstruction of a smaller region of an excised hippocampus from 132 sections. Scale bar: 200 μm. Objective: Fluar 5×. (F) 3D reconstruction of CA1 pyramidal cells imaged with a higher resolution objective (LD-Plan Neofluar 20× NA 0.4) in a whole hippocampus (430 sections). Dendritic spines are also visible, even though usually a higher NA objective (>1.2) is required to visualize these. Scale bar: 5 μm. Adapted from Dodt *et al.* [6].

development, including interkinetic nuclear migration at stages E5.5–6.5 (Figure 1.15A, iii).

A second method of sample mounting for light-sheet imaging was developed by Udan *et al.* who were able to record a full 24 h time-lapse of living embryos focusing on the gastrulation and yolk sac formation processes (Figure 1.15G–I). Their mounting technique comprised of producing a hollow agarose container shaped like a cylinder that could support the embryo from below without constraining its growth (Figure 1.15B–F).

Another consideration to keep in mind, is the growing size of the embryo. As it gets bigger, illumination is less efficient, and scattering can dominate at larger depths. As mentioned in earlier (Figure 1.3) this can be alleviated by multi-view imaging: illuminating and detecting from multiple directions. Electronic confocal slit detection can further improve the signal-to-noise ratio by rejecting unwanted scattered light, which allows deeper imaging in large specimens, even up to E7.5 (Figure 1.15I) [75].

1.4.3 Imaging adult mice

Imaging adult mice is especially interesting for answering neurobiological questions. Since development is over at this stage, the use of an environmental chamber is no longer necessary. The biggest challenge for imaging these samples is their size, as they are centimeters in size instead of less than a millimeter as in the embryonic stage. Furthermore, the tissues

1.4 Light-sheet imaging of mammalian development

of adult mice are much more opaque, which severely limits imaging depth. Light-sheet microscopy can already deal with large specimens, however, to achieve (sub)cellular resolution for an entire brain, for example, multiple recordings have to be stitched together after acquisition [81].

Light scattering and absorption depend on the tissue composition and imaging depth. Especially the brain with a high concentration of lipids in the myelinated fibers pose a real challenge for imaging. Live imaging is usually performed with 2-photon microscopy which can penetrate the tissue up to 800 µm deep [82]. Using fixed samples, however, the scattering problem can be eliminated by the use of tissue clearing methods.

Tissue clearing is a process that removes and/or substitutes scattering and absorbing molecules by a chemical process while keeping the tissue structure intact and preserving fluorescence. The most dominant contributors to these effects are the proteins and lipids. Proteins in the cells locally change the refractive index of the tissue which leads to scattering, while lipids predominantly absorb the light. Clearing methods tackle these problems by chemically removing and substituting lipids by certain types of gel, and immersing the whole sample in a medium with higher refractive index to match the optical properties of proteins. Numerous methods have been developed for tissue clearing, such as ScaleA2 [83], 3DISCO [84, 85], SeeDB [86], CLARITY [87], CUBIC [88] and iDISCO [89].

The first combination of optical clearing and light-sheet microscopy for whole brain imaging was performed by Dodt *et al.* using a custom ultramicroscope consisting of two opposing illumination arms and a single detection arm with an objective from above (Figure 1.16A). The light-sheets were positioned horizontally, and the cleared samples could be placed in a transparent imaging chamber filled with the clearing medium (Figure 1.16B). Imaging was performed from both top and bottom after rotating the sample 180°. By changing the detection lens, it is possible to adapt the system to different samples: low magnification is capable of imaging the whole brain (Figure 1.16C), while for smaller, dissected parts, such as the hippocampus, higher magnification with higher resolution is more appropriate (Figure 1.16D). With this configuration individual cell-cell contacts can be recognized (Figure 1.16E), and even dendritic spines can be visualized (Figure 1.16F).

Although light-sheet microscopy is highly suitable for imaging cleared specimens, even entire mice [90], brain imaging in live animals is more challenging due to the two-objective setup of a conventional SPIM microscope. Two light-sheet-based methods, however offer a solution for this, axial plane optical microscopy (APOM) [91] and swept confocally-aligned planar excitation (SCAPE) [92] both use only a single objective to generate a light-sheet and detect the fluorescence as well. This is done by rotating the detection plane at an intermediate image (APOM), or by rotating both the light-sheet and detection

1.4 Light-sheet imaging of mammalian development

plane simultaneously (SCAPE).

Chapter 2

Image compression

Light-sheet microscopy is capable of generating an immense amount of data in a short amount of time. For this reason not only fast data processing, but data compression also plays an important role when evaluating, sharing and storing the images. In this chapter we will briefly introduce the core concepts of image compression and show some examples as a background for Chapter 4. For a more comprehensive review on data compression fundamentals, the interested reader is referred to the works of Sayood [93], and Salomon and Motta [94].

There are two distinct ways of data compression: lossless and lossy. This is an important difference, and the choice between the two greatly depends on the application itself. For some types of data no loss is acceptable, for example computer programs or text. Here, even a small change could drastically influence the meaning of the original data. For other applications, such as audio and video compression, some loss can be tolerated as long as there is no perceived change or distortion. For scientific applications mostly lossless compression is used. Even for image data, where lossy compression can significantly increase the compression ratio (original size / compressed size), lossy compression is usually not recommended, as it can alter the measurement results in unpredictable ways [95].

2.1 Basics of information theory

As compression is the art of reducing the size of a message while keeping the same amount of information, it is necessary to briefly discuss the theory behind information, and how to quantify it. These concepts were first introduced by Shannon, in his highly influential papers [96–98]. As a rigorous mathematical explanation is outside the scope of this work, we refer the interested reader to the aforementioned works.

Informally, information can be quantified as the amount of surprise. A statement, if it has a high probability, carries a low amount of information, while if it has a small

probability, there is more information. Consider the following example: “It is July”. If it is indeed July, this statement doesn’t provide too much information. Continuing with “It is snowing outside”, carries more information, as it is unexpected under the circumstances (provided the conversation takes place on the Northern Hemisphere).

The self-information of event A can be defined the following way:

$$I(A) = \log_b \frac{1}{P(A)} = -\log_b P(A), \quad (2.1)$$

where $P(A)$ is the probability of event A occurring. The base of the logarithm can be chosen freely, but usually the preferred base is $b = 2$. With this choice, the unit of information is 1 bit, and $I(A)$ represents how many bits are required to store the information contained in A .

The average self-information, also called entropy, for a random variable X can be calculated based on the self-information of the outcomes A_i :

$$H(X) = \sum_i P(A_i)I(A_i) = -\sum_i P(A_i) \log_b P(A_i) \quad (2.2)$$

If we consider a data stream S , where each symbol records the outcome of independent, identical random experiments X , then the average information in each symbol will be $H(X)$. As a consequence, as stated by Shannon’s source coding theorem [96], the shortest representation of S will require at least $N \cdot H(X)$ bits, where N is the number of symbols in the stream. This defines the theoretical lower bound that any naïve compression algorithm, also called entropy coding, can achieve without loosing any information.

The requirement, however, is that the symbols are independent of each other, which is usually not true for most of the data types we (humans) are interested in. In order to achieve ideal compression, the input needs to be modeled, or transformed, to represent it as a sequence of independent variables. This pattern of modeling and coding [99] is the core of all modern compression algorithms. The following sections will briefly introduce these concepts by two examples: Huffman coding, and pixel prediction.

2.2 Entropy coding

Entropy coding algorithms aim to reduce data size and reach the limit of entropy for any kind of input based on the probability distribution of the possible symbols. All of these algorithms work in a similar way, as their aim is to represent the symbols of the input data by codewords in a way to minimize the overall length of the data. Variable length codes, for example, replace the more common symbols with short codewords, while for less frequent symbols they use longer codewords. The ideal length of a codeword for symbol A is actually equal to $I(A)$, as this was the definition of self-information.

Table 2.1: Examples of a random binary code (#1) and a prefix-free binary code (#2). Code #2 is uniquely decodable, while for code #1 it is necessary to introduce boundaries between codewords to be able to distinguish them.

Letter	Code #1	Code #2
a_1	0	10
a_2	11	11
a_3	00	00
a_4	10	010
a_5	111	011

Prefix-free codes

Fixed-length codes have the convenience that there is no need to indicate the boundaries between them, as they are all the same length (*e.g.*, 8 bits for ASCII codes). For variable length codes, as the name implies this is not possible, which necessitated the development of various strategies to demarcate these codewords.

One way to indicate the end of a codeword is to use a specific delimiting sequence which is not part of any of the codewords. While this is an obvious solution, it is also wasteful, as these sequences will not contain any information regarding the original source. Prefix-free codes were developed to be able to omit these sequences, while still allowing unique decodability, making them very popular. This is achieved by making sure that once a codeword was assigned, no other codeword would start with that sequence. In other words, no codeword is a prefix of another codeword, hence the name of the technique. During decoding the bits are read until a valid codeword is matched. Since it is guaranteed that no other codeword will start with the same sequence, the decoder can record the symbol corresponding for that codeword, and continue reading the compressed stream.

Let's take the example in Table 2.1. Five letters are coded in binary code by Code #1 and by Code #2. Code #1 is not a prefix code, and because of this when reading the encoded sequence we can not be sure when we reach the end of a codeword. Decoding the sequence 0000 for example could be interpreted as 4 letters of a_1 or 2 letters of a_3 . For Code #2 it is clear that the sequence decodes to 2 letters of a_3 .

Huffman coding

Huffman coding is a prefix-free, optimal code that is widely used in data compression. It was developed by David A. Huffman as a course assignment in the first ever course on information theory at MIT, and was published shortly afterwards [100]. It is able to achieve optimal compression in a sense that no other prefix-free codes will produce a shorter output. Due to its simplicity combined with a good compression ratio it is still

Table 2.2: Letters to be Huffman coded and their probabilities.

Letter	Probability	Codeword
a_2	0.4	$c(a_2)$
a_1	0.2	$c(a_2)$
a_3	0.2	$c(a_2)$
a_4	0.1	$c(a_2)$
a_5	0.1	$c(a_2)$

widely used in many compression algorithms, such as in JPEG, bzip2, or DEFLATE (zip) [94].

The Huffman coding procedure is based on two observations regarding optimal and prefix-free codes:

1. For a letter with higher frequency the code should produce shorter codewords, and for letters with lower frequency it should produce longer codewords.
2. In an optimum code, the two least frequent codewords should have the same lengths.

From these statements it is trivial to see that the first is correct. If the more frequent letters would have longer codewords than the less frequent letters, then the average codeword length (weighted by the probabilities) would be larger than in the opposite case. Thus, more frequent letters must not have longer codewords than less frequent letter.

The second statement at first glance might not be so intuitive, so let's consider the following situation. Let's assume that the two least frequent codewords do not have the same lengths, and the least frequent is longer. However, because this is a prefix code, the second longest codeword is not a prefix of the longest codeword. This means that if we truncate the longest codeword to the same length as the second longest, they will still be distinct codes and uniquely decodable. This way we have a new coding scheme which requires less space on average to code the same sequence as the original code, from which we can conclude the original code was not optimal. Therefore, for an optimal code, statement 2 must be true.

To construct such a code, the following iterative procedure can be used. Let's consider an alphabet with five letters $A = [a_1, a_2, a_3, a_4, a_5]$ with $P(a_1) = P(a_3) = 0.2$, $P(a_2) = 0.4$ and $P(a_4) = P(a_5) = 0.1$ (Table 2.2). This distribution represents a source with 2.122 bits/symbol. Let's order the letters by probability, and consider the two least frequent. Since the codewords assigned to these should have the same lengths, they can be assigned

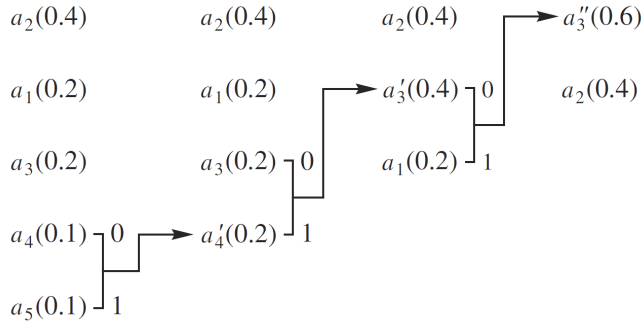


Figure 2.1: Building the binary Huffman tree. The letters are ordered by probability, these will be the final leaves of the tree. To create the branches, at every iteration we join the two nodes with the smallest probability, and create a new common node with the sum of the probabilities. This process is continued until all nodes are joined in a root node with probability of 1. Now, if we traverse down the tree to each leaf, the codeword will be defined by their position.

as

$$\begin{aligned} c(a_4) &= \alpha_1 * 0 \\ c(a_5) &= \alpha_1 * 1 \end{aligned}$$

where $c(a_i)$ is the assigned codeword for letter a_i and $*$ denotes concatenation. Now we define a new alphabet A' with only four letters a_1, a_2, a_3, a'_4 , where a'_4 is a merged letter for a_4 and a_5 with the probability $P(a'_4) = P(a_4) + P(a_5) = 0.2$. We can continue this process of merging the letters until all of them are merged and we have only one letter left. Since this contains all of the original letters, its probability is 1. We can represent the end result in a binary tree (see Figure 2.1), where the leaves are the letters of the alphabet, the nodes are the merged letters, and the codewords are represented by the path from the root node to each leaf (compare with Table 2.3). The average length of this code is

$$l = 0.4 \times 1 + 0.2 \times 2 + 0.2 \times 3 + 0.1 \times 4 + 0.1 \times 4 = 2.2 \text{ bits/symbol} \quad (2.3)$$

The efficiency of a code can be measured by comparing the average code size to the entropy of the source. For this example, the difference is 0.078 bits/symbols. As the Huffman code operates in base 2, it will produce a code with zero redundancy when the probabilities are negative powers of 2.

Limitations of Huffman coding

Although the Huffman code is optimal among variable-length codes, for certain types of data its compression ratio may be low. This limit lies in the fact that the length of the shortest code assignable is one. For certain types of data with very low entropy this will

Table 2.3: Huffman code table.

Letter	Probability	Codeword
a_2	0.4	1
a_1	0.2	01
a_3	0.2	000
a_4	0.1	0010
a_5	0.1	0011

result in a relatively high redundancy. Arithmetic coding offers an alternative here, as contrary to Huffman coding, it does not rely on substituting symbols with codewords, and thus can compress very low entropy data with minimal redundancy. This coding method maps the whole message to a single number with arbitrary precision in the interval of 0 to 1. A more detailed description of arithmetic coding is given in [93].

Another alternative for compressing very low entropy data is run-length encoding. This coding method assumes that the same character appears in the message many times consecutively, and instead of storing each of these individually, it counts the number of identical symbols in a single run, and encodes the run-length together with the symbol. As this strategy is only efficient for very low entropy data, it is a common practice to combine run-length encoding with Huffman coding to construct a low redundancy coder for a wide range of input data.

2.3 Decorrelation

Since entropy coding doesn't assume anything about the data structure, it is not capable of recognizing and compressing any regular patterns or correlations between the consecutive data points. To maximize the efficiency of compression, any correlations should be removed from the data before it is fed to the entropy coder. Here we will briefly discuss some decorrelation strategies for image compression that aim to improve the performance of a successive entropy coder.

Transform coding

Very popular methods for decorrelation are the transformations that represent the data as a decomposition of orthonormal functions. One of the most common of these transformations is the Fourier transform, which represents a periodic signal as a sum of sine and cosine functions. As most natural images are of continuous tone, the idea behind this is that most of the information will be captured by just a few Fourier coefficients. As a result, compressing the coefficients with an entropy coder should result in a smaller output than encoding the original data.

For practical purposes, instead of the discrete Fourier transform (DFT), the discrete cosine transform (DCT) [101] is usually used in image compression applications. This is very similar to DFT, the difference being the periodic extension of the signal. In the DCT transform the image is mirrored on the sides instead of just repeated, to avoid large jumps at the boundaries that may introduce unwanted high-frequency components in the Fourier transform. If the image is extended in a symmetric way, the Fourier transform will be able to represent the data with only cosine functions, hence the name discrete cosine transformation.

One drawback of frequency-based transformations is that they can't capture any spatial information, as their base functions are periodic for the whole domain. This can have a negative impact on image compression ratio. For example, if the image contains a single sharp edge, a high frequency base function will need to have a large coefficient. Since this will affect the entire image, other, lower frequency bases will also need to have increased coefficients to negate the unwanted effects. To overcome this limitation, the DCT is usually performed on small chunks of the image, such as on 8×8 blocks in the JPEG compression. The other option is to use non-periodic base functions to represent the signal. One good example for this is the use of wavelets, and based on this, the discrete wavelet transform (DWT) [102, 103].

As both DCT and DWT operate with floating-point coefficients (although DWT has integer-based variants), the inverse transformation is not guaranteed to exactly reconstruct the original data. This is due to the finite machine precision of floating-point numbers. Due to this fact these transformations are generally used in lossy compression algorithms, and the coefficients are quantized based on the required image quality.

Predictive decorrelation

Another family of decorrelation methods is based on predicting the values of each data point (or pixel) depending on the context of the neighboring values. These techniques are based on differential pulse code modulation (DPCM), a decorrelation method originally used for audio compression. Here, before the data stream is entropy coded, a prediction is made for each value, which is equal to the preceding value. The difference to the prediction, called the prediction error, or prediction residual (ε) is passed to the entropy coder.

To see how why such an algorithm can increase compression ratio, let's consider the following sequence:

37	38	39	38	36	37	39	38	40	42	44	46	48
----	----	----	----	----	----	----	----	----	----	----	----	----

Although there is no obvious pattern in this sequence, there are no sharp jumps between the consecutive values, and this can be exploited by using a prediction scheme. Let's

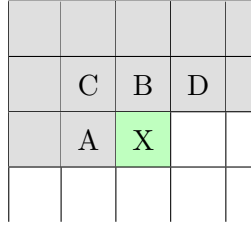


Figure 2.2: Context for pixel prediction. X is the current pixel to be encoded and the previously encoded pixels are indicated with gray background. To allow for decoding, only the already encoded pixels are used for the prediction, typically the nearest neighbors (A, B, C, D).

define the prediction $\text{Pred}(\cdot)$ for each element X_k to be equal to the preceding element. The prediction error would be $\varepsilon_k = X_K - \text{Pred}(X_k) = X_k - X_{k-1}$:

37	1	1	-1	-2	1	2	-1	2	2	2	2	2
----	---	---	----	----	---	---	----	---	---	---	---	---

As apparent from this new sequence, the number of distinct values are reduced, which means that fewer bits can represent this sequence than the original. When running these two sequences through an entropy coder, the error sequence will be much more compressed due to this property.

Using a predictive scheme to remove correlations from neighboring elements is a very good strategy for various applications where this signal is only slowly changing. It has been successfully implemented in audio and image compression algorithms as well, such as lossless-JPEG [104], JPEG-LS [105], CALIC [106], SFALIC [107] and FLIC [108], just to name a few.

For image compression, as the datasets are inherently multi-dimensional, the prediction rules can also be multi-dimensional, which can better capture the structure of the data, and achieve better decorrelation. For a typical encoding scenario, where the pixels are encoded one by one, the prediction can be based on the already encoded values (gray in Figure 2.2). This causality constraint is necessary in order to be able to decode the image.

Usually the nearest neighbors are used for the prediction, but this is not a necessity; CALIC, for example, uses the second neighbors [106], and the third dimension can also be utilized if the data structure allows this, for example when encoding hyperspectral recordings [109].

The lossless part of the JPEG standard specifies 7 possible rules for the prediction

step [104]:

$$\begin{aligned}\text{Pred}_1(X) &= A \\ \text{Pred}_2(X) &= B \\ \text{Pred}_3(X) &= C \\ \text{Pred}_4(X) &= A + B - C \\ \text{Pred}_5(X) &= A + (B - C)/2 \\ \text{Pred}_6(X) &= B + (A - C)/2 \\ \text{Pred}_7(X) &= (A + B)/2\end{aligned}$$

Depending on the patterns of the input image, some predictors can perform better than others. For general use, predictor 4 or 7 are recommended, as these are not direction dependent, and usually perform best. Predictor 7 is just the mean of the top and left neighbors, while predictor 4 assumes that the values for pixels A, B, C and X are on the same plane, and calculates the prediction based on this.

Other algorithms try to improve the prediction by adapting it depending on the local texture. The LOCO-I algorithm (part of JPEG-LS), for example, uses the median edge detector [105]:

$$\text{Pred}(X) = \begin{cases} \min(A, B) & \text{if } \geq \max(A, B) \\ \max(A, B) & \text{if } \leq \min(A, B) \\ A + B - C & \text{otherwise} \end{cases} \quad (2.4)$$

This function tries to estimate if there is an edge close to X. If it detects a vertical edge to the left of X, it picks B for the prediction, whereas if it detects a horizontal edge above X it tends to pick A. If no edge is detected, the prediction is the same as predictor 4 of the lossless JPEG standard.

A useful property of the prediction-based methods is that there is no base change as in the transform coding methods, and it is possible to construct bounded lossy compression algorithms. JPEG-LS, for example defines a near-lossless mode of operation, where the user can select the maximum absolute reconstruction error per pixel. This is achieved by quantizing the prediction residual ε with a quantization step depending on the allowable error. Since the decoding algorithm simply calculates $\hat{X} = \text{Pred}(X) + \varepsilon$, any quantization error of ε is directly reflected in the reconstructed pixel value. Since the quantization error is known, and bounded by the quantization step size, the maximum reconstruction error for each pixel is also bounded. This mode is sometimes used for medical imaging applications, where the preservation of diagnostic quality is required by law, but higher compression ratios are desired than what is possible by lossless compression.

Chapter 3

Dual Mouse-SPIM

Unraveling the secrets of mammalian development has been a long standing challenge for developmental biologists and medical professionals alike. This phase of early life is an incredibly complex and dynamic process spanning through large scales in space and time. Subcellular processes at the nanoscale are happening in the range of milliseconds or shorter, while whole embryo reorganizations and tissue migration events take place over the course of hours [110]. Resolving these processes presents a true challenge, since to understand the underlying mechanisms, molecular specificity is just as crucial as high spatial and temporal resolution. As we have seen in Chapter 1, live imaging of mouse embryonic development is an especially challenging task, but light-sheet microscopy can offer a good solution owing to its gentle optical sectioning and fast image acquisition. The Mouse-SPIM [J2] introduced earlier (Section 1.4.1) also solves the issue of live imaging with its inverted design: the embryos are held by a foil which not only allows easy sample handling but also acts as a barrier that isolates the embryos from the immersion medium.

As all microscopes, the Mouse-SPIM also had to make a compromise: although its design allows for long-term live imaging, it only has a single detection view, as rotation is not possible with the sample mounting trays. Due to this configuration, its resolution is inherently anisotropic, having an axial-to-lateral resolution ratio of around 3. Although this is sufficient for many applications, such as cell tracking, for detecting subcellular features it might be limiting. One such example is chromosome tracking, which could shed light on chromosome missegregation mechanisms in the early embryonic development, which is the cause of many congenital diseases also affecting humans.

In this chapter, we present a novel light-sheet microscope developed to address the above challenges by using high NA objectives for subcellular isotropic resolution and low-light imaging, while offering multi-view detection without the need to rotate the samples. The microscope is designed to be live imaging compatible, offering new perspectives in the research of mouse embryonic development. This chapter will describe the design concepts for the microscope, the optical layout, alignment strategies, the results of various

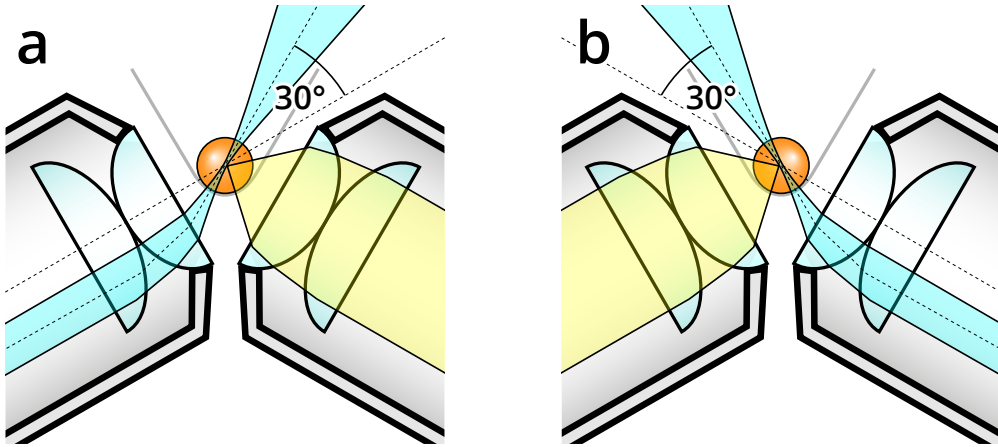


Figure 3.1: Dual view concept with high NA objectives. To achieve multi-view detection while maximizing resolution and light collection efficiency, two high NA objectives are placed in 120° arrangement. The sample (orange) is held from below by a thin FEP foil. To be able to overlap the light-sheet with the focal plane, the light-sheet is tilted by 30° . The objectives are used in an alternating sequence for illumination and detection.

performance measurements, and its multi-view imaging capabilities.

3.1 Microscope design concept

As the limiting factor for subcellular imaging with the original Mouse-SPIM is the poor axial resolution relative to the lateral, our first aim was to increase the axial resolution to ideally reach the lateral resolution. A common way to reach isotropic resolution is to image a specimen from multiple directions, and combine the resulting images by multi-view deconvolution [28, 111, 112]. This has the benefit that the high-resolution information from one view can complement the low axial resolution of the other view, thus providing better resolution in all three directions.

As described in Chapter 1, many SPIM implementations allow for recording multiple views either by rotating the sample, or by surrounding the sample with multiple objectives that are used for detection (Figure 1.10). For our setup, following the sample mounting technique of the original Mouse-SPIM, we wanted to keep the open-top sample mounting possibility, as this was proven to be highly compatible with mouse embryo imaging. To achieve multi-view detection in this configuration, we designed a setup where both objectives can be used for illumination and detection in a sequential manner, inspired by previous symmetrical SPIM designs [43, 113].

To achieve the highest possible resolution from two views, the core of our design is based on the symmetric arrangement of two Nikon CFI75 Apo LWD 25x water-dipping objectives, with a numerical aperture of 1.1. Due to the large light collection angle of these objectives, we arrange them in 120° instead of the conventional 90° used for light-sheet imaging. As the light-sheet still needs to coincide with the imaging focal plane

3.1 Microscope design concept

of the objectives, we tilt the light-sheet by 30° (Figure 3.1). Due to the low NA of the light-sheet, this is possible without affecting illumination quality.

This 120° arrangement has several benefits when compared to the traditional 90° configuration. When placing the objectives in 90° the largest possible light collection half-angle for an objective can be $\alpha_{max,90} = 45^\circ$, and the corresponding NA is $NA_{max,90} = n \cdot \sin \alpha_{max,90} = 0.94$, where $n = 1.33$ is the refractive index of water. Considering that this is an idealized case, the practically available highest NA is only 0.8. For a 120° arrangement, the theoretical maximum is $NA_{max,120} = n \cdot \sin(120^\circ/2) = 1.15$, with a practical maximum NA of 1.1.

Although the resolution won't be completely isotropic when combining the images from two 120° views (Figure 3.2), as it is for 90° views, due to the higher maximum NA possible, the resolution can be higher in the 120° case. When simulating the combined multi-view PSFs (Figure 3.2), for 0.8 NA objectives in 90° the axial and lateral resolutions are both 317 nm; while for two 1.1 NA objectives in 120° the axial resolution will be identical, 317 nm, and the lateral will be better, 193 nm.

Although this difference in resolution may seem marginal, the 120° configuration has another advantage in light collection efficiency. Collecting as much of the fluorescence signal as possible is crucial in live imaging applications, due to the limited available photon budget (see Figure 1.1 and [8]). Collecting more light from the sample allows to image faster with the same contrast, or allows to reduce the illumination power and maintain the imaging speed. As light collection efficiency depends on the solid angle subtended by the detection lens, (see Appendix Section C), a 1.1 NA objective can collect twice as many photons as a 0.8 NA objective, which gives the 120° setup a clear edge in low-light imaging.

3.1.1 Light-sheet design

To allow for flexibility in the field of view height, to achieve even illumination, reduced stripes, and have the potential for confocal line detection, we opted to use the beam-scanning technique to generate a virtual light-sheet. The effective focal length of the Nikon 25x objective, given the 200 mm focal length tube lens is

$$f_o = \frac{f_{tl}}{M} = \frac{200 \text{ mm}}{25} = 8 \text{ mm}, \quad (3.1)$$

and the back aperture diameter is $d = 17.6 \text{ mm}$.

To generate the tilted light-sheet as shown on Figure 3.1, the illumination beam will need to be displaced by

$$\delta = f_o \cdot \tan 30^\circ = 4.62 \text{ mm} \quad (3.2)$$

Since the Gaussian beam is not uniform, only a smaller portion of it can be used to

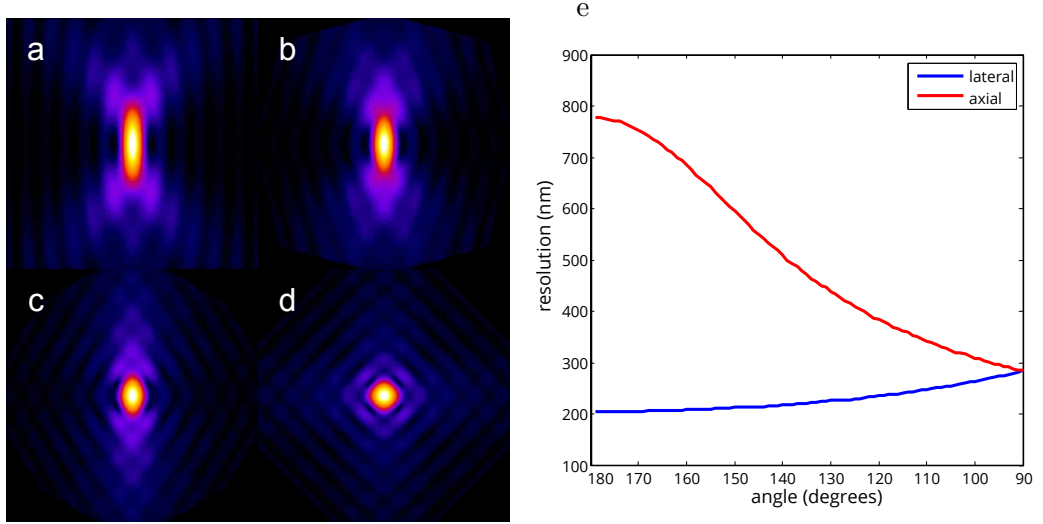


Figure 3.2: Lateral and axial resolution of a multi-view optical system. a) Simulated PSF for a single view. b)–d) Simulated compound PSF of two views aligned in b) 150, c) 120 and d) 90 degrees to each other. e) Axial and lateral resolution of a dual-view setup depending on the rotation angle of the two objectives. Parameters used for calculations: NA=1.1, $\lambda_{ex} = 488\text{nm}$, $\lambda_{det} = 510\text{nm}$, $n = 1.333$ for water immersion.

maintain an even illumination (Figure 1.12a). Because the size of an early mouse embryo is around $80\text{ }\mu\text{m}$, we require the length and the height of the light-sheet to be at least $100\text{ }\mu\text{m}$.

The length and thickness of the light-sheet

As we saw in Section 1.3.1, the length of the light-sheet is determined by the Rayleigh-range of the beam in the zy -plane. Since $l_{\text{FOV}} = 2 \cdot z_R = 100\text{ }\mu\text{m}$

$$z_R = 50\text{ }\mu\text{m}. \quad (3.3)$$

Since the Rayleigh range and the diameter of the beam waist are coupled, the light-sheet thickness can be calculated after rearranging Equation 1.20:

$$2 \cdot W_0 = 2 \cdot \sqrt{\frac{z_R \cdot \lambda}{\pi}} = 5.57\text{ }\mu\text{m} \quad (3.4)$$

when $\lambda = 488\text{ nm}$ for GFP excitation. As the beam width for these calculations is defined as $1/e^2$ of the peak intensity, we also calculate the more commonly used full width at half maximum (FWHM):

$$\text{FWHM} = W_0 \cdot \sqrt{2 \ln 2} = 3.28\text{ }\mu\text{m}. \quad (3.5)$$

3.2 Optical layout

From this, the divergence angle of the beam is

$$\theta_0 = \frac{\lambda}{\pi W_{0,y}} = 55.74 \text{ mrad} = 3.196^\circ \quad (3.6)$$

This means, the numerical aperture needed to produce this light-sheet is:

$$\text{NA}_{ls} = n \cdot \sin(\theta_0) = 0.0743 \quad (3.7)$$

Since $\text{NA} = 1.1$, the diameter of the back aperture is $d = 17.6 \text{ mm}$ and the divergence angle $\theta_0 \ll 1$, using paraxial approximation, the necessary beam width at the back focal plane in the y direction is

$$b_y = d \cdot \frac{\text{NA}_{ls}}{\text{NA}} = 1.19 \text{ mm} \quad (3.8)$$

Thus, to generate a light-sheet with appropriate length to cover a whole mouse pre-implantation embryo, the laser beam diameter should be $b = 1.19 \text{ mm}$. Larger diameters will result in a more focused beam and a shorter light-sheet, while a smaller diameter beam will have worse optical sectioning capabilities, but will provide a larger field of view.

The height of the light-sheet

The height of the light-sheet can be adjusted by changing the beam scanning amplitude with the galvanometric mirror (also referred to as scanner). To scan the entire height of the field of view of $h_{\text{FOV}} = 270 \mu\text{m}$, the scanning angle range at the back focal plane of the objective will need to be $\theta = \tan^{-1}(h_{\text{FOV}}/2/f_o) = \pm 0.967^\circ$.

3.2 Optical layout

Based on the requirements and other considerations shown in the previous sections, the microscope was designed in three main parts: 1) the core unit (green), 2) illumination branches (blue) and 3) detection branches (yellow, Figure 3.3). The aim when integrating these units together was to allow for high level of flexibility with robust operation, while also keeping efficiency in mind. After finalizing the concept, the mechanical layout of the microscope was designed in SolidWorks.

3.2.1 Core unit

As the most important part of the microscope is actually the sample, the design is based around a core consisting of the imaging chamber and the objectives (Figure 3.4). Also part of the core are two mirror blocks placed at the back of the objectives, and three

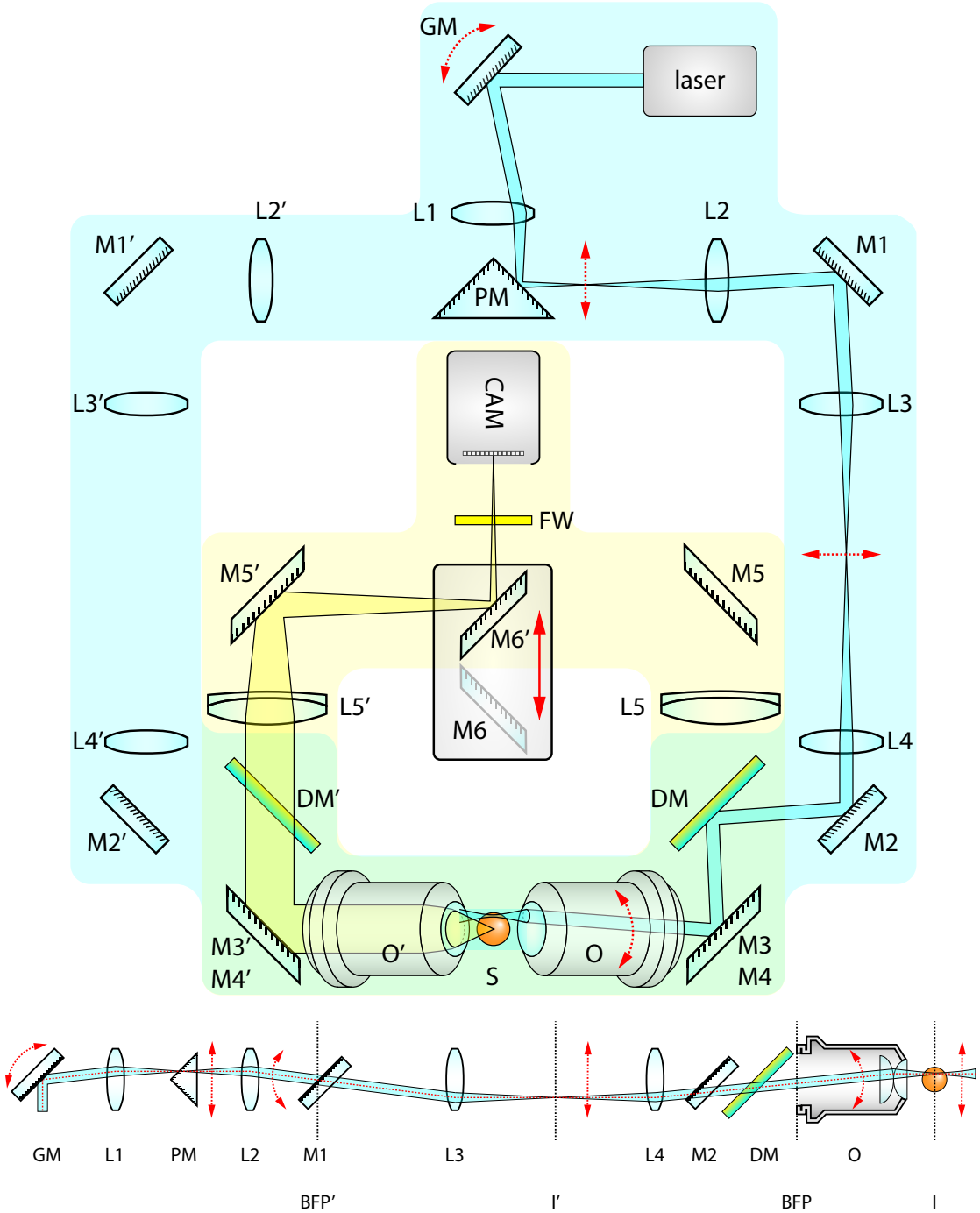


Figure 3.3: Dual Mouse-SPIM optical layout. The microscope consists of two main parts, the illumination branches (blue) and detection branches (yellow). For both illumination and detection there are two identical paths implemented. Illumination direction can be changed by applying a different offset to the galvanometric mirror, which in turn will direct the beam to the opposite face of the prism mirror. L1 and L2 will then image the scanner on M1. Using L3 as a scan lens, and L4 as a tube lens, the scanned beam is coupled into the objective path by a quad band dichroic mirror. CAM – camera, DM – dichroic mirror, FW – filter wheel, L – lens, M – mirror, O – objective, PM – prism mirror, S – sample

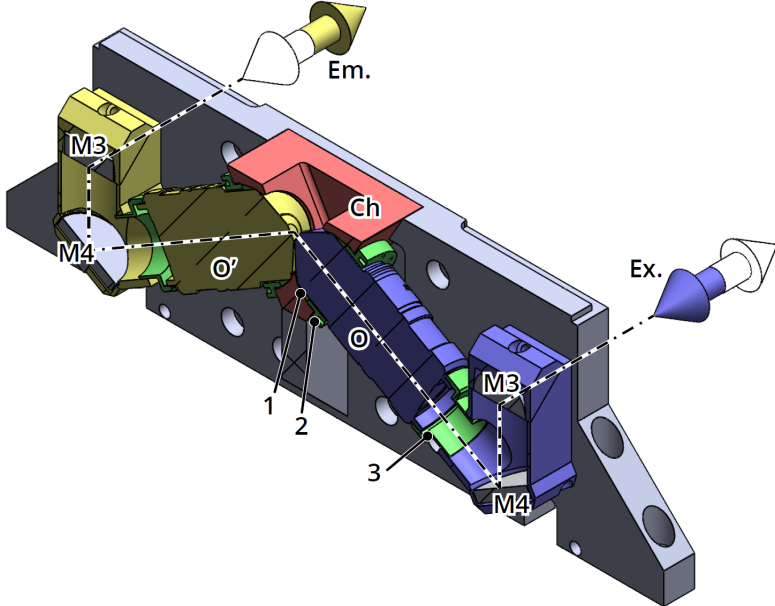


Figure 3.4: The core unit of the microscope. The two objectives (O and O') are mounted on a solid 15 mm thick aluminium plate. Fitting on the objectives, a custom chamber (Ch) is holding the immersion medium for imaging. The mirror block with mirrors $M3$ and $M4$ directs the light to 65 mm optical rails. Excitation (Ex.) and emission (Em.) light paths are indicated by the dash-dot line. Due to the symmetric arrangement, the excitation and illumination paths can be alternated. The objectives are secured with rings 1–3 (green, see main text for details).

custom-designed rings to hold the objectives in place. The objectives are pointing slightly upwards, closing a 60° angle with the horizontal plane, and 120° angle with each other.

Chamber

The chamber serves two purposes: it holds the immersion liquid necessary for imaging, and it keeps the objectives in the 120° position. The objectives are held by their necks as opposed to the standard mounting method, which is from the back, by the threads. The advantage of this is that any axial movements due to thermal expansion are greatly reduced, thus the focal plane position is more stable even when changing the imaging conditions.

The chamber is machined from a high-performance plastic, polyether ether ketone (PEEK). This material has many beneficial properties: it is food safe, chemically extremely inert, and resistant to most solvents used in a biology laboratory. Due to these properties, PEEK is live imaging compatible, even for sensitive samples, as it can also be autoclaved. Compared to other plastics its mechanical properties are also superior. It has high tensile and compressive strength, comparable to those of aluminium, low thermal expansion and low thermal conductivity. This can be beneficial when implementing temperature control, as thermal loss is reduced.

The objectives are kept in place by two custom-designed rings (Figure 3.4 1, 2).

The first ring has a cross sectional shape of a wedge, and sits tightly against both the objective and the wall of the chamber. The second ring can freely slide on the objective, and has threads matching the chamber. When turned in, the threaded ring pushes the wedge ring further in, which in turn presses against the objective and the chamber wall uniformly, thus preventing the objective from moving, and sealing the chamber at the same time. As the wedge ring is made from a soft plastic (delrin), it will press evenly against the objective preventing any damage. Given the conical shape of the ring, it will also automatically center the objective, ensuring correct positioning.

To relieve any rotational stresses from the objective, the back of the objective is also supported by the mirror block. This is not fixed, however. A third ring, made of PEEK is threaded on the objective, and slides into the opening of the mirror block. This reduces the forces on the objectives, while still allows for some movements that might occur in the axial direction due to thermal expansion.

Mirror blocks

Apart from supporting the objectives from the back, the mirror blocks are housing two broadband dielectric mirrors (Thorlabs, BBE1-E03 and OptoSigma, TFMS-30C05-4/11) to direct the light to and from the objectives on a standard 65 mm height, compatible with the Owis SYS65 rail system. The combination of two mirrors have two benefits compared to using just one. With a single mirror directly reflecting the light to the back, the entire assembly would need to be much higher to reach the desired 65 mm height. This could result in stability problems. Furthermore, due to the 60° rotation angle of the objective, the image of the objective would also be rotated if using only a single mirror. With two mirrors the reflection planes can be kept orthogonal to the optical table, which will result in a straight image after the mirror block. This is not only beneficial when recording the images, but also when aligning the illumination arm. With the use of two mirrors, a convenient vertical scanning is required to produce the light-sheet; with a single mirror, the scanning direction would need to be rotated by 60°.

3.2.2 Illumination

The illumination arm of the microscope directs and shapes the laser beam to generate the proper light-sheet dimension at the sample. As was calculated in Section 3.1.1, a beam diameter of 1.2 mm is ideal for this setup.

The illumination arm has three main roles:

1. expands the laser beam to the required size.
2. images the galvanometric scanner to the back focal plane of the objective
3. switches the laser light between the two objectives during imaging

3.2 Optical layout

To achieve the desired beam diameter, a 1:2 beam expander (Sill Optics, 112751) is used in the reverse direction. As the output of the laser fiber produces a 3 mm diameter beam, this will reduce it to 1.5 mm. As this is already the required beam diameter, the lenses further in the illumination path will not introduce any magnification.

Switching between the two illumination arms is performed by a custom-designed beam splitter unit (Figure 3.5). Instead of utilizing a 50/50 beam splitter cube and mechanical shutters, we exploit the fact that a galvanometric scanner is needed to generate the light-sheet. As this galvanometric scanner (Cambridge Technology, 6210B) has a relatively large movement range ($\pm 20^\circ$) it is also suitable for diverting the beam from one illumination arm to the other.

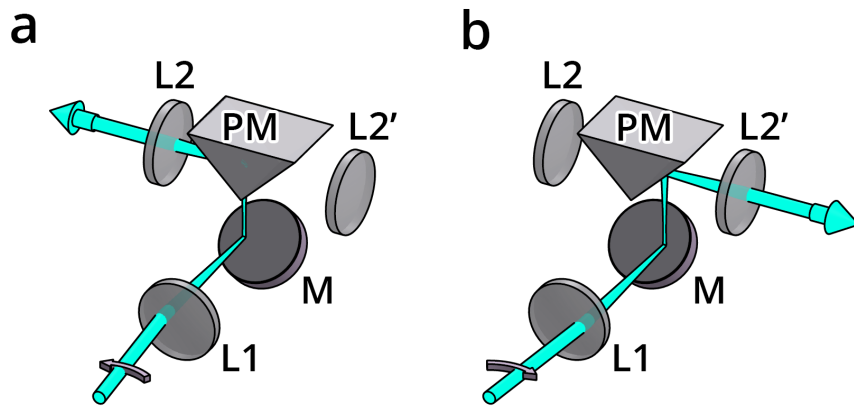


Figure 3.5: Illumination branch splitting unit. To divert the beam to either side, a right angle prism mirror is used in conjunction with a galvanometric scanning mirror. L1 acts as a scan lens, thus the beam is translated on mirror M. Depending on the scanner angle, the beam will be reflected either to the left (a) or to the right (b). L2 and L2' act as relay lenses, and will image the scanner movement to the corresponding intermediate planes.

Switching illumination side is done the following way. As the scanner is positioned at the focus of the first lens (L1, $f_1 = 75$ mm, Edmund Optics, #47-639), the rotational movement will result in a linear scanning movement on mirror M and the prism mirror PM (Figure 3.5). Depending on the lateral position of the beam, it will hit either the left or the right leg of the prism (Thorlabs, MRAK25-E02), and will be reflected to either direction. As the galvanometric mirror can be precisely controlled through our custom software, we can set and save the position when the beam is centered on the left lens L2 ($f_2 = 75$ mm, Edmund Optics, #47-639) (Figure 3.5a) and the position when the beam is centered on the right lens L2' (Figure 3.5b). Lenses L1 and L2(L2') form a 1:1 relay system, and are imaging the scanner on mirror M1(M1') (Figure 3.3). This way we can use the same scanner to generate the light-sheet for both directions, depending on the initial offset position. This not only has the advantage of being able to electronically switch the illumination arms, but only requires a single galvanometric scanner instead of one for each arm.

Due to the arrangement of the bottom mirror and the prism mirror the scanning direction will be rotated by 90°. This will result in a vertical scanning plane, which is exactly what we need to generate the light-sheet on the sample (see Section 3.2.1). Further following the illumination path, two achromatic lenses L3 and L4 ($f_3 = f_4 = 200\text{ mm}$) form a 1:1 relay, imaging the scanning axis to the back focal plane (BFP) of the objective.

3.2.3 Detection

As the emitted light exits the objective and the mirror block, it is spectrally separated from the illumination laser light by a quad band dichroic mirror (DM, Semrock, Di03-R405/488/561/635-t3-25x36) matching the wavelengths of the laser combiner. The light is then focused by a 400 mm achromatic lens (L5, Edmund Optics, #49-281) onto the camera sensor (Andor Zyla 4.2 sCMOS). Just before the camera, a motorized filter wheel (FW, LEP 96A361) is placed to discriminate any unwanted wavelengths from the emission light. Although this is not in the infinity space, due to the very small angles after the 400 mm tube lens, the maximum axial focal shift is $\sim 50\text{ nm}$ only, which is negligible compared to the axial resolution of $\sim 1.1\text{ }\mu\text{m}$.

Similarly to the common scanner in the illumination path, the two detection arms share the same camera. Although two cameras could also be used, due to the operating principle of the microscope, the two objective are not used for imaging at the same time. This means a single camera is capable of acquiring all the images. However, the two distinct detection arms need to be merged to be able to use a single detector.

Our solution to this problem is a custom-designed view-switching unit comprised of two broadband dielectric elliptical mirrors (Thorlabs, BBE1-E03) facing opposite directions, mounted on a high precision linear rail (OptoSigma, IPWS-F3090). Depending on the rail position, either the left (Figure 3.6a) or the right (Figure 3.6b) detection path will be reflected upwards, to the camera.

Moving the switcher unit is performed by a small, 10 mm diameter pneumatic cylinder (Airtac, HM-10-040) that is actuated by an electronically switchable 5/2 way solenoid valve (Airtac, M-20-510-HN). This solution offers a very fast switching between views, up to 5 Hz, depending on the pressure, and it is extremely simple to control, as only a digital signal is necessary to switch the valve.

3.3 Optical alignment

Precise alignment of the illumination and detection paths are crucial for high quality imaging, and has a pronounced importance for high magnification and high resolution optical systems. Due to the symmetrical setup of the microscope, we will only describe the alignment of one side, as the same procedure is also applicable to the other side.

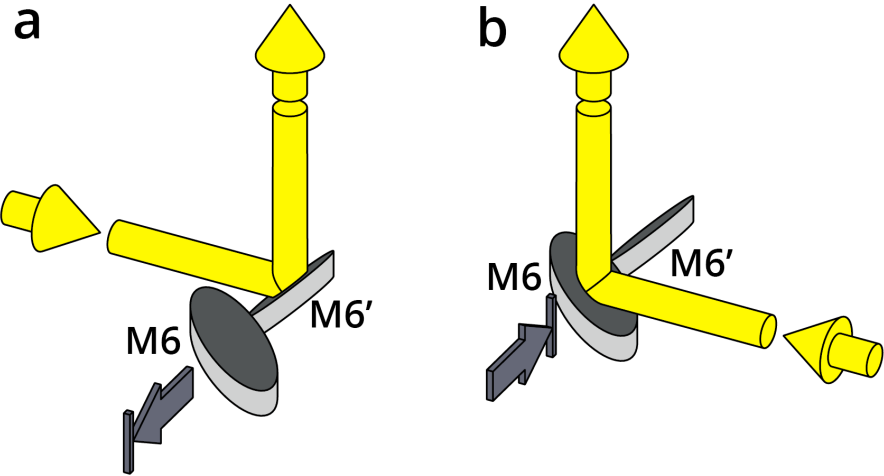


Figure 3.6: Detection branch switching unit. To be able to image both views on the same camera, a moveable mirror unit is introduced. Depending on the imaging direction, the mirror block is either moved backward (a) or forward (b) to reflect the light up to the camera. Since the movement is parallel to the mirrors' surface, the image position on the sensor is not dependent on the exact position of the mirrors.

References to optical components will be as defined in Figure 3.3.

3.3.1 Alignment of the illumination branches

The two illumination branches start with a common light source, a single-mode fiber coupled to a laser combiner, and they also share a galvanometric mirror that performs the beam scanning to generate the virtual light-sheet. Likewise shared is a scan lens focusing on the galvanometric mirror (GM), and the illumination splitter unit (PM, see section 3.2.2).

Alignment of the illumination arms is done in three steps. First the laser beam is aligned on the rail that holds the scanner, lens L1, and the splitter unit PM. This is performed by two kinematic mirrors placed between the fiber output and the galvanometric mirror (not shown on figure). Using these two mirrors it is possible to freely align the beam along all four degrees of freedom: translation in two orthogonal directions and rotation around two orthogonal axes. Beam alignment on the rail is tested by using two irises at the two ends of the rail, if the beam passes through both of them we consider it centered and straight on the optical axis.

After the beam is aligned on the first rail, lens L1 and the splitter unit PM are placed in the measured positions to image the galvanometric mirror on mirror M1 using lenses L1 and L2. Correct positioning of the splitter unit along the rail is crucial, since this will affect the lateral position and tilt of the beam exiting the unit. To some extent this can also be compensated by adjusting the two mirrors before the galvanometric mirror, but should be avoided if possible as this will also displace the beam from the center of the galvanometric mirror.

After the initial alignment of the illumination arms, when the laser is already coupled in the objective, the fine adjustments are performed based on the image of the beam through the other objective. The beam is visualized by filling the chamber with a 0.1% methylene blue solution. As this solution is fluorescent and can be excited in a very large range, it is well suited to visualize the beam during adjustment.

Adjusting beam position Beam position can be adjusted by either translating the beam in a conjugated image plane (I'), or by rotating the beam in a conjugated back focal plane (BFP'). The setup was designed in a way that BFP' coincides with mirror M1. This mirror is mounted in a gimbal mirror mount, allowing to rotate the mirror exactly around its center, which avoids unwanted translational movements, and results in pure rotation of the beam. Lens L3 is positioned exactly 1 focal length away from the mirror, thus acting as a scan lens, and transforming the rotational movements to translation. This translation is further imaged and demagnified by the tube lens L4 and the objective O onto the sample.

Adjusting beam tilt Beam tilt can be adjusted by either rotating the beam in an intermediate image plane (I'), or translating it at the back focal plane (BFP). As mirror M2 is relatively far from the back focal plane, adjusting it will mostly result in translation that will rotate the beam in the image plane. This movement, however, will also introduce translations, and has to be compensated by adjusting mirror M1. The light-sheet needs to be tilted by 30° to coincide with the focal plane of the other objective, but this level of adjustment is not possible with M2. In order to allow for a pure rotation of the light-sheet, we mounted the dichroic mirrors on linear stages (OptoSigma, TSDH-251C). By translating the dichroic mirror, the illumination laser beam gets translated at the back focal plane, which will result in a pure rotational movement at the sample. Coarse alignment of the light-sheet is performed by adjusting the dichroic position while inspecting the light-sheet through a glass window in the chamber. Precise alignment is done afterwards based on the image of the beam visualized in a fluorescent medium.

Adjusting the scanning-plane angle After the beam is properly aligned, *i.e.*, it is in focus and in the center of field of view, it is still necessary to check if the scanning direction is parallel to the imaging plane. It is possible that the beam is in focus in the center position, but when moved vertically it drifts out of focus due to a tilted scanning angle. This tilt can be compensated by mirror M1, which is placed at the conjugate back focal plane BFP' . Between lenses L3 and L4 a magnified version of the light-sheet will be visible, and the tilt can be checked by placing an alignment target in the optical path while scanning the beam. By tilting mirror M1 up or down the scanning pattern not only translates, but it also rotates if the mirror surface is not exactly vertical. Since M1

and GM are in conjugated planes, the tilt and offset can be performed independently. The tilt is first fixed by M1 while inspecting the target, and the beam is re-centered by changing the offset on the galvanometric mirror. Moving the galvanometric mirror will not introduce tilt, since in this case rotation axis is perpendicular to the reflection plane.

3.3.2 Alignment of the detection branches

Since the detection path is equivalent to a wide-field detection scheme, its alignment is much simpler than that of the illumination branches. The only difference is the detection branch merging unit (see Section 3.2.3.) which features two moving mirrors. This, however, doesn't affect the alignment procedure, since the movement direction is parallel to both mirrors' surfaces, meaning that the exact position of the mirrors will not affect the image quality, as long as the mirrors are not clipping the image itself. A stability test was performed to confirm the consistent switching performance of the mirror unit before the final alignment took place (see Section 3.5.1).

Positioning the tube lens The position of the tube lens determines the focal plane that is being imaged on the camera sensor. Ideally, the tube lens's distance from the camera sensor is exactly the tube lens's focal length, which will ensure the best imaging performance. If the tube lens's distance is not correct, the focal plane will be slightly shifted in the axial direction. Small shifts will not necessarily have detrimental effect on the image quality, because the light-sheet can also be shifted accordingly. Because of the shifted focal and image planes, however, the magnification of the system will be affected, and will change depending on the amount of defocus. For this reason we aim for positioning the tube lens as close to the theoretical position as possible.

Our tube lens is a compound, achromatic lens with a center thickness of 12.5 mm, and edge thickness of 11.3 mm. Its effective focal length is 400 mm which will produce a 50x magnified image. The back focal length is 394.33 mm which we measured from the camera chip, and the lens was positioned at this theoretically optimal position.

Adjusting the correction collar The Nikon 25x objectives used for this setup have a built in correction ring that can be used to correct spherical aberrations resulting from refractive index differences when imaging samples behind a coverslip. This can be also effectively used to correct for any spherical aberrations occurring from imaging through the FEP foil. Although these aberrations are expected to be extremely low, due to the relatively thin, 50 μm foil thickness, and the close matching of refractive index ($n_{\text{FEP}} = 1.344$, $n_{\text{H}_2\text{O}} = 1.333$), for optimal, aberration free image quality it can't be neglected.

The correction collars are adjusted by inspecting a gel-suspended fluorescent bead

specimen with the microscope, where the beads can act as a reporter of the point spread function of the microscope. The alignment can be performed “live” by inspecting the bead image quality for aberrations. By gradually changing the correction collar, the ring artifacts are minimized on out-of-focus beads, and the peak intensity is maximized for in-focus beads. By moving the correction ring, the focal plane is also slightly shifted, which has to be compensated by shifting the light-sheet correspondingly to coincide with the correct imaging plane.

Adjusting the field of view To allow for proper sampling of the image, we use $50\times$ magnification, which combined with the $6.5\text{ }\mu\text{m}$ pixel pitch of our sCMOS camera, will result in a $0.13\text{ }\mu\text{m}$ pixel size. The full field of view recorded by the camera is $2048 \times 0.13\text{ }\mu\text{m} = 266.24\text{ }\mu\text{m}$. To ensure the best image quality, we align the center of the objective field of view on the camera sensor, since this region has the best optical properties in terms of numerical aperture, aberration correction and flatness of field.

Field of view alignment can be performed by using mirror M5 just before the detection merging unit. To identify the center region of the field of view, diffuse white light is used to illuminate the entire sample chamber, and it is imaged on the camera. Then, mirror M5 is adjusted until the top edge of the field of view becomes visible, *i.e.*, where the illumination from the chamber is clipped. This will have a circular shape. Afterwards, adjusting the mirror in the orthogonal direction, the left-right position of the field of view can be adjusted, by centering the visible arc on the camera sensor.

After the horizontal direction is centered, vertical centering is performed. This, however can not be centered the same way as the horizontal direction, since for that we would have to misalign the already aligned horizontal position. To determine the center, we move the field of view from the topmost position to the bottom. During this process the number of turns of the adjustment screw is counted (this can be done accurately by using a hex key). After reaching the far end of the field of view, the mirror movement is reversed, and the screw is turned halfway to reach the middle.

3.4 Control unit

The microscope’s control and automation is performed by an in-house designed modular microscope control system developed in LabVIEW [113]. The core of the system is a National Instruments cRIO-9068 embedded system that features an ARM Cortex A9 processor and a Xilinx Zynq 7020 FPGA. Having both chips in the same device is a great advantage, since the main processor can be used to run most of the microscope control software, while the FPGA can be used to generate the necessary output signals in real time and with high precision.

The embedded system is complemented by a high-performance workstation that is used to display the user interface of the microscope, and to record the images of the high-speed sCMOS camera.

3.4.1 Hardware

Various components need to be synchronized with high precision to operate the microscope: a laser combiner to illuminate the sample; a galvanometric scanner to generate the light-sheet; stages to move the samples; filter wheel to select the imaging wavelengths; and a camera to detect the fluorescence signal. For high speed image acquisition, all of these devices have to be precisely synchronized in the millisecond range, and some even in the microsecond range. Although they require different signals to control them, we can split them into three main categories:

digital input	analog input	serial communication
camera exposure	galvanometric position	filter wheel
laser on/off ($\times 3$)	laser intensity ($\times 3$)	stages ($\times 2$)

All devices are connected to the NI cRIO 9068 embedded system, either to the built in RS232 serial port, or to the digital and analog outputs implemented by C-series expansion modules (NI 9401, NI 9263, NI 9264). The workstation with the user interface is communicating with the embedded system through the network. The only device with a connection to both systems is the camera: the embedded system triggers the image acquisition, and the images are piped to the workstation through a dual CameraLink interface, capable of a sustained 800 MB/s data transfer rate (Figure 3.7).

3.4.2 Software

Being able to precisely control all of the instruments not only relies on the selected hardware, but just as much on the software. Our custom software is developed in LabVIEW, using an object-oriented approach with the Actor Framework. The embedded system is responsible for the low-level hardware control, for keeping track of the state of all devices, saving the user configurations, and automating and scheduling the experiments. It also offers a Javascript Object Notation (JSON) based application programming interface (API) through WebSocket communication. This is mainly used to communicate with the user interface, however it also offers the possibility of automated control by an external software.

FPGA software

The on-board FPGA is responsible for generating the digital and analog output signals based on the microscope settings (Figure 3.8). To avoid having to calculate all the traces

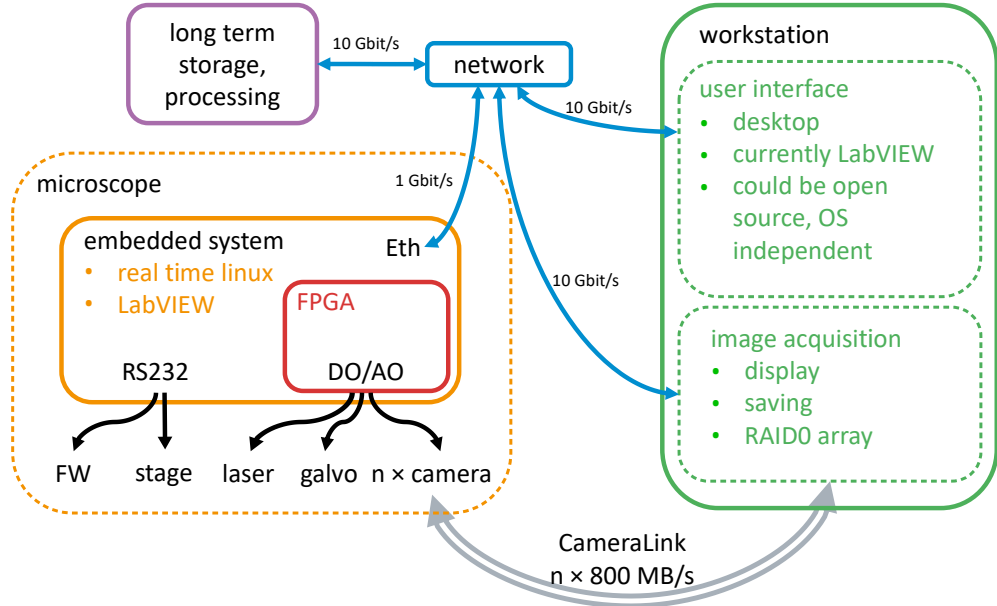


Figure 3.7: Microscope control hardware and software architecture. The embedded system responsible for the hardware control and the workstation are communicating through the network using the WebSocket protocol. The electronic devices of the microscope are either controlled through digital/analog signals, or through serial communication. The camera is also connected to the workstation with a CameraLink connection, which transmits the recorded images.

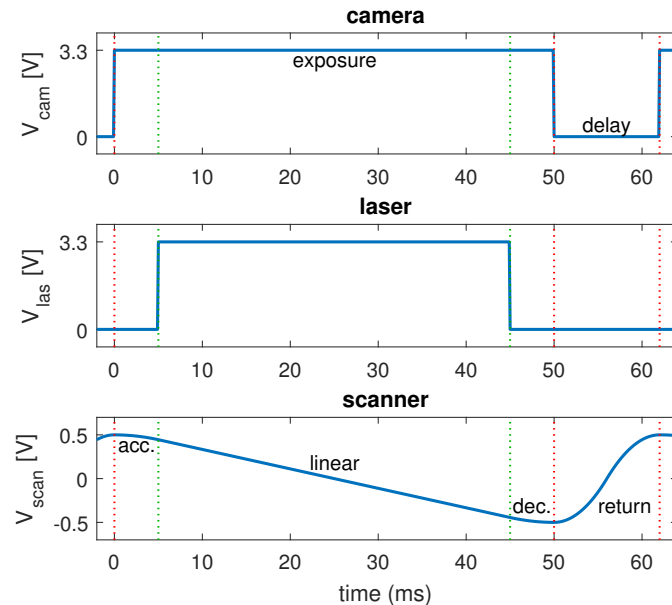


Figure 3.8: Digital and analog control signals. Example traces for recording a single plane with 50 ms exposure time and 12 ms delay. During the exposure of the camera the scanner has 3 sections: acceleration (acc.), linear, and deceleration (dec.). The laser line is synchronized with the scanner linear section to ensure even illumination.

for a whole stack, the main software only calculates a few key parameters of the traces that are necessary to completely describe them. The FPGA then calculates the signals in real time, and outputs them with microsecond precision.

To describe the traces, we define them as a concatenation of *sections*. Each section has 3 or 5 parameters, depending on whether they are digital or analog. Both types have three common properties: `value`, `length`, and `type`. The analog sections additionally contain a `dValue` and a `ddValue` element describing the velocity and the acceleration of the signal. This allows us to generate piecewise functions made of second-order polynomials.

The `type` element contains information on which value should be updated for the current section. Setting the lowest bit high will update the `value`, setting the second bit high will update the `dValue`, and setting the third bit high will update the `ddValue`. This feature allows to define smooth transitions between the sections, and also to define more complex signals, as long as they are periodic in the second derivative.

3.5 Results

Following the design phase, all custom parts were manufactured by the EMBL mechanical workshop, and the microscope was assembled on a MellesGriot optical table (Figure 3.9 and Figure D1). During the assembly and alignment of the microscope the author had assistance from Nils Wagner, Gustavo Quintas Glasner de Medeiros, and Yu Lin. The microscope was equipped with an Andor Zyla 4.2 sCMOS camera that offers a large field of view of 2048×2048 pixels with a pixel pitch of $6.5 \mu\text{m}$. It offers a high dynamic range of 1:30,000, and high frame rate at 100 frames per second (fps), while readout noise is minimal (0.9 e^-).

To evaluate the performance of the microscope, we conducted various measurements, concerning the stability and the resolution of the system. The methods and results of these measurements will be presented in this section.

3.5.1 Stability of the view switcher unit

As the view switcher unit is a custom-designed solution for this microscope, it is necessary to evaluate the effect of the switching on the field of view. Given that this is a moving unit, many mechanical imprecisions can introduce a drift in the final image.

To assess the reproducibility in the movement of the detection branch switching unit, a long-term stability test was conducted. To exclude all other factors (such as sample drift), we imaged the opening of two closed irises that were mounted on the detection optical rail. Image formation was done by two achromatic lenses ($f = 75 \text{ mm}$) positioned directly after mirrors M5 and M5'.

The apertures were imaged from both views every 10 seconds, for 4 h, for a total

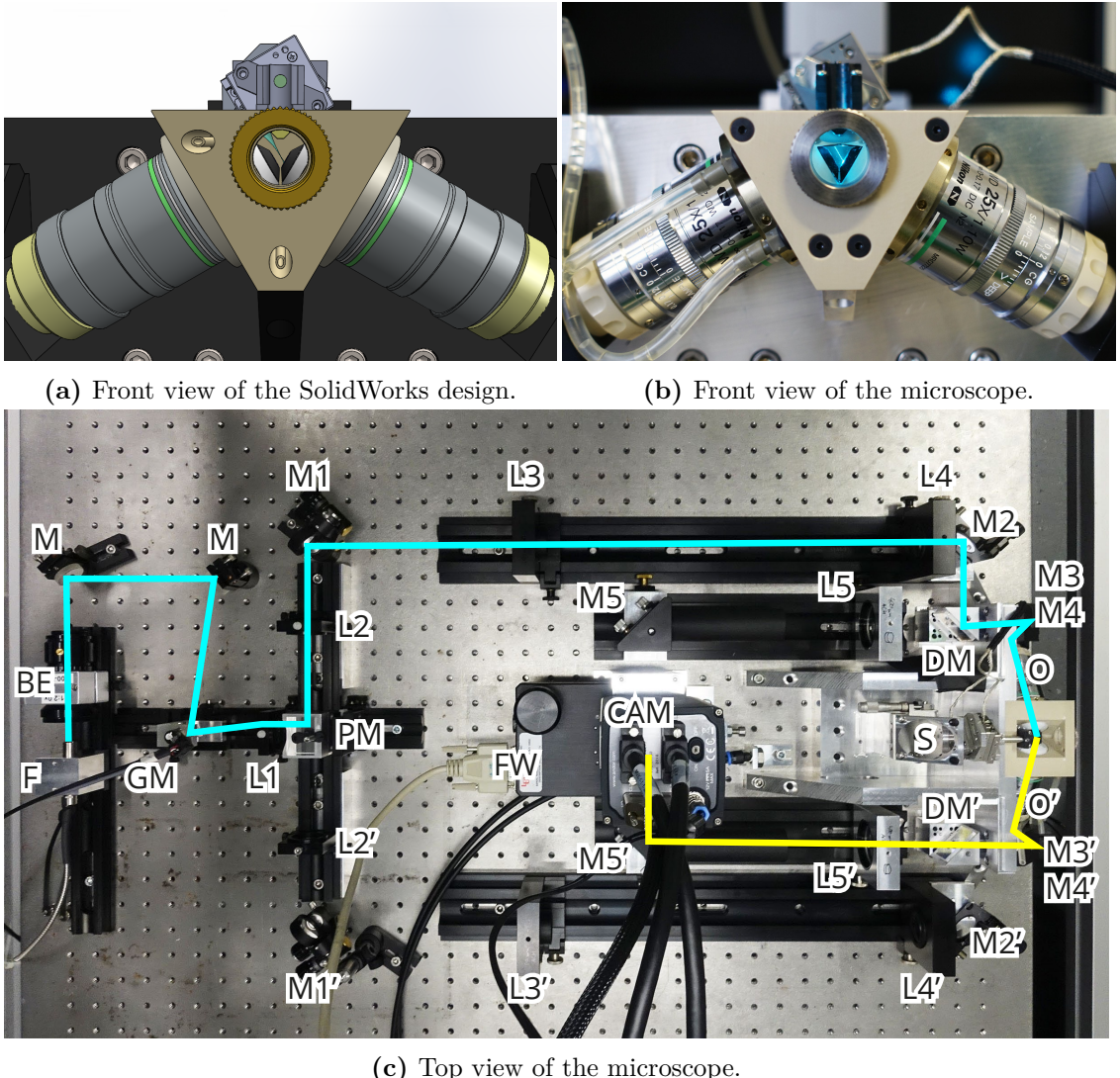


Figure 3.9: Completed DualMouse-SPIM. The excitation and emission light paths are depicted with blue and yellow lines respectively. Component numbering corresponds to Figure 3.3. Detection branch merging unit, and mirrors M6 and M6' are underneath the camera and filter wheel. BE – beam expander, CAM – camera, DM – dichroic mirror, F – fiber, FW – filter wheel, L – lens, M – mirror, O – objective, PM – prism mirror, S – stage

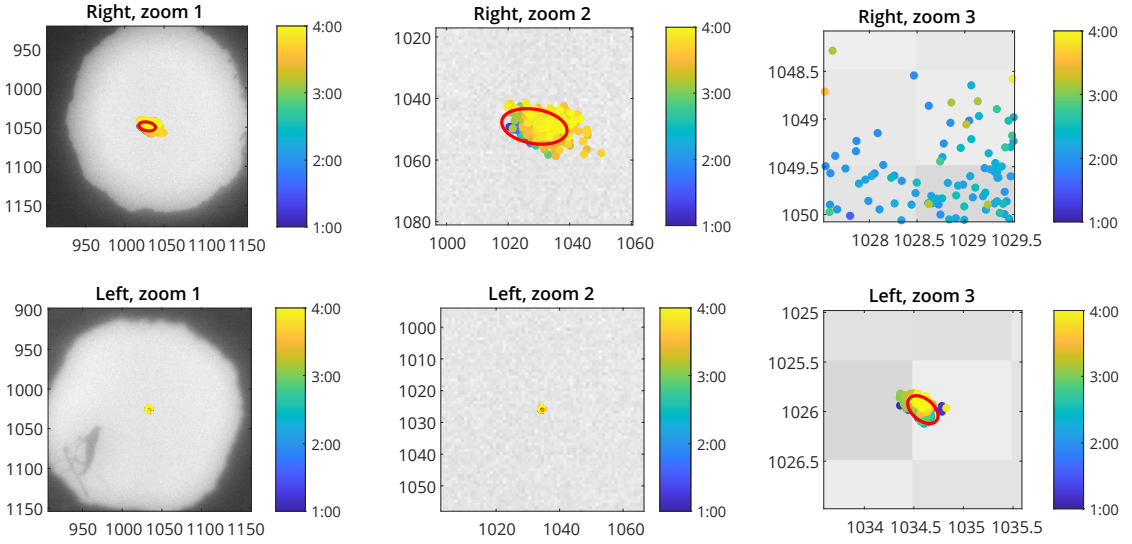


Figure 3.10: Stability measurements of view switcher unit. A closed aperture was imaged on the camera from both views, every 10s, for 4h. The dots represent the center of each frame, color coded with the time. The red ellipse represents the 95% confidence interval of the measured positions based on principal component analysis. Standard deviations for right view: $\sigma_1 = 4.37$ px, $\sigma_2 = 2.26$ px; for left view: $\sigma_1 = 0.07$ px, $\sigma_2 = 0.04$ px.

of 1440 images per view, and 2880 switches. The center of the aperture was segmented on all images using Matlab, and tracked to assess any drift occurring during the 4 h time lapse (Figure 3.10). To visualize the uncertainty of the aperture’s position, we performed principal component analysis (PCA) on the positions and visualized the results by plotting the 95% confidence ellipse on the images. Although the right view had a significant spread with a standard deviation of 4.37 px and 2.26 px along the long and short axes respectively, the left view was extremely stable, and the standard deviation was only 0.07 px and 0.04 px for the long and short axes respectively. This result implies that there is no conceptual limitation in reaching sub-pixel reproducibility with the view switching unit, although some optimization is still needed for the right view to reach the same stability as the left view.

3.5.2 Characterizing the illumination profile

Since a Gaussian beam is used for illumination, its intensity profile depends on the axial position (Equation 1.18). Although the total intensity at any cross section of the beam is constant, because of the divergent properties, the peak intensity varies. To assess any non-uniformities in the illumination pattern, we measured the illumination beam intensity for each view.

To visualize the beam, the chamber was filled with a fluorescent solution (0.1 % methylene blue in distilled water). In order to increase the signal-to-noise ratio of these images, a long exposure time of 200 ms was used, and 500 images of each beam were

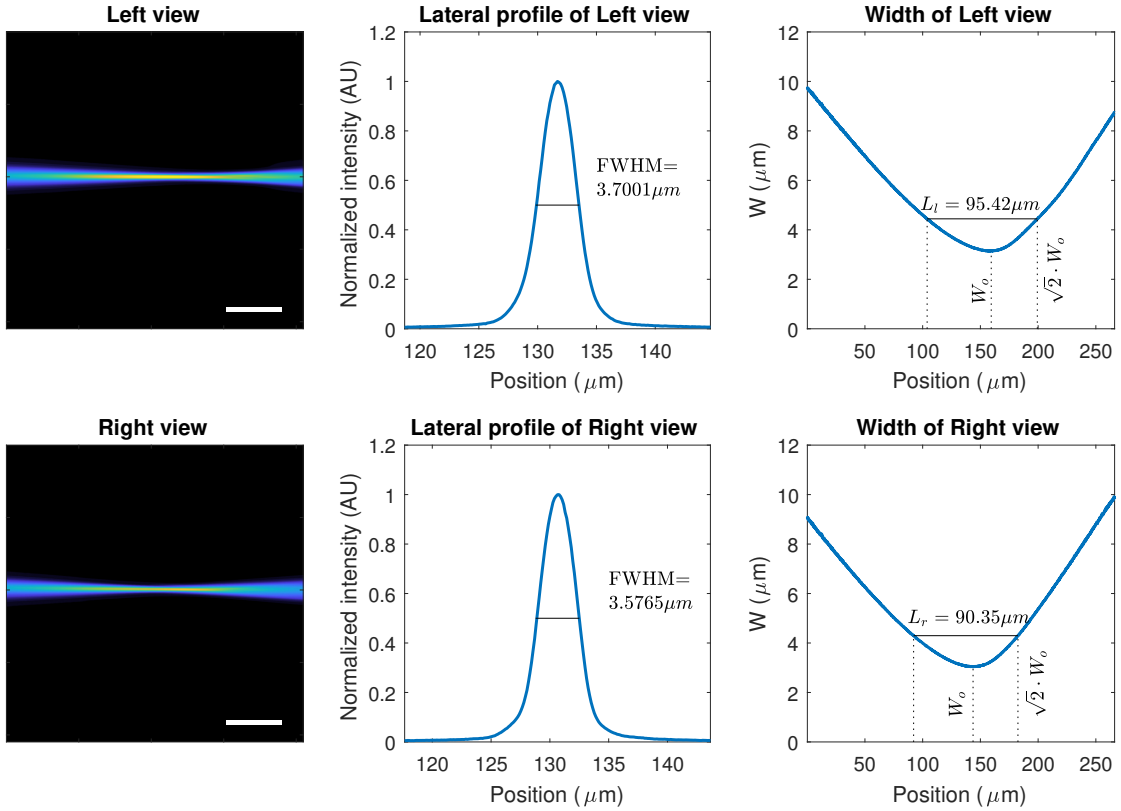


Figure 3.11: Illumination beam profile. Average of 500 stationary beam images for both left (top left) and right objectives (bottom left). Beam intensity profile along the waist of each beam is plotted in the center column. The right column shows the beam width profile of each beam ($1/e^2$).

averaged. Background images were acquired by repeating the image acquisition with the laser turned off. The average of the background images were subtracted from the averaged beam images, resulting in the beam intensity profile (Figure 3.11).

To determine the beam waist position we measured the beam thickness (FWHM) for each column of the averaged images, and located the position of the minimal width. The beam width at the waist position for the left view was $3.70\text{ }\mu\text{m}$, and for the right view it was $3.58\text{ }\mu\text{m}$ (Figure 3.11). We also measured the usable length of the beams (Section 1.3.1). The distance between the points where the beam has expanded by a factor of $\sqrt{2}$ relative to the waist is $95.42\text{ }\mu\text{m}$ for the left view, and $90.35\text{ }\mu\text{m}$ for the right view. This corresponds well to the original requirement of a minimal field of view of $100\text{ }\mu\text{m}$. Depending on the sample and the required level of optical sectioning, the practical field of view can be larger than this if the light-sheet is adjusted, as the camera sensor allows for a field of view of $266\text{ }\mu\text{m}$.

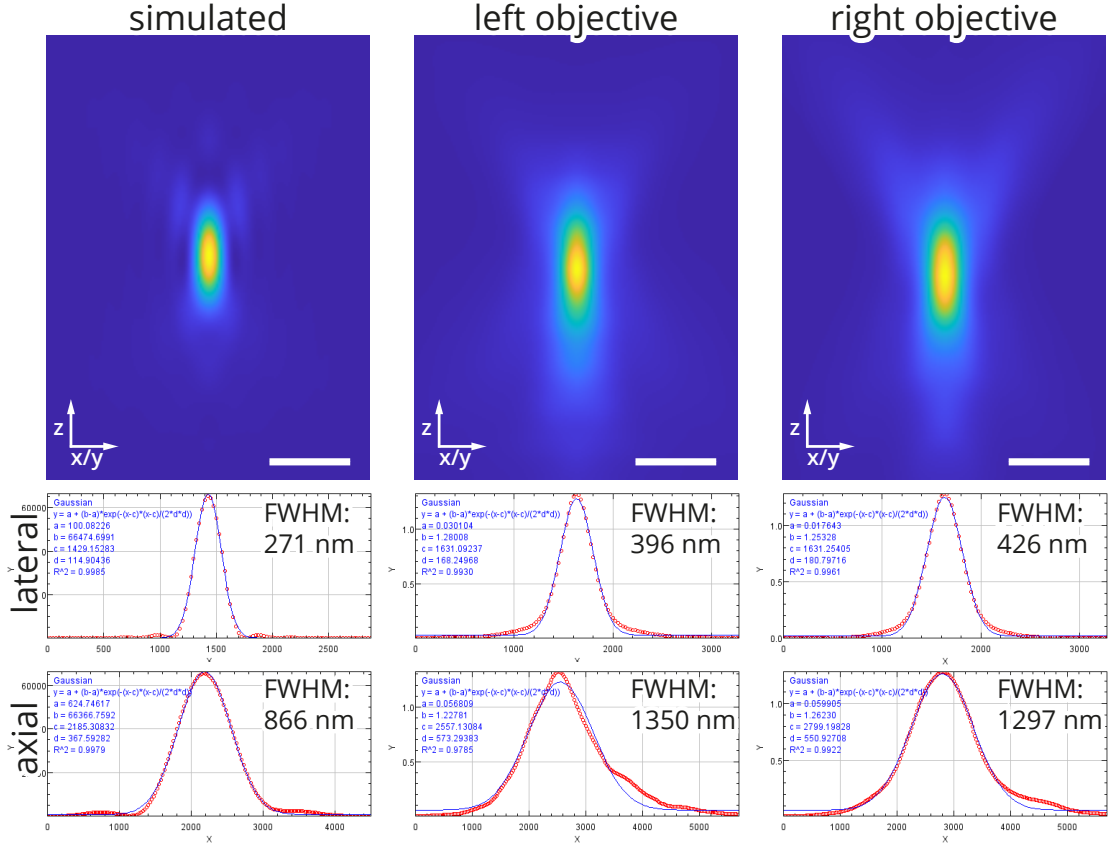


Figure 3.12: Simulated and measured PSF of Dual Mouse-SPIM. Top row: axial sections of simulated and measured point spread functions. Middle row: lateral intensity profile and Gaussian fit. Bottom row: Axial intensity profile and Gaussian fit. Simulations were performed based on the Gibson-Lanni model. Immersion medium and sample refractive index: 1.330, coverslip (FEP foil) refractive index: 1.344, coverslip distance: 1900 μm , coverslip thickness: 50 μm . Excitation wavelength: $\lambda_{ex} = 561 \text{ nm}$. Emission wavelength: $\lambda_{em} = 600 \text{ nm}$. Scale bar: 1 μm .

3.5.3 Resolution and point spread function measurement

In order to establish an ideal, reference PSF, we simulated the theoretical PSF of the microscope with the Gibson-Lanni model [114], using the MicroscPSF Matlab implementation [115]. The advantage of this model is that it accounts for any differences between the experimental conditions and the design parameters of the objective, and thus it can simulate any possible aberrations that may arise. The adjustable parameters are the thicknesses (t) and refractive indices (n) of the immersion medium (i), coverslip (g), and sample (s). To simulate the reference PSF, we accounted for the slight mismatch in refractive index between the FEP foil ($n_g = 1.344$) and water ($n_i = 1.33$). The working distance of the objective is 2 mm, while the thickness of the foil is 12.5 μm .

It is apparent from the simulations that even though the FEP refractive index is almost identical to the refractive index of water, a slight spherical aberration is still present even for the ideal case (Figure 3.12, left). The resolution measured as the FWHM of the

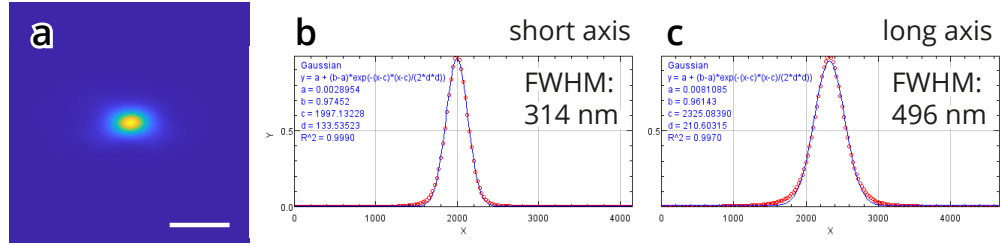


Figure 3.13: Combined PSF of 2 views. (a) The measured PSFs (Figure 3.12) were rotated to their corresponding orientations and multiplied. (b) Gaussian fit along the short axis of the combined PSF; FWHM=314 nm. (c) Gaussian fit along the long axis of the combined PSF; FWHM=496 nm. Scale bar, 1 μm

intensity profile through the lateral and axial cross sections is 271 nm and 866 nm respectively. The FWHM was measured in Fiji by fitting a Gaussian curve, and multiplying the standard deviation of the resulting fit by $2\sqrt{2 \ln 2}$.

To experimentally determine the resolution of the microscope and characterize its optical performance, we measured the point spread function using fluorescently labeled beads suspended in 0.8% GelRite (Section 3.6). The gel was loaded in glass capillaries and allowed to cool. After the gel solidified, a ~ 1 mm piece was cut off and placed in the microscope sample holder. The beads were imaged from both views using the 561 nm laser line with the 561 long-pass filter (Semrock, BLP02-561R-25).

From both views 12 beads were averaged using Fiji [116] and the 3D PSF estimator of the MOSAIC suite [117]. In order to acquire a more accurate PSF, the averaged bead images were deconvolved with the ideal image of the bead (uniform sphere with a diameter of 500 nm) using the DeconvolutionLab2 Fiji plugin [118]. The results of the deconvolution are shown on Figure 3.12. Similarly to the simulation, we measured the axial and lateral resolutions on the experimental PSFs. For the left view, the measured resolutions were 396 nm in the lateral direction, and 1350 nm in the axial direction. For the right view the lateral resolution was 426 nm, and the axial was 1297 nm.

To estimate the achievable multi-view resolution of the system, we combined the two measured PSFs. First, the PSFs were rotated by $\pm 60^\circ$ to correspond to the objective orientations. The PSF images were then normalized by scaling the maximum to 1, and the two rotated and normalized PSFs were multiplied (Figure 3.13). Resolution of the combined PSF is much improved in all directions: along its shortest axis the FWHM is 314 nm, and along the longest axis the FWHM is 496 nm (Figure 3.13). Both are better than the corresponding resolutions for a single view, especially along the long axis, where the FWHM is 2.67 times smaller. This is almost perfectly matching the theoretically expected increase in the axial direction (compare with Section 3.1).

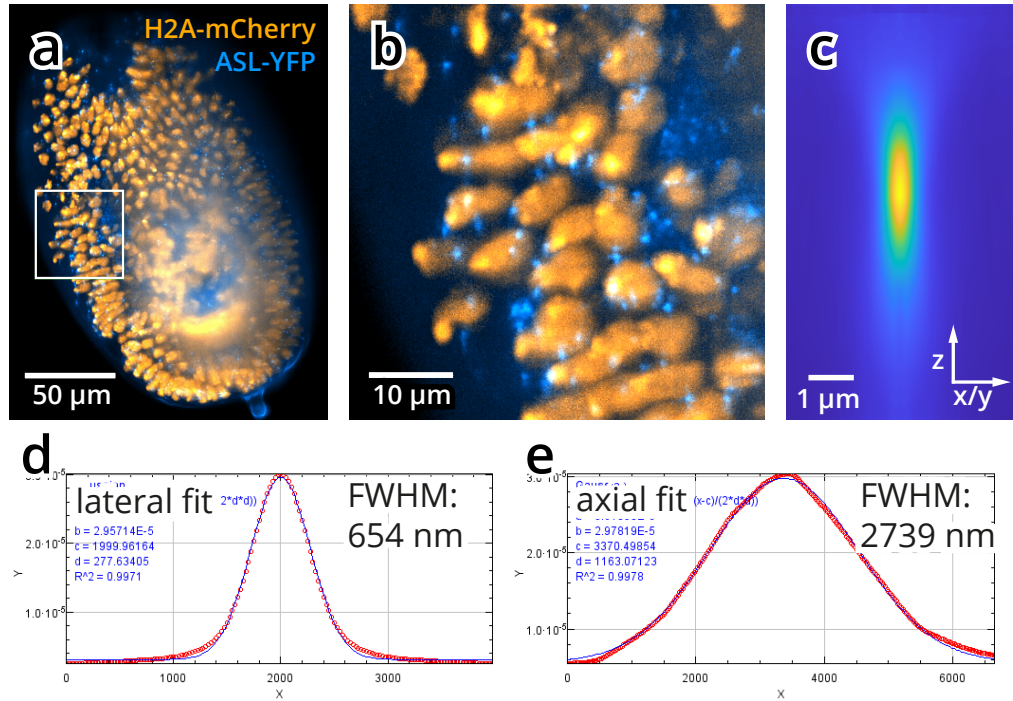


Figure 3.14: Maximum intensity projection of a *Drosophila melanogaster* embryo recording. Maximum intensity projection of a 30 μm thick substack. Orange: nuclei (H2A-mCherry), blue: centrioles (ASL-YFP). 50x magnification. (a) Overview of the embryo. (b) Zoomed in view to the region marked in (a). (c) Average image of 15 centrioles distributed evenly in the embryo. (d) Gaussian fit on the lateral intensity profile of the averaged centrioles; FWHM=654 nm. (e) Gaussian fit on the axial intensity profile of the averaged centrioles; FWHM=2739 nm.

3.5.4 Resolution inside a *Drosophila melanogaster* embryo

Apart from measuring the point spread function and resolution in an ideal bead sample, we also wanted to know the resolution inside a biological sample, as the tissues usually introduce some aberrations to the light path. Although these aberrations highly depend on the sample, as a worst case scenario, we measured the point spread function inside a *Drosophila melanogaster* embryo. As this specimen is highly opaque and scattering, it gives a good estimate for the upper bound of the resolution.

Instead of the fluorescent beads, we imaged a *Drosophila* embryo expressing H2A-mCherry marking the nuclei, and ASL-YFP marking the centrosomes (Figure 3.14a, and Section 3.6). As the centrosomal protein ASL is diffraction limited in size [119], its image gives a good estimate for the point spread function inside the specimen.

Similarly to the bead recordings, 15 centriole images were averaged with the 3D PSF tool of the MOSAIC plugin in Fiji (Figure 3.14c). On the averaged image we measured the resolution by fitting a Gaussian function on the lateral and axial intensity profiles (Figure 3.14d,e), and calculating the FWHM of the fitted Gaussian. The size of the averaged centrioles was 654 nm in the lateral, and 2739 nm in the axial direction.

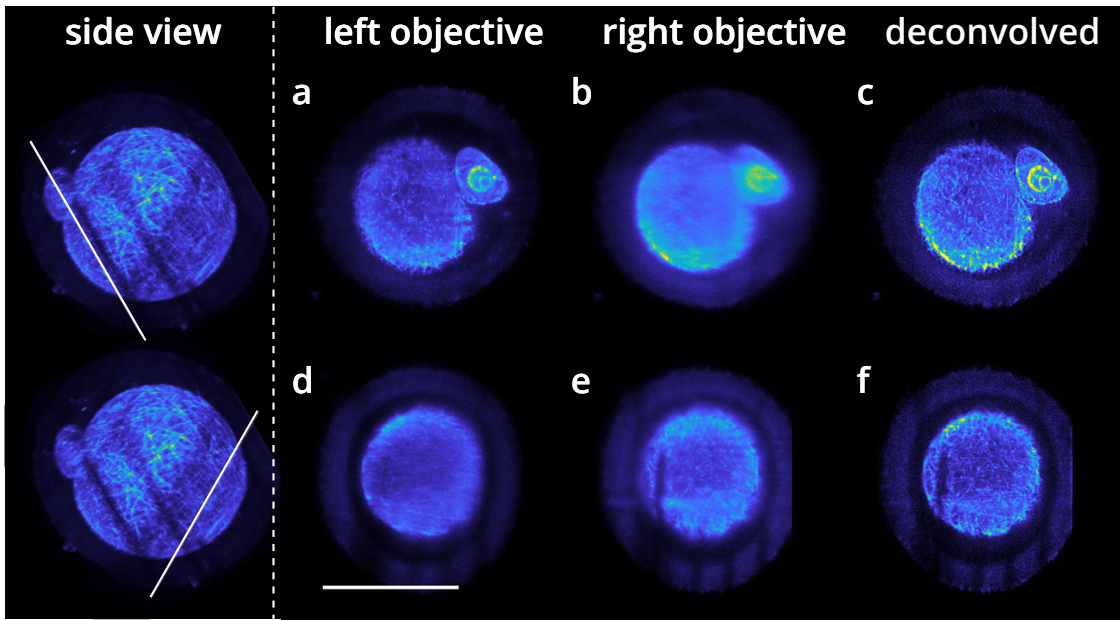


Figure 3.15: Multi-view recording of a mouse zygote. Dual-view imaging was performed on a fixed mouse zygote. Microtubules were stained with Alexa Fluor 488 coupled secondary antibodies. Top row: view of Left objective. Bottom row: view of Right objective. (a) Raw image from left objective. (b) Rotated view of Right objective. (c) Multi-view deconvolution of stacks (a) and (b). (d) Rotated slice from left objective. (e) Raw image from right objective. (f) Multi-view deconvolution of stacks (d) and (e). Scale bar: 50 µm. The darker banding artifacts visible on the side view are due to bleaching.

3.5.5 Multi-view imaging of a mouse zygote

To demonstrate the multi-view capabilities and improved image quality of the microscope, we performed dual-view imaging of a fixed mouse zygote and combined the images using the Multiview Reconstruction [112] plugin of Fiji (Figure 3.15). The microtubules were stained with Alexa Fluor 488 coupled secondary antibodies, and the zygote was imaged from both views with 0.5 µm inter-plane distance.

Anisotropy in the resolution becomes apparent in the single-view recordings, when the stacks are resliced from a different direction than the imaging plane. Even though the native view of each objective (Figure 3.15a,d) shows good contrast and easy to recognize features, when rotated and sliced corresponding to the view of the other objective, the contrast is almost completely gone, and the resolution is decreased (Figure 3.15b,e). The fused stack, after the multi-view deconvolution contains the high resolution information from both views, and thus both directions show good quality and high contrast (Figure 3.15c,f).

3.6 Methods

3.6.1 Preparation of fluorescent bead samples

For registration and resolution measurements we used TetraSpeck 0.5 µm diameter fluorescently labeled beads (ThermoFisher, T7281). The stock bead solution was thoroughly vortexed and sonicated for 5 min before diluting it 1:100 in distilled water. The diluted bead solution was stored at 4 °C until use. GelRite (Sigma-Aldrich, G1910) gel was prepared in distilled water at 0.8% concentration with 0.1% MgSO₄ · 7H₂O and kept at 70 °C until use. 50 µl of the diluted bead solution was added with a heated pipette tip to 450 µl of gel solution at 70° to prevent polymerization. The gel was thoroughly vortexed, and loaded to glass micropipettes (Brand 100 µl). The gel was allowed to cool to room temperature and stored in a petri dish under dH₂O at 4 °C until use. For imaging a small piece of gel was extruded from the capillary, cut off, and placed in the sample holder. After positioning the gel to the bottom of the sample holder, the holder was filled with 200 µl dH₂O.

3.6.2 Preparing the sample holder

The sample holder was lined with 12.5 µm (PSF measurements) or 50 µm (mouse zygote and *Drosophila* embryo imaging) thin FEP foil (Lohmann, RD-FEP050A-610). The FEP foils were cut to size, washed with 70% ethanol followed by a second wash with dH₂O. After washing, both surfaces of the foils were chemically activated by a 20 s plasma treatment (PlasmaPrep2, Gala Instrumente). The foils were then stored in a petri dish until further use, separated by lens cleaning tissues (Whatman, 2105-841). Before imaging, the sample holder was cleaned with dish soap, rinsed with tap water, rinsed with 70% ethanol, and rinsed with dH₂O. The prepared foils were glued to the inside of the cleaned sample holder with medical grade silicon glue (twinsil speed, picodent). During the 5 min curing process the foil was pressed against the sample holder by a custom made press fitting the shape of the sample holder. Final dilution of the stock bead solution in the gel is 1:1000.

3.6.3 Drosophila embryo imaging

Drosophila melanogaster embryos (fly stock AH1) expressing fluorescent nuclear (H2A-mCherry) and centriole (ASL-YFP) markers were collected on apple juice agar plates and dechorionated in 50% bleach solution for 1 min. After rinsing the bleach with deionized water, the embryos were placed in the sample holder under PBS solution. A small piece of gel containing fluorescent beads were also placed next to the samples to aid in multi-view registration.

3.6.4 Mouse zygote imaging

Fixed mouse zygotes labeled with Alexa Fluor 488 (microtubules) and Alexa Fluor 647 (kinetochores) coupled secondary antibodies were kindly provided by Judith Reichmann. Zygotes were transferred to the sample holder, and imaged in PBS. To allow for multi-view reconstruction, a small piece of gel containing fluorescent beads was placed next to the zygote in the sample holder. After imaging the zygote from both views, the beads were also recorded using the same stack definitions. After data acquisition, the multi-view datasets were registered and deconvolved in Fiji [116] using the Multiview Reconstruction Plugin [112, 120]. The deconvolution was based on a simulated PSF generated in Fiji with the PSF Generator plugin [121] using the Born-Wolf PSF model [24]. $NA_{ex} = 0.1$, $NA_{em} = 1.1$, $n=1.33$, $\lambda_{ex} = 488 \text{ nm}$, $\lambda_{em} = 510 \text{ nm}$.

3.7 Discussion

In this chapter we have presented a novel light-sheet microscope designed for subcellular imaging of mouse embryos. The microscope has two identical objectives, positioned in a 120° angle, and operates with a 30° tilted light-sheet. Due to the symmetrical design both objectives can be used for detection and illumination as well, providing multi-view capabilities without sample rotation. The 120° objective configuration allows the use of high numerical aperture objectives (1.1 instead of 0.8), which drastically increases the light collection efficiency compared to the conventional 90° configuration. Due to this improvement the microscope requires less tradeoff in imaging speed, resolution, contrast, and phototoxicity, as the corners of the pyramid (Figure 1.1) are now moved closer together.

We have characterized the optical properties of the microscope by measuring the light-sheet dimensions (average length: $93 \mu\text{m}$, average thickness: $3.6 \mu\text{m}$), and by measuring the point spread function. When combining the two views, the resolution is much closer to an ideal isotropic shape, being 496 nm along the long axis and 314 nm along the short axis as opposed to 1323 nm and 411 nm measured for a single view. This 2.67 fold increase in axial resolution can potentially make the difference in being able to track all chromosomes in a developing mouse embryo.

The obtained resolution is comparable to the state of the art lattice light-sheet microscopy (LLSM) [7] (230 nm lateral and 370 nm axial), however, the optical alignment and the operation of our microscope is considerably simpler, as there is no need for the use of a spatial light modulator. As LLSM relies on the self-interference of the illumination beam to obtain the thin sectioning pattern, the practical imaging volume is only $50 \times 50 \times 50 \mu\text{m}^3$. In contrast, the Dual Mouse-SPIM is capable of imaging a volume of $260 \times 100 \times 100 \mu\text{m}^3$ due to the more robust Gaussian-beam illumination and the

two-sided detection. Imaging very fast dynamics from two directions, however, might be challenging, as the detection direction is switched with a mechanical part, which limits the maximum volumetric imaging speed.

To be able to surpass the proof-of-concept state, the microscope still needs some improvements. The detection view switching unit needs to be improved to minimize field of view drift of both views. One possible issue with the current solution is the insufficient damping of the moving mirror unit, which can cause unwanted vibrations when the switching force is high. This can also be a possible explanation of why only one direction was unstable, as the movement speed was not equal in both directions. Since the pneumatic cylinder has a single actuator rod, the force on the piston is different depending on the movement direction: on the side where the rod is attached to the piston the surface area is smaller, thus the actuating force is lower with the same air pressure. This could be remedied by applying a more efficient damping system, and by making sure that the forces are the same in both directions. For small specimens, if a reduced field of view is sufficient, the entire moving assembly can be replaced by a fixed prism mirror, which reflects the two objective images on either half of the camera sensor. This has the added benefit of faster imaging, since the switching time between the two imaging branches is only limited by the galvanometric scanner. Another solution could be the addition of a second camera, which would make the view switching completely unnecessary without sacrificing the field of view.

Another necessity for long-term experiments is the implementation of an environmental chamber to provide the appropriate conditions for live mammalian embryo imaging. This involves the integration of a heating element and a gas mixer unit to the mechanical design, complemented by an enclosure that seals off the environment of the imaging chamber. The mechanical design is already underway and the electronic control will be integrated with the modular control software.

The use of high-NA objectives also keeps the door open for future upgrades, such as the addition of structured illumination [55, 56], or coupling in a high-power pulsed laser for photomanipulation capabilities [122]. Another natural extension to the system would be the addition of a third objective that would allow for truly isotropic imaging and two-sided sample illumination. Using three objectives would introduce some challenges in sample mounting, as the open-top sample holder design could not be used in the same way. A more practical way would be the use of an FEP tube, where the embryos could develop in the appropriate medium while they are sealed from the outside by gel plugs on either side. Of course such a system will need to be thoroughly tested of live imaging compatibility.

Single-view solutions for isotropic imaging only allow a very limited field of view. For diffraction-limited optical sectioning a Gaussian beam is diverging too fast [123], while

3.7 Discussion

the use of other, non-diffractive beams rely on self-interference [7], which breaks down after a few tens of micrometers inside the sample. Our dual-view high NA solution allows for near isotropic resolution even for large fields of view, such as for entire mouse zygotes or embryos ($120\text{ }\mu\text{m} \times 120\text{ }\mu\text{m} \times 120\text{ }\mu\text{m}$).

Chapter 4

GPU-accelerated image processing and compression

4.1 Challenges in data handling for light-sheet microscopy

When using any kind of microscopy in research, image processing is a crucial part of the workflow. This is especially true for light-sheet microscopy, since it is capable of imaging the same specimen for multiple days, producing immense amounts of data. A single overnight experiment of *Drosophila* development (which is a very typical use-case for light-sheet microscopy) can produce multiple terabytes of data.

Apart from light-sheet microscopy, many other microscopy modalities also suffer from this problem. Methods, such as high content screening [124–126] and single molecule localization microscopy (SMLM) [127–129] can easily face similar challenges.

Not only these methods are capable of generating data extremely fast, but with the sustained high data rate a single experiment can easily reach multiples of terabytes (Figure 4.1). Handling this amount of data can quickly become the bottleneck for many discoveries, which is a more and more common issue in biological research [130–132].

This chapter will focus on addressing these challenges by presenting a real-time, GPU-based image preprocessing pipeline developed in CUDA [133] consisting of two parts (Figure 4.2). The first part is a fast image fusion method for our workhorse light-sheet microscope, the MuVi-SPIM [45], that enables live fusion of the images arriving from two opposing cameras. The second part of the pipeline, which can also be used in a standalone way, is a real-time image compression library that allows for lossless and noise-dependent lossy compression of the data directly during acquisition even for high-speed sCMOS cameras.

4.2 Real-time preprocessing pipeline

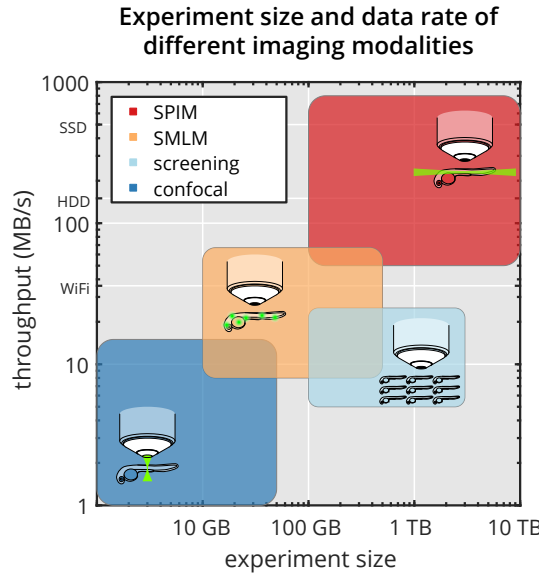


Figure 4.1: Experiment sizes and data rate of different imaging modalities. Comparison of single-plane illumination microscopy (SPIM, red), high-content screening (light blue), single molecule localization microscopy (SMLM, orange) and confocal microscopy (blue) by typical experiment size and data production rate (see also Table B1 in Appendix B).

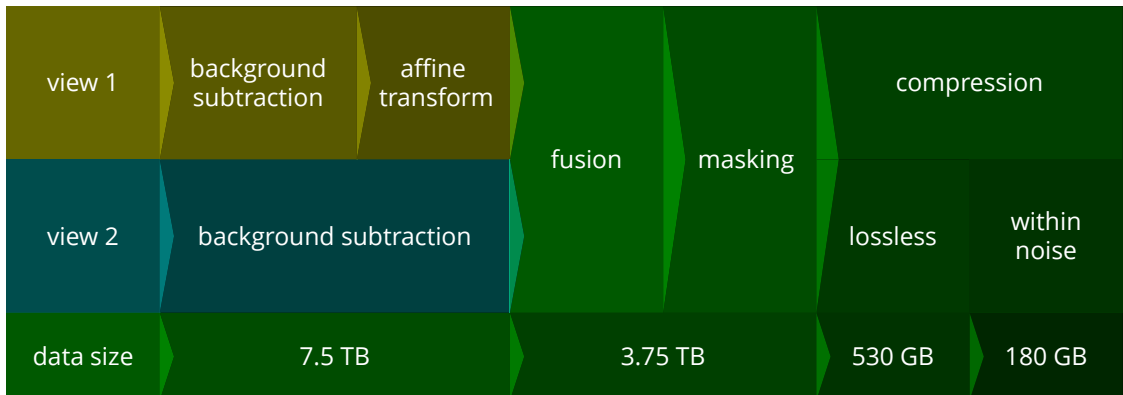


Figure 4.2: Real-time image processing pipeline for multiview light-sheet microscopy.

4.2 Real-time preprocessing pipeline

Similarly to the DualMouse-SPIM, our currently used production microscope, the Multiview-SPIM (MuVi-SPIM) [45] also uses multiple imaging directions to improve the image quality. In this case, however, the aim is completeness rather than increasing the resolution. As the MuVi-SPIM is capable of imaging much larger specimens, such as entire *Drosophila* embryos, the sample size itself can present some challenges, especially for opaque specimens. As light scattering and absorption impact both the illumination and detection optics, the negative effects for SPIM are more pronounced compared to single-lens systems [134].

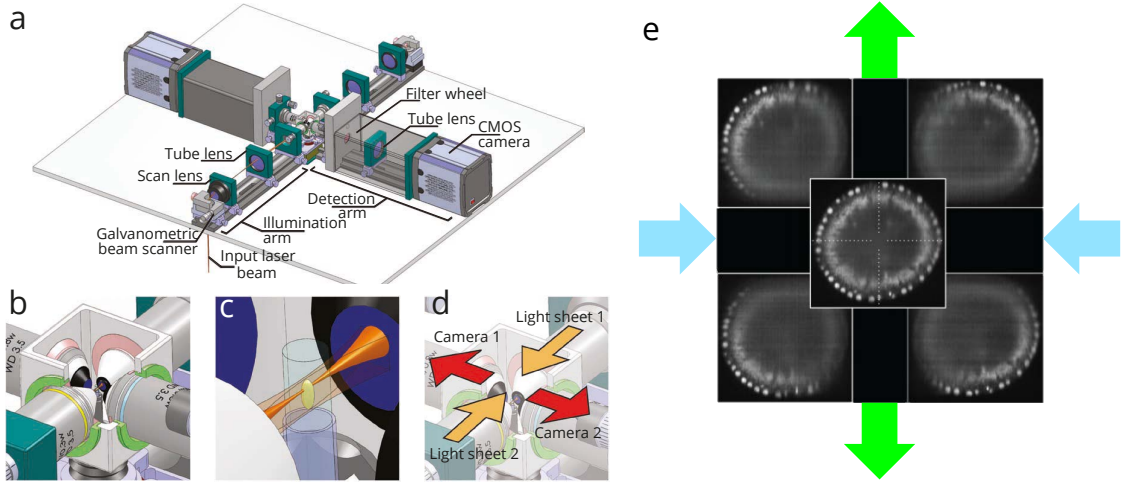


Figure 4.3: Operating principle of MuVi-SPIM. (a) The microscope consists of two illumination and two detection arms for simultaneous multiview illumination and detection. (b) The 4 arms meet in the imaging chamber that is filled with water, and contains the sample. (c) The sample is held by a glass capillary, in a GelRite cylinder. Optical sectioning is achieved by a virtual light-sheet. (d) The light-sheets can be generated from two sides (light-sheet 1 and 2), and detection is also double sided (Camera 1 and 2). Adapted from [45].

4.2.1 Multiview SPIM for *in toto* imaging

MuVi-SPIM provides an elegant solution for multiview imaging. A standard SPIM setup with a single detection and a single illumination lens would rotate the sample to acquire images from multiple directions. MuVi-SPIM, on the other hand, utilizes two opposing objectives for illumination and two opposing objectives for detection (Figure 4.3a). As the sample is held by an aqueous gel inside the imaging chamber, all objectives have unobstructed view of it from multiple directions (Figure 4.3b,c).

Data acquisition is done in two steps: the sample is illuminated by light-sheet 1, and fluorescence is collected by both detection objectives at the same time. After this, light-sheet 2 is activated and both cameras record the fluorescence again (Figure 4.3d). This process will result in 4 datasets, all with partial information due to scattering effects. The 4 views are later fused to a single, high quality dataset (Figure 4.3e). This fusion process is necessary before any further analysis steps can be performed. However, due to the sheer size of the data, it takes a considerable amount of time after the acquisition.

By combining scanned light-sheet [49] with confocal slit detection on the camera chip [135], it is possible to exclude out-of-focus, scattered illumination light. This way it is possible to illuminate simultaneously with both light-sheets, which leaves us with only two views, the views of the two opposing cameras [75].

4.2.2 Image registration

To perform image fusion of multiple views, first image registration is necessary: the coordinate systems of the views have to be properly overlapped. Ideally a single mirroring transformation would be enough to superpose the two camera images, however, in practice the microscope can never be aligned with such precision. Other types of transformations are also necessary: translation to account for offsets in the field of view; scaling in case of slightly different magnifications; and also shearing if the detection plane is not perfectly perpendicular to the sample movement direction [136]. To combine all of these effects, a full, 3D affine transformation is necessary to properly align the two camera images (Figure 4.4 a). This transformation can be represented by a matrix multiplication with 12 different parameters:

$$\begin{pmatrix} x' \\ y' \\ z' \\ 1 \end{pmatrix} = \begin{pmatrix} a & b & c & d \\ e & f & g & h \\ i & j & k & l \\ 0 & 0 & 0 & 1 \end{pmatrix} \times \begin{pmatrix} x \\ y \\ z \\ 1 \end{pmatrix} = \begin{pmatrix} ax + by + cz + d \\ ex + fy + gz + h \\ ix + jy + kz + l \\ 1 \end{pmatrix}$$

where x, y, z are the coordinates in the original 3D image, x', y', z' are coordinates in the transformed image, and a, b, \dots, l are the affine transformation parameters.

These parameters are traditionally acquired by a bead based registration algorithm after imaging fluorescent beads from each view of the microscope [120, 137]. The beads are segmented by using a difference of Gaussian filter, and the registration parameters are acquired by matching the segmented bead coordinates in each view. Identifying the corresponding beads is done by a translation and rotation invariant local geometric descriptor. This matches the beads based on their relative position to their nearest neighbors. After the matching beads are identified, the affine transformation parameters are calculated by minimizing the global displacement for each pair of beads.

For the two opposing views of MuVi-SPIM, these parameters are only dependent on the optical setup itself, and not on the sample or on the experiment. Because of this, it is sufficient to determine the transformation parameters only after modifying the microscope (*e.g.*, after realignment).

In our currently used fusion pipeline, after the parameters are acquired, the 3D stacks are fused by transforming one of the views to the coordinate system of the other (using the affine transformation parameters from the bead based registration), and fusing the two stack by applying a sigmoidal weighted average (4.4a). The weights are determined in a way to exclude the parts of the stacks that have worse image quality and complement these from the other view's high quality regions. When using the electronic confocal slit detection (eCSD) weighting is not necessary, as the scattered light is already rejected in these recordings, and a simple sum of the two stacks gives the best result regardless of

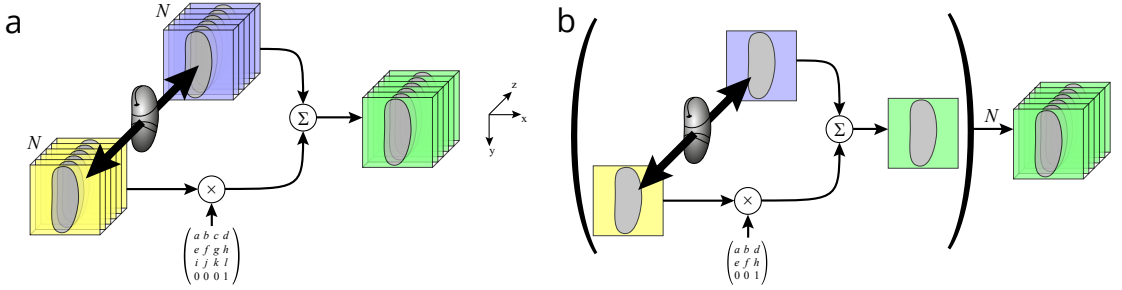


Figure 4.4: multiview fusion methods for light-sheet microscopy. a) Full 3D stacks are acquired from the opposing views (yellow and blue), which are then registered in 3D space using previously acquired affine transformation parameters. Registered stacks are then weighted averaged to create the final fused stack (green). b) Images from opposing views are directly fused plane by plane. Registration takes place in 2D space thus reducing computational effort and memory requirements. The registered planes are then weighted averaged to create the final fused image.

the sample [75].

The fusion process itself can be very resource intensive and can take a considerable amount of time. This is simply due to the size of the 3D stacks: a single dataset is usually between 2 and 4 GB in size. Thus, the necessary memory requirement to fuse 2 of these stacks is $3 \cdot 4 \text{ GB} = 12 \text{ GB}$, as the result will also take up the same space. Just reading and writing this amount of information to the hard disk takes a substantial amount of time. When using an SSD drive for example, with a 500 MB/s read and write speed, just the read/write operations will take around $\frac{12 \text{ GB}}{500 \text{ MB/s}} = 24 \text{ s}$.

4.2.3 2D fusion of opposing views

To speed up the image processing, we take a new approach to fusing the images. As the two objectives of MuVi-SPIM ideally image the same z plane, it should be possible to reduce the alignment problem to a 2D affine transformation:

$$\begin{pmatrix} x' \\ y' \\ 1 \end{pmatrix} = \begin{pmatrix} a & b & d \\ e & f & h \\ 0 & 0 & 1 \end{pmatrix} \times \begin{pmatrix} x \\ y \\ 1 \end{pmatrix} = \begin{pmatrix} ax + by + d \\ ex + fy + h \\ 1 \end{pmatrix}$$

The advantage of a simplified transformation is not only the reduced computational complexity, but also the massively reduced memory requirement, as in this case it is sufficient to store 3 planes in memory instead of 3 entire stacks (Figure 4.4 b). Performing the 2D direct fusion on the GPU immediately after acquisition has two benefits: first, only the fused images are stored on the hard drive, which directly results in 50% savings in storage space. Second, since the fusion is faster than the camera acquisition speed, the fused image can be displayed for the users instead of the 2 raw images. This would greatly improve user experience and speed up the initial set-up phase of each experiment.

In order to allow for the direct 2D fusion, the microscope needs to be very well aligned

4.2 Real-time preprocessing pipeline

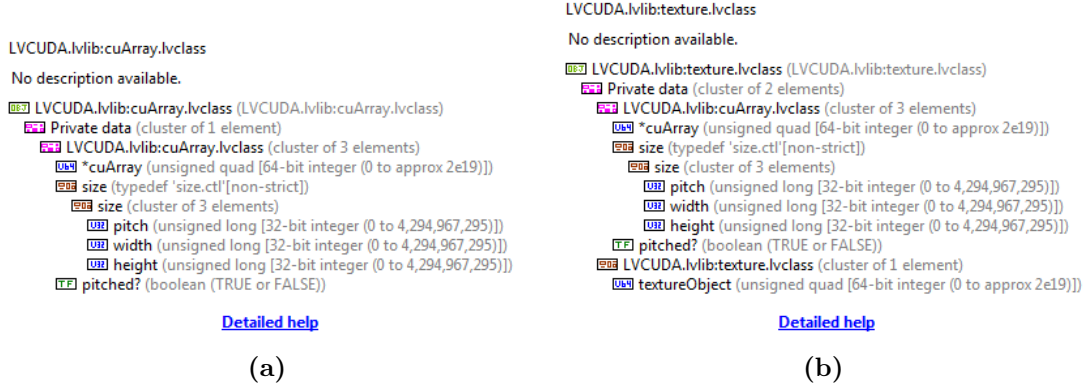


Figure 4.5: Classes of LVCUDA library. (a) **CuArray** class, wrapping a 1D or 2D pitched device memory for use in LabVIEW. (b) **Texture** class, wrapping a CUDA texture object for use in LabVIEW.

to minimize any adverse effects arising from discarding some of the transformation parameters. The requirements for this are the following:

$$|cz| < \sigma_{xy} \quad \forall z \quad (4.1)$$

$$|gz| < \sigma_{xy} \quad \forall z \quad (4.2)$$

$$|ix + jy + (k - 1)z + l| < \sigma_z \quad \forall x, y, z \quad (4.3)$$

where σ_{xy} is the lateral resolution, and σ_z is the axial resolution of the microscope, which are 277 nm and 1099 nm respectively.

If these conditions are fulfilled (*i.e.*, the microscope is properly aligned), direct plane by plane fusion will not result in any loss of information compared to the full 3D image fusion.

4.2.4 CUDA implementation of direct fusion

Our custom microscope control software (Section 3.4.2) is developed in LabVIEW, and we implemented the pipeline as a combination of a CUDA and a LabVIEW library. The CUDA library implements all the necessary low level functions and exposes these in a dynamically linked library (dll). The LabVIEW library, **LVCUDA.lvlib** implements two high level classes: **CuArray** and **Texture** (Figure 4.5). These classes interface with the CUDA dll, and allow to easily build a flexible CUDA-based image processing pipeline in LabVIEW.

As the pipeline operates on 2D images, both classes support 1D or 2D arrays in a pitched configuration. **CuArray**, as the parent class, stores the pointer to the array, as well as the pitch, width and height. LabVIEW natively doesn't support pointer operations, therefore the pointer is simply cast to a 64 bit unsigned integer internally. As this is a private member of the class there is no danger of accidental modification. Being a descen-

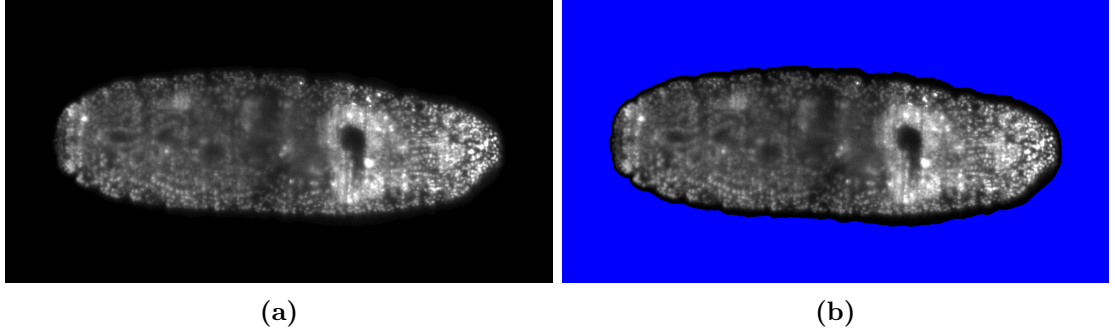


Figure 4.6: Applying mask to remove background. (a) Original image of a *Drosophila* embryo. (b) Background selected by thresholding the blurred image.

dent of `cuArray` class, the `Texture` class adds a further member to store the reference to the CUDA texture object. This class is used to implement the affine transformation, as it supports floating point indexing and automatic linear interpolation.

Since the processing is actually bottlenecked by the data transfer rate between the main memory and GPU memory, we implemented multiple commonly used image preprocessing operations for our pipeline to maximize the utility of the GPU. These functions include background subtraction, background masking and image compression. We will discuss these features in the following sections of the chapter.

4.2.5 Background subtraction and masking

As an additional step of the preprocessing pipeline, background subtraction and background masking was implemented. Background subtraction can improve image quality as it removes any system-specific patterns, while background masking is beneficial for the consecutive compression step.

To perform the background subtraction, dark images are recorded without the laser turned on. Typically 500–2000 images are taken which are averaged, to capture the pixel non-uniformities of the camera sensors. As this is camera specific, the step is repeated for all cameras. If necessary, the recordings can be repeated under different conditions, such as different exposure times, or different sensor modes (such as global shutter and rolling shutter). The averaged background images are saved in a custom file format in an HDF5 container [138] together with the camera serial number. The microscope software can read these files and applies the background subtraction to the appropriate cameras during imaging.

Background masking is a useful step to increase the efficiency of image compression. For light-sheet microscopy, where typically an entire embryo is imaged, the boundary of the specimen, and thus the area of interest, is well defined. Anything outside the embryo is just noise which does not contribute to any useful information. For image compression, however, these regions are extremely difficult to compress, as due to the

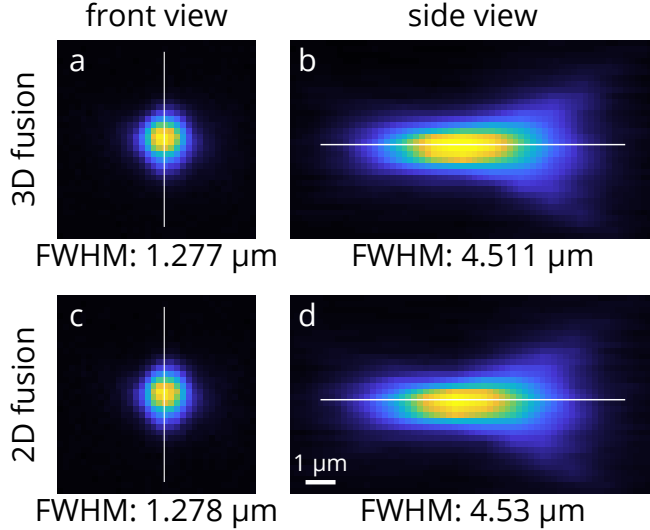


Figure 4.7: Comparison of 3D and 2D fusion of beads. Front and side views of a representative bead after 3D full affine fusion (a, b) and after 2D planewise fusion (c,d). FWHM was measured along the indicated lines, through the center of the bead image. Scale bar: 1 μm .

random nature of noise, almost no reduction is achievable (see 2.1). To circumvent this issue, the background pixels outside the specimen can be set to 0, which will greatly increase the compression ratio without compromising any data of interest [139].

The masking is performed in the following way. As the sample has much higher signal compared to the background, a thresholding operation is sufficient. In order to have a smooth mask, the images are first blurred by a Gaussian kernel, and the thresholding is done on the blurred image. This will define a binary mask with smooth boundaries, which is applied to the original image (Figure 4.6). The threshold can be calculated automatically by the Triangle method [140], or can also be user specified.

4.2.6 Methods and results

The image preprocessing pipeline was tested on our MuVi-SPIM microscope [45]. Processing speed of the CPU and GPU implementation of the processing pipeline was measured with the profiling tool of LabVIEW, and are an average of 10 runs. The benchmarking computer had 2 Intel Xeon E5620 processors with 8 processing cores running at 2.4 GHz, 24 GB RAM and an Nvidia GeForce GTX 750 graphics card. Test images were 2048 \times 2048 pixels at 16 bit depth.

For the background subtraction we recorded 1500 dark images with each camera and averaged them, in order to obtain the camera specific background images. Prior to image acquisition these were uploaded to the GPU memory, and were readily available for the pipeline. The implemented CUDA pipeline with background subtraction, 2D fusion and masking reached a throughput of 135.8 frames per second (fps), while a single-threaded

CPU implementation could only process 7.4 images per second on average.

Following careful alignment of the microscope to meet the previously discussed requirements (Eqs. 4.1 – 4.3), we imaged fluorescent beads in a gel suspension to obtain the affine transformation parameters. The measured 3D transformation parameters were the following:

$$\begin{pmatrix} 1.013 & 2.494 \times 10^{-3} & \mathbf{7.182 \times 10^{-3}} & -21.67 \\ -1.697 \times 10^{-3} & 1.014 & -\mathbf{3.192 \times 10^{-5}} & -4.161 \\ -\mathbf{9.694 \times 10^{-5}} & \mathbf{1.937 \times 10^{-7}} & \mathbf{1.003} & -\mathbf{0.433} \\ 0 & 0 & 0 & 1 \end{pmatrix}$$

Substituting these values to Eqs. 4.1 – 4.3 and evaluating for the full range of x, y, z , the maximum contribution of the discarded coefficients for each coordinate will be:

$$\begin{aligned} \max |cz| &= 0.070 \mu\text{m} \\ \max |gz| &= 3.11 \times 10^{-4} \mu\text{m} \\ \max |ix + jy + (k - 1)z + l| &= 0.7789 \mu\text{m} \end{aligned}$$

As these are below the resolution of the microscope, discarding the coefficients and reducing the 3D transformation to a 2D transformation will not have any negative effects on the image quality.

To validate our hypotheses, we fused bead stacks that were acquired for the calibration using both the 3D and the 2D transformations. The 2D, planewise fused beads do not exhibit any pathological morphologies compared to the 3D fused beads (Figure 4.7). When measuring the size of the bead images (FWHM) along the lateral and axial directions, the difference is less than 0.5% compared to the 3D fused dataset. This is well below any resolvable features.

We applied the direct fusion method to various biological specimens, such as *Drosophila melanogaster* embryos, zebrafish larvae, *Phallusia mammillata* embryo and *Volvox* algae. As a demonstration, here we show the results of imaging a *Drosophila* embryos expressing H2Av-mCherry histone marker. The embryos were imaged first without direct fusion enabled, and immediately afterwards with direct fusion enabled (Figure 4.8). Image quality dependency on the depth of the imaging plane is especially apparent in single-view stacks. Planes closer to the objective give a sharp, high contrast image, while planes deeper inside the embryo are severely degraded due to scattering (Figure 4.9).

Stacks obtained with the live fusion enabled show a consistently high image quality throughout the entire stack, independent of the depth (Figure 4.9). This allows us to keep only the already fused data, thus effectively reducing the storage requirement by half, and facilitating further data processing steps.

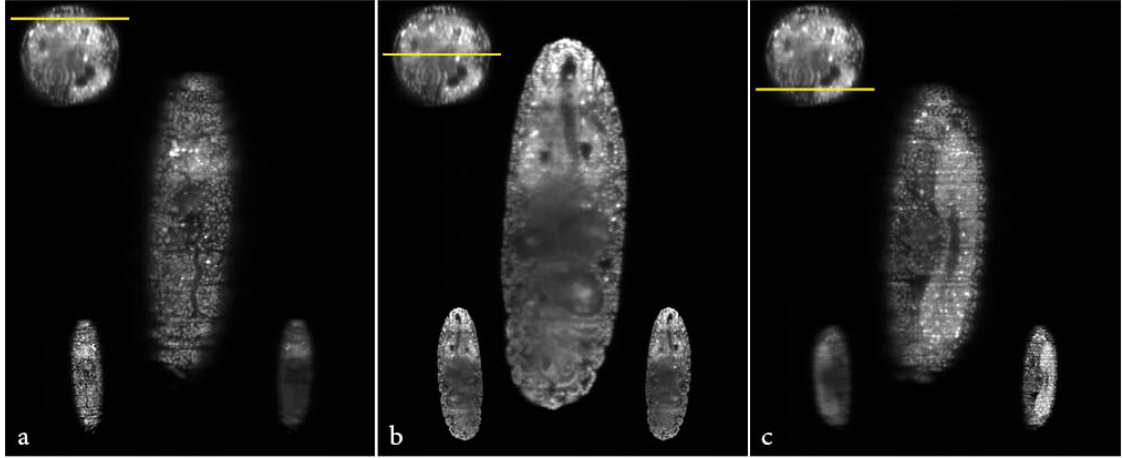


Figure 4.8: GPU fused images of a *Drosophila melanogaster* embryo. Two stacks were taken in quick succession first without fusion, then with fusion enabled. Fused images are shown in the middle of each subfigure, while the individual camera images are in the bottom insets. The top-left inset depicts the z-position of the shown images. (a) Image from closer to the left camera. (b) Image from the center of the embryo. (c) Image from closer to the right camera.

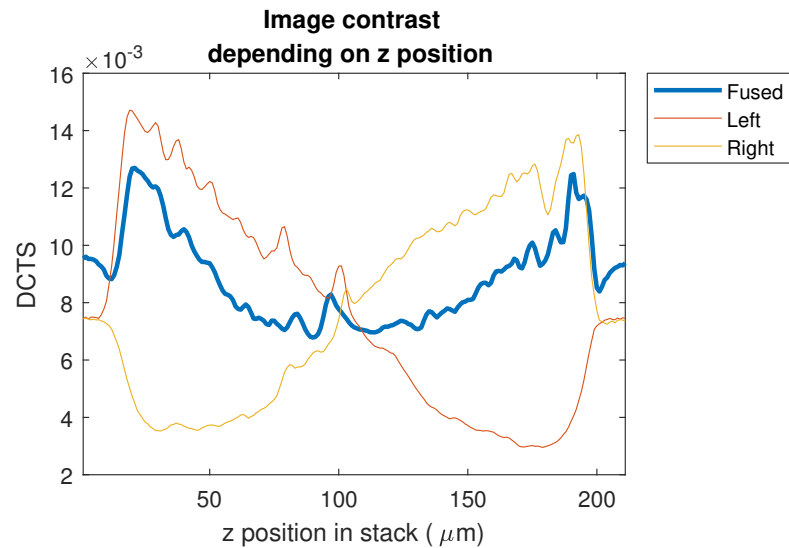


Figure 4.9: Image contrast depending on z position for raw and fused stacks. Image contrast was measured as the Shannon entropy of the normalized Discrete Cosine Transform of the sections [141]. Contrast measurements were performed on the images shown on Figure 4.8.

4.3 B³D image compression

The second part of our GPU-based image preprocessing pipeline is a new image compression algorithm that allows for extremely fast image compression to efficiently reduce data sizes already during acquisition. Although this would not reduce the requirements for image processing power and time, it still has a big impact on the necessary background infrastructure. By reducing the data size, not only the cost for storage can be reduced, but also the time it takes to transfer the data during the various steps of data processing is shortened. A fast compression method would also greatly improve 3D data browsing possibilities, as more data could be piped to the rendering software.

Despite the advantages, real-time compression for high-speed microscopy has not been available, and this is mostly due to the lack of appropriate compression methods suitable for scientific imaging that also offers the high throughput demanded by these applications. While typically used lossless compression methods, such as JPEG2000 [142] offer good compression ratios, they are very slow in processing speed, at least compared to the data rate of a modern microscope ($\sim 1 \text{ GB/s}$, Figure 4.1). High-speed compression methods that can deal with this data rate have been developed for ultra-high-definition 4K and 8K digital cameras, such as the high efficiency video codec (HEVC) [143]. These methods, however, have been optimized for lossy image compression which is generally not acceptable for scientific data [95], and rarely support compression of high bit rate originals, which is typically the case for modern sCMOS sensors. Although the HEVC recommendation does specify bit rates up to 16 bits, and lossless compression, the open source version, x265 only supports bit rates up to 12 bit [144].

To address these issues, we developed B³D, a GPU based image compression library capable of high-speed compression of microscopy images during the image acquisition process. By utilizing the massively parallel processing architecture of a GPU, we were not only able to reach a compression and decompression speed of 1 GB/s, but our algorithm also keeps the load off the CPU, making it available for other computing tasks related to operating the microscope itself.

A second feature of our compression library is a novel algorithm for noise-dependent lossy compression of scientific images. Although most lossy compression methods are not suitable for scientific data, our method allows for a deterministic way to control the exact amount of loss. The algorithm was designed in a way that any modification to a single pixel is proportional to the inherent image noise accounting for shot noise and camera read noise. Since this noise already introduces some uncertainty to the raw data, if any changes made are smaller than this, the extractable information by further data analysis steps should not be affected, whereas the compression ratio is massively increased.

4.3.1 Compression algorithm

Lossless compression

The algorithm design initially had three main requirements to ensure suitability for a high-speed microscopy environment: 1) low complexity for fast execution, 2) no data dependencies to enable parallel execution, and 3) full reversibility to ensure lossless compression. Since existing image compression standards such as JPEG2000 [142] or JPEG-LS [105] were designed to maximize compression ratio even at the expense of compression speed, these were not suitable for our needs. Furthermore, most steps inherently require sequential execution, thus preventing efficient parallelization. Promising efforts have been made to enable parallel compression by simplifying JPEG-LS and removing the limiting steps from the algorithm (such as Golomb parameter adaptation or context modeling) [107, 108]. Although some of these methods could reach a significant speedup with minimal expense in compression ratio, their performance was still not enough for real-time compression of high-speed microscopy data.

As in the case of other image compression methods, our algorithm has two main components: decorrelation and entropy coding (Figure 4.10a). In this work we focused on implementing a parallel encoder and decoder for the decorrelation part that would also be compatible with the noise-dependent lossy compression, as efficient CUDA-based entropy coders are already available [145]. To decorrelate the data, similarly to JPEG-LS and lossless-JPEG [104], a prediction is performed for each pixel by calculating the average of the top and left neighbors (Figure 4.10b). The prediction is subtracted from the real pixel value, resulting in the prediction error term:

$$\varepsilon = X - \text{Pred}(X). \quad (4.4)$$

Since the neighboring pixels have a high chance of correlation, these error terms will typically be very small compared to the raw intensity values. This step is similar to predictor 7 of lossless JPEG (see 2.3).

The pixel prediction method is especially well suited for parallel compression, as it can be performed independently for all pixels. For decompression, the top and left neighbor of a pixel need to be first reconstructed, thus parallelization needs some adjustments. An obvious choice is to perform the reverse prediction in tiles, where the number of threads will equal the number of tiles. Parallel execution can be further scaled up if the decoding is done in diagonals, starting from the top left corner (Figure 4.10c). With this method the average number of parallel threads will be

$$N_{th} = N_t * a_t / 2, \quad (4.5)$$

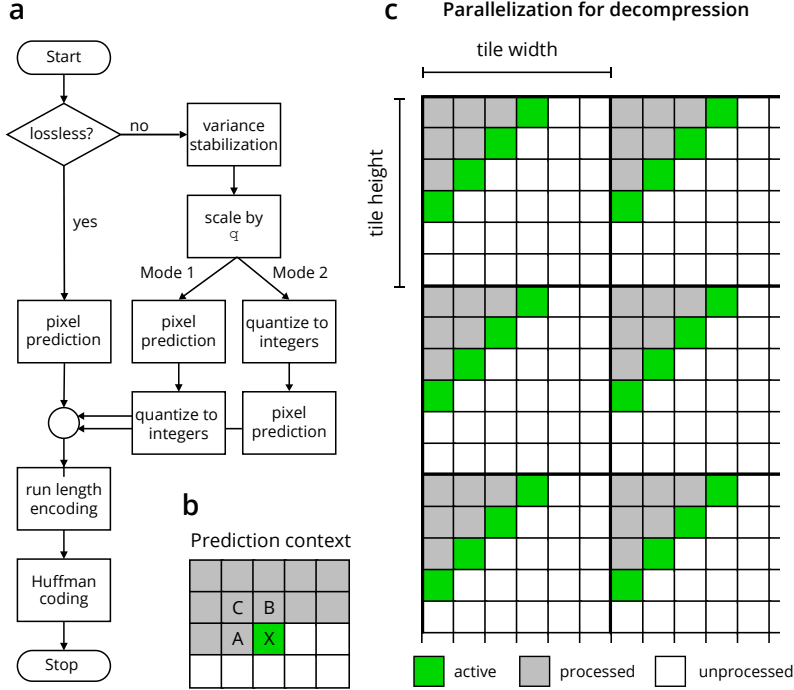


Figure 4.10: B³D algorithm schematics.

(a) Complete algorithm flowchart depicting the main stages of the compression. (b) Prediction context for pixel X, the next sample to be encoded. Three neighboring pixels are considered: left (A), top (B) and top left (C) neighbors. (c) Parallelization scheme for decompression and lossy compression. Already processed pixels are in gray, unprocessed pixels are in white, active pixels are in green.

where N_{th} is the number of threads, N_t is the number of tiles, a_t is the tile width and height for a square tile. Although the threads can be maximized by making smaller tiles, the compression ratio will be negatively affected. This is because the corner pixel can't be predicted, and for the edges only one neighbor can be used instead of 2. We find square tiles between 16 and 64 pixels are a good choice between decompression speed and compression ratio.

The prediction error terms are subsequently run-length encoded and entropy coded by a fast, CUDA-enabled Huffman coder [145, 146] to effectively reduce data size. The library is making extensive use of parallel prefix sum, which can be used for the effective parallel execution for both run-length encoding and Huffman coding. For decompression, the Huffman coding and run-length encoding are first reversed, then each pixel value is reconstructed from the neighboring values and the prediction errors. Although this implementation sacrifices a little in compression ratio compared to size-optimized methods, it can surpass a compression speed of 1 GB/s (see Section 4.3.2), which is sufficient even for the dual camera confocal MuVi-SPIM setup [75].

Within-noise-level compression

Noise-dependent lossy compression relies on the fact that microscopy images naturally contain photon shot noise. To increase compression ratio, this algorithm allows some differences in the pixel values, as long as they are within a predefined proportion of the inherent noise. A special case for this mode is when all compression errors are smaller than the standard deviation of the noise (σ), which we call within-noise-level (WNL) compression.

Our algorithm is inspired by both the near-lossless mode of JPEG-LS [105], where the maximum compression error can be set to a predefined value, and the square root compression scheme [147, 148], that quantizes its input relative to its square. We combine the two methods to achieve noise-dependent lossy compression while still retaining good image quality and avoiding banding artifacts.

Before the prediction errors are sent to the entropy coder, a quantization can take place that reduces the number of symbols that need to be encoded in order to increase compression ratio. By changing the quantization step, the maximum absolute reconstruction error can be defined, such as when using JPEG-LS. For noise dependent compression, however, the quantization step should be proportional to the image noise, which can be achieved by the following variance stabilizing transformation introduced by Bernstein *et al.* [148]:

$$T = 2\sqrt{e + \sigma_{RN}^2}, \quad (4.6)$$

where e is the intensity scaled to photoelectrons, and σ_{RN} is the standard deviation of the camera read noise. To perform the scaling of digital numbers (DN) to photoelectrons, it's necessary to know the camera offset and conversion parameters: $e = (I - \text{offset}) \cdot g$, where g is the gain in photoelectrons/DN, and I is the original pixel intensity. The transformation assumes a Poisson-Gaussian noise, incorporating the photon shot noise and the camera readout noise, which is a good model for most scientific imaging sensors, such as (EM)CCD or sCMOS.

To accommodate for all imaging needs, two options are available in the noise-dependent lossy mode. In Mode 1, after the stabilizing transform (Equation 4.6), the prediction is performed first, followed by quantization of the prediction errors. This mode reaches a better compression ratio and higher peak signal-to-noise ratio (PSNR) for the same quantization step compared to Mode 2 (Figure 4.11 a, b), and is recommended for most use cases. For larger quantization steps ($q \geq 3\sigma$), however, Mode 1 might introduce some spatial correlations, because the prediction errors that are being quantized depend on multiple adjacent pixels (Figure 4.11 c, d). Mode 2 excludes this possibility by swapping the quantization and prediction (Figure 4.11 c, d) at the expense of compression ratio. Since no correlations are introduced, Mode 2 is suitable for highly

sensitive image analysis tasks, such as single-molecule localization. In this chapter we use Mode 2 for single-molecule localization data, and Mode 1 for all other datasets.

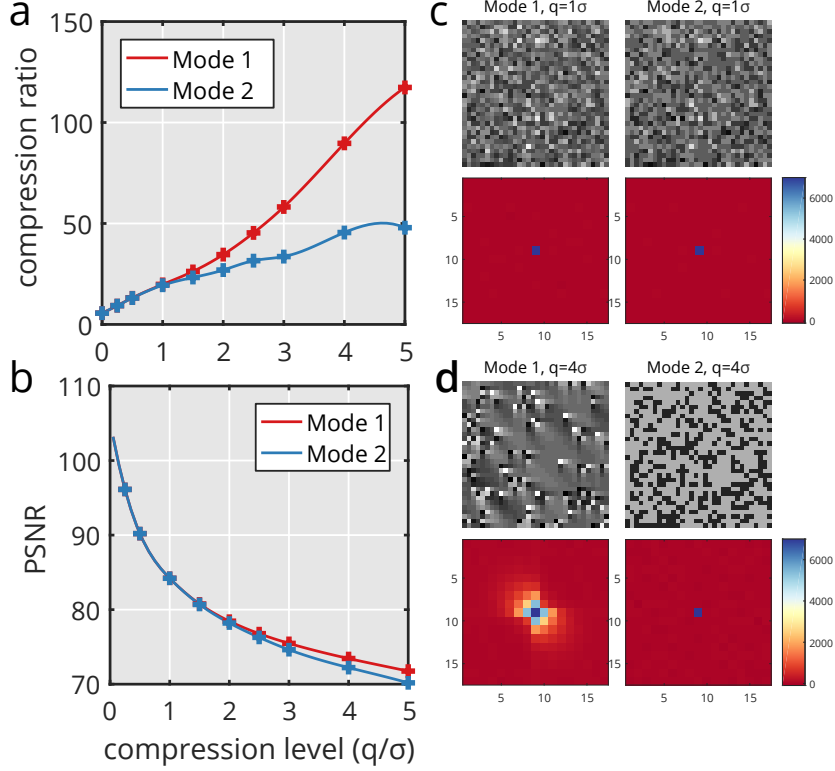


Figure 4.11: Options for noise-dependent lossy compression. Comparing Mode 1 (prediction then quantization) and Mode 2 (quantization then prediction) of noise-dependent lossy compression in terms of compression ratio, peak signal-to-noise ratio (PSNR) and spatial correlations introduced to random noise. (a) Compression ratio as a function of the quantization step for Mode 1 and Mode 2. (b) PSNR as a function of the quantization step for Mode 1 and Mode 2. (c, d) Random noise was compressed at various quantization steps both for Mode 1 and Mode 2. Autocorrelation was calculated for the compressed images to see whether the compression introduces any spatial correlation between the pixels. For $q=1\sigma$ both modes are free of correlation (c, top: compressed images, bottom: autocorrelation), however, for $q=4\sigma$ Mode 1 exhibits a correlation pattern (d, top left: compressed image, bottom left: autocorrelation) that is not present in Mode 2 (d, top right compressed image, bottom right: autocorrelation). For more discussion, see Section 4.3.1.

Additional noise introduced by compression

When applying quantization to any kind of data, the quantization error can be modeled as an additional uniform noise with standard deviation of $\frac{\delta}{\sqrt{12}}$, where δ is the quantization step size [149]. During compression the quantization is proportional to the standard deviation of the original image noise, thus the noise on the decompressed image will be:

$$\sigma_{out} = \sigma_{in} \cdot \sqrt{1 + \frac{q^2}{12}} \quad (4.7)$$

For the WNL case, when $q = 1\sigma$ this means an increase of 4%, which also coincides with the measured increase of localization error for single molecule localization (Figure 4.18a).

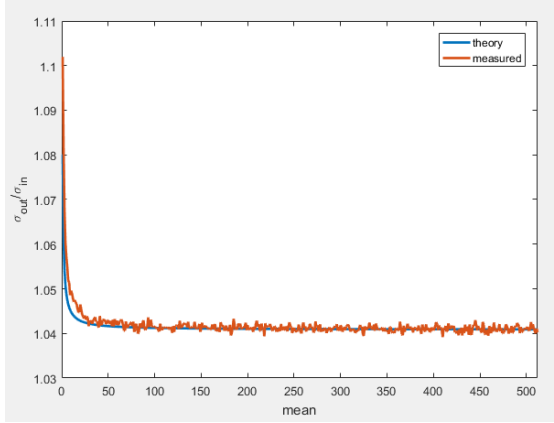


Figure 4.12: Theoretical and measured increase in image noise for WNL compression. Validating Equation 4.8, we plot the relative increase in image noise as a function of the mean. Blue line: plot of Equation 4.8 Red line: plot of measured data. To obtain the measurement, we compressed a stack of 512 images consisting of Poisson noise, each with a different mean. After WNL compression the dataset was read in Matlab, and the standard deviation was calculated for each frame. The ratio σ_{in}/σ_{out} is plotted as a function of the mean.

However, this is not the only source of additional noise we have to consider, because at the decompression step there is a possibility of getting floating point results after applying the inverse of the compression steps, and for most applications these have to be coerced to integer numbers. This effectively adds a second quantization, but now at a constant quantization step of 1. This results in an additional uniform noise with variance of $\frac{1}{12}$:

$$\sigma_{out} = \sigma_{in} \cdot \sqrt{1 + \frac{q^2}{12}} + \frac{1}{12} \quad (4.8)$$

We verified this by compressing 512 images (1024×1024 pixels) of random Poisson noise with different means (1–512), and calculated the standard deviation for each frame after the decompression step. Finally, we plotted the ratio σ_{out}/σ_{in} as a function of the mean m (Figure 4.12), and we found that it is in very good agreement with the theory outlined above.

4.3.2 Evaluation of the compression algorithm

We compared our algorithm's performance with some of the most commonly used image formats in the scientific field: TIFF (LZW) and JPEG2000. Furthermore, we also included the state of the art KLB compression [139], which was especially designed for fast compression of large light-sheet datasets. We measured compression speed, decompression speed and resulting file size for all algorithms (Figure 4.13a). Only B³D is capable of handling the sustained high data rate of modern sCMOS cameras typically used in light-sheet microscopy, while still maintaining compression ratios comparable to more complex, but much slower algorithms (Table B2 in Appendix B).

4.3 B³D image compression

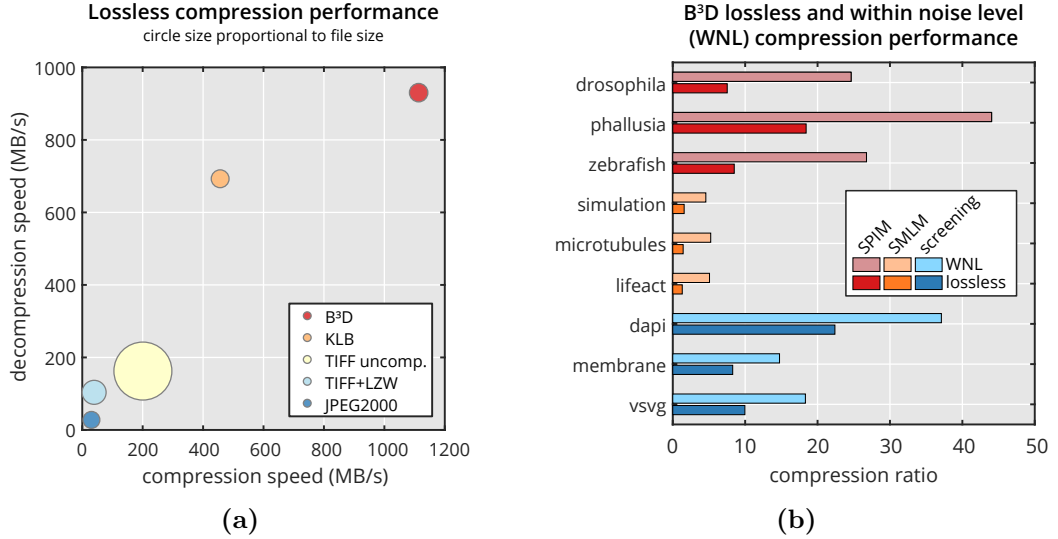


Figure 4.13: Compression performance. (a) Performance comparison of our B³D compression algorithm (red circle) vs. KLB (orange), uncompressed TIFF (light yellow), LZW compressed TIFF (light blue) and JPEG2000 (blue) regarding write speed (horizontal axis), read speed (vertical axis) and file size (circle size). (see also Table B2). (b) WNL compression performance compared with lossless performance for 9 different dataset representing 3 imaging modalities (SPIM, SMLM, screening). Compression ratio = original size / compressed size. For description of datasets see Table B3 in Appendix B.

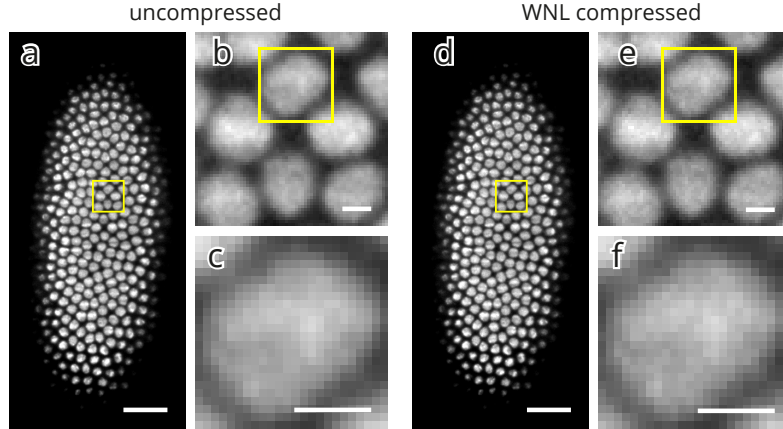


Figure 4.14: Image quality of a WNL compressed dataset. WNL compression of a *Drosophila* recording taken in the MuVi-SPIM setup. Compression ratio: 19.83. (a–c) Uncompressed image of the whole field of view (a), and zoomed in smaller regions (b, c). (d–f) WNL compressed image of the whole field of view (d), and zoomed in smaller regions (e, f). Scale bars: 25 µm (a, e); 2.5 µm (b, c, e, f).

Using the noise-dependent lossy mode with $q = 1\sigma$ (WNL), the compression ratio massively increases for all imaging modalities compared to the lossless mode (Figure 4.13b) without any apparent loss in image quality (Figure 4.14). Furthermore, the average compression error is considerably smaller than the image noise itself (Figure 4.15).

To see how the noise-dependent compression affects common imaging pipelines, we tested the effect of different levels of compression on 3D nucleus and membrane segmentation in light-sheet microscopy, and on single-molecule localization accuracy in super-

4.3 B³D image compression

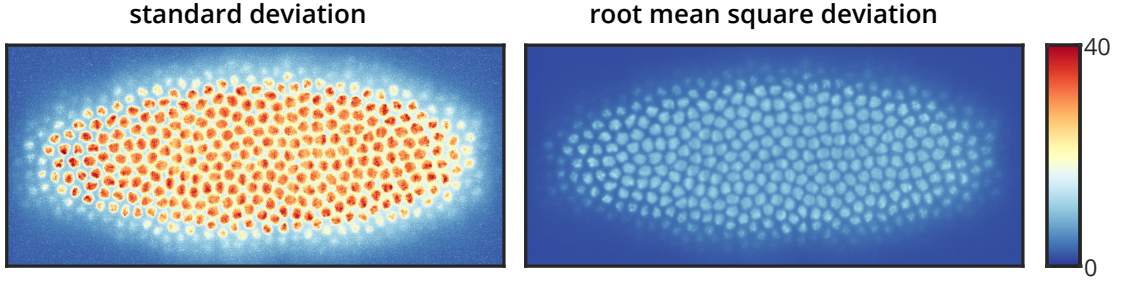


Figure 4.15: Compression error compared to image noise. To compare the difference arising from WNL compression to image noise, we imaged a single plane 100 times in a *Drosophila melanogaster* embryo expressing H2Av-mCherry nuclear marker at 38 ms intervals. The whole acquisition took 3.8 s, for which the sample can be considered stationary. To visualize image noise, the standard deviation was calculated for the uncompressed images (left). All images were then WNL compressed, and the root mean square deviation was calculated compared to the uncompressed images (right). The root mean square deviation on average is 3.18 times smaller than the standard deviation of the uncompressed images.

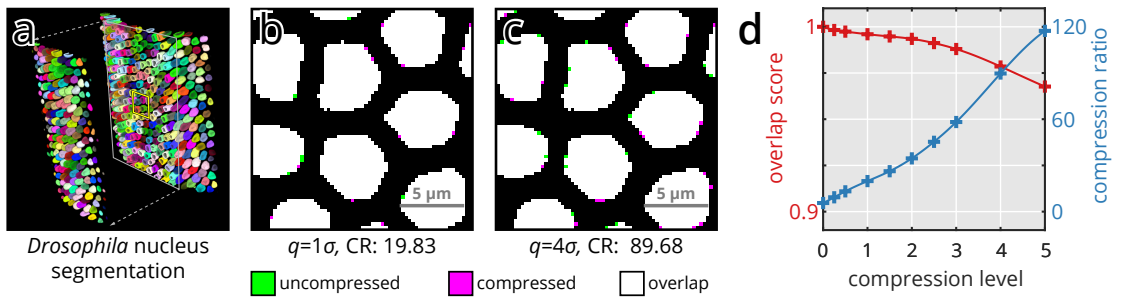


Figure 4.16: Influence of noise-dependent lossy compression on 3D nucleus segmentation. A *Drosophila melanogaster* embryo expressing H2Av-mCherry nuclear marker was imaged in MuVi-SPIM [45], and 3D nucleus segmentation was performed (Section 4.3.4) (a). The raw dataset was subsequently compressed at increasingly higher compression levels, and segmented based on the training of the uncompressed data. To visualize segmentation mismatch, the results of the uncompressed (green) and compressed (magenta) datasets are overlaid in a single image (b, c; overlap in white). Representative compression levels were chosen at two different multiples of the photon shot noise, at $q=1\sigma$ (b) and $q=4\sigma$ (c). For all compression levels the segmentation overlap score (Section 4.3.4) was calculated and is plotted in (d) along with the achieved compression ratios.

resolution microscopy. First, we imaged a *Drosophila melanogaster* embryo expressing an H2Av-mCherry nuclear marker in the MuVi-SPIM and segmented the nuclei with Ilastik [150] (Figure 4.16a and Section 4.3.4). Then we performed noise dependent compression at various quality levels and calculated the segmentation overlap compared to the uncompressed stack (Section 4.3.4). At WNL compression ($q = 1\sigma$) the segmentation overlap is almost perfect (Figure 4.16b) with an overlap score of 0.996. Even when increasing the quantization step to 4σ (Figure 4.16c) the overlap score stays at 0.98 and only drops below 0.97 when the compression ratio is already above 120 (quantization step of 5σ , Figure 4.16d). We got similar results for a membrane segmentation pipeline that is used with *Phallusia mammillata* embryos (Figure 4.17 and Section 4.3.4).

Next, we evaluated our compression algorithm in the context of single molecule localization microscopy (SMLM), and measured how the localization precision is affected

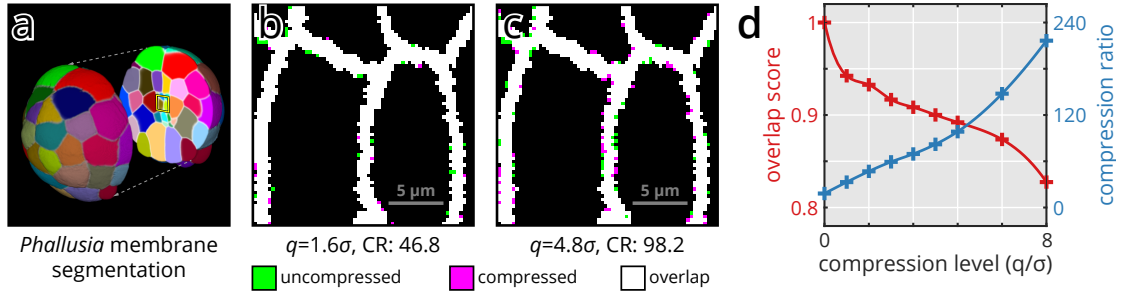


Figure 4.17: Influence of noise-dependent lossy compression on 3D membrane segmentation. A *Phallusia mammillata* embryo expressing PH-citrine membrane marker was imaged in MuVi-SPIM [45], and 3D membrane segmentation was performed (Section 4.3.4) (a). The raw dataset was subsequently compressed at increasingly higher compression levels, and segmented using the same settings as the uncompressed data. To visualize segmentation mismatch, the results of the uncompressed (green) and compressed (magenta) datasets are overlaid in a single image (b, c; overlap in white). Representative compression levels were chosen at two different multiples of the photon shot noise, at $q=1.6\sigma$ (b) and $q=4.8\sigma$ (c). For all compression levels the segmentation overlap score (Section 4.3.4) was calculated and is plotted in (d) along with the achieved compression ratios.

when compressing the raw images by an increasing compression ratio. We compressed an SLM dataset of immuno-detected microtubules (Figure 4.18a) with increasing compression levels. For WNL compression ($q = 1\sigma$) no deterioration of the image was visible (Figure 4.18b), and even for the case of $q = 4\sigma$ the compression induced errors were much smaller than the resolvable features (Figure 4.18c). To quantify the impact of compression on the localization error, we used a simulated dataset (Section 4.3.4) and compared the localization output of different compression levels to the ground truth (Figure 4.18d). Lossless compression resulted in a compression ratio of 2.7, whereas WNL compression reached a compression ratio of 5.0, while increasing the localization error by only 4%. This also coincides with the theoretical increase of image noise (Section 4.3.1). Furthermore, the increase in localization error was not dependent on the signal to background noise ratio (Figure 4.19).

4.3.3 HDF5 integration

To make our compression method more accessible, we developed a filter plugin for HDF5. Because of its versatility, HDF5 has emerged as the *de facto* standard in the open source light-sheet microscopy field, and is also the basis for the widely used BigDataViewer [151] in Fiji [116]. Starting from version 1.8.11 (May 2013), HDF5 supports dynamically loaded filters, and is able to load third party components without having to modify any already installed files. When loading a B³D compressed image in an HDF5 enabled application, the library automatically calls our filter plugin, decompresses the image on the GPU, and copies it back into CPU memory.

Since HDF5 is extensively used in many scientific/image analysis software, this plugin format is especially suitable to equip existing software with compression/decompression

4.3 B³D image compression

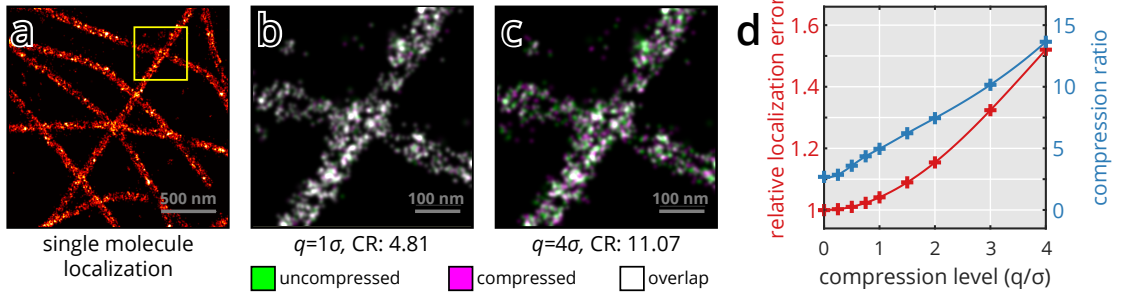


Figure 4.18: Influence of noise-dependent lossy compression on single-molecule localization. Microtubules, immunolabeled with Alexa Fluor 647 were imaged by SMLM (a). The raw dataset was compressed at increasingly higher compression levels, and localized using the same settings as the uncompressed data. To visualize localization mismatch, the results of the uncompressed (green) and compressed (magenta) datasets are overlaid in a single image (b, c; overlap in white). Two representative compression levels were chosen at $q=1\sigma$ (b) and $q=4\sigma$ (c). To assess the effects of compression on localization precision, a simulated dataset with known emitter positions was compressed at various levels. For all compression levels the relative localization error (normalized to the Cramér–Rao lower bound) was calculated and is plotted in (d) along with the achieved compression factors.

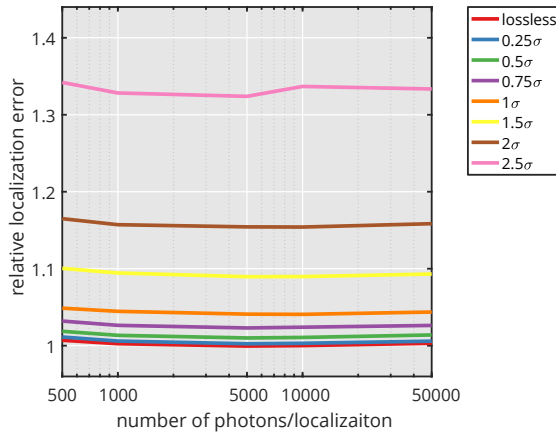


Figure 4.19: Change in localization error only depends on selected quantization step. We simulated multiple datasets (Section 4.3.4) with different average photon numbers per localization. Background was kept at a constant average of 20 photons/pixel. Datasets were compressed at multiple compression levels (see legend), and localization error relative to the Cramér–Rao lower bound was calculated. The relative localization error only depends on the compression level, and not on the signal to background illumination ratio.

capabilities. To read compressed files no modification is required, and any software supporting HDF5 should be compatible. The following software have been tested with our filter plugin and are able to read B³D compressed files: Fiji (also with BigDataViewer), Imaris 8.4.1, Ilastik 1.2.0, Matlab R2016a, Python 2.7.10 and 3.5.3, LabVIEW 2015, C++.

Writing compressed HDF5 files is possible if the user has direct control over the file writing routine, as an additional command is required to set up compression. This functionality has been tested in the following environments: C++, Python 2.7.10 and 3.5.3, LabVIEW 2015.

4.3.4 Methods

Compression benchmarking

For all presented benchmarks, TIFF and JPEG2000 performance was measured through MATLAB's imwrite and imread functions, while KLB and B³D performance was measured in C++. All benchmarks were run on a computer featuring 32 processing cores (2×Intel Xeon E5-2620 v4), 128 GB RAM and an NVIDIA GeForce GTX 970 graphics processing unit. Read and write measurements were performed in RAM to minimize I/O overhead, and are an average of 5 runs. SMLM datasets were provided by Joran Deschamps (EMBL, Heidelberg), and were originally published in [152] and [153]. Screening datasets were provided by Jean-Karim Hériché (EMBL, Heidelberg), and were originally published in [154]

Light-sheet imaging

Drosophila embryos were imaged in the MuVi-SPIM setup [45] using the electronic confocal slit detection (eCSD) [75]. Embryos were collected on an agar juice plate, and dechorionated in 50% bleach solution for 1 min. The embryos were then mounted in a shortened glass capillary (Brand 100 µl) filled with 0.8% GelRite (Sigma-Aldrich), and pushed out of the capillary to be supported only by the gel.

3D nucleus segmentation

3D nucleus segmentation of *Drosophila* embryos was performed using Ilastik [150]. The original dataset was compressed at different quantization levels, then upscaled in z to obtain isotropic resolution. To identify the nuclei, we used the pixel classification workflow, and trained it on the uncompressed dataset. This training was then used to segment the compressed datasets as well. Segmentation overlap was calculated in Matlab using the

Sørensen–Dice index [155, 156]:

$$QS = 2 |A \cap B| / (|A| + |B|) \quad (4.9)$$

where the sets A and B represent the pixels included in two different segmentations.

3D membrane segmentation

Raw MuVi-SPIM recordings of *Phallusia mammillata* embryos expressing PH-citrine membrane marker were kindly provided by Ulla-Maj Fiuba (EMBL, Heidelberg). Each recording consisted of 4 views at 90 degree rotations. The views were fused using an image based registration algorithm followed by a sigmoidal blending of the 4 views. The fused stack was then segmented using the MARS algorithm [157] with an hmin parameter of 10. The raw data (all 4 views) was compressed at different levels, and segmented using the same pipeline. Segmentation results were then processed in Matlab to calculate the overlap score for the membranes using the Sørensen–Dice index.

Single-molecule localization imaging

In order to visualize microtubules, U2OS cells were treated as in [152] and imaged in a dSTORM buffer [158]. In brief, the cells were permeabilized and fixed with glutaraldehyde, washed, then incubated with primary tubulin antibodies and finally stained with Alexa Fluor 647 coupled secondary antibodies. The images were recorded on a home-built microscope previously described [152], in its 2D single-channel mode.

Single-molecule localization data analysis

Analysis of single-molecule localization data was performed on a custom-written MATLAB software as in [153]. Pixel values were converted to photon counts according to measured offset and calibrated gain of the camera (EMCCD iXon, Andor). The background was estimated with a wavelet filter [159], background-subtracted images were thresholded and local maxima were detected on the same images. 7-pixel ROIs around the detected local maxima were extracted from the raw images and fitted with a GPU based MLE fitter [160]. Drift correction was performed based on cross-correlation. Finally, images were reconstructed by filtering out localizations with a high uncertainty (>30 nm) and large PSF (>150 nm) and Gaussian rendering.

Simulation of single-molecule localization data

Single molecule localization datasets were simulated in Matlab by generating a grid of pixelated Gaussian spots with standard deviation of 1 pixel. With a pixel size of a 100

nm, this corresponds to a FWHM of 235.48 nm. The center of each spot was slightly offset from the pixel grid at 0.1 pixel increments in both x and y directions. To this ground truth image a constant value was added to simulate illumination background, and finally Poisson noise was applied to the image. This process was repeated 10,000 times to obtain enough images for adequate accuracy.

Code availability

Code used for analyzing data, B³D source code and compiled binaries, including a filter plugin for HDF5, are available for download at <https://git.embl.de/balazs/B3D>.

4.4 Discussion

In this chapter we presented a real-time image preprocessing and compression pipeline for multiview light-sheet microscopy. This pipeline is capable of fusing opposing views recorded in the MuVi-SPIM faster than the acquisition rate, as well as compressing the acquired data during imaging. Both of these are important steps in the data preprocessing, especially given the very high data production rate of the microscope. As a single experiment can reach tens of terabytes, any kind of processing that can be performed during acquisition can immensely facilitate further analysis.

When using the full 3D fusion pipeline the data not only takes up twice as much storage space, but due to the demanding processing requirements the fusion process can take a considerable amount of time. Since this step is necessary before any further evaluation of the data can take place, it acts as a bottleneck in an efficient workflow. Using the direct fusion this issue is greatly alleviated.

A further benefit of the direct fusion is that it can also run during setting up the experiments, in the “live” view, and the fused view replaces the two camera views. This helps the users to better assess image quality, and expedites setting up the experiments.

For experiments where more than two views are necessary and the sample is also rotated, the direct fusion can’t completely replace the previous 3D fusion method, as it can not account for any transformation outside the common focal plane. However, even for these experiments the raw data is reduced by a factor of two, and the 3D fusion task is also simplified, since the number of distinct views are halved.

The compression algorithm is implemented in C++, and allows for easy integration through an API with various programming languages. The library was tested on Linux (Ubuntu 16.04) and Windows (10). Additionally, we implemented a filter plugin for HDF5 which enables a seamless integration in all software packages that are supporting the native HDF5 library, such as Matlab, Python, Imaris, or Ilastik. Due to B³D’s efficient compression ratio and its high decompression speed, loading data is often accelerated: For

a state-of-the-art hard drive with 200 MB/s bandwidth, loading a 2 GB uncompressed 3D stack of images takes about 10 seconds. With an average compression ratio of 20 fold in the WNL mode, the loading time is reduced to 0.5 seconds followed by 2 seconds of decompression, which yields a factor of four speed-up.

It is also worth to note, that the achieved WNL compression reduces the camera data rate to below 40 MB/s, well below the 1 Gb/s Ethernet standard. This enables to use current network infrastructure to move data to long term storage and even makes the use of cloud services possible. Altogether, B³D, our efficient GPU-based image compression library allows for exceptionally fast compression speed and greatly increases compression ratio with its WNL scheme, offering a versatile tool that can be easily tailored to many high-speed microscopy environments.

Chapter 5

Conclusions

Each chapter was concluded by their own discussions. Here, the new scientific results are summarized, and an outlook is provided for the possible future applications.

5.1 New scientific results

Thesis I. *I have designed and constructed a new light-sheet microscope suitable for high resolution imaging of delicate samples. A novel arrangement of two high numerical aperture objectives in 120 degrees combined with a tilted light-sheet allows for near isotropic resolution while increasing light collection efficiency by a factor of two.*

Corresponding publications: [J1], [J2], [J3]

Dual Mouse-SPIM is a novel design for symmetric light-sheet microscopy. The use of high NA objectives in 120° not only increases volumetric resolution compared to the conventional 90° setup, but due to the larger detection angle, light collection efficiency is doubled. This is especially beneficial for delicate, light-sensitive specimens, such as mouse embryos, since phototoxic effects are reduced while the contrast is preserved.

As part of the microscope I have designed a custom beam splitter unit that allows the use of a single galvo scanner to generate the light-sheet for both objectives. I have also designed a custom detection merging unit that allows the use of a single camera for both detection views.

I have characterized the optical properties of the microscope, measured the illumination profile and point spread function. With a 3.6 µm thick light-sheet, a 95 µm field of view is evenly illuminated. Dual view imaging of bead samples revealed a lateral resolution of 314 nm, and axial resolution of 496 nm. This is a 2.67× improvement compared to the axial resolution of a single lens. I have also demonstrated the imaging capabilities of the microscope on *Drosophila* embryos and mouse zygotes.

Thesis II. *I have developed a GPU-based image processing pipeline for multi-view light-sheet microscopy that enables real-time fusion of opposing views.*

Corresponding publications: [C1], [C2], [C3]

I have developed a GPU-based image preprocessing pipeline, which integrates directly to our universal microscope control software in LabVIEW. The pipeline currently supports background subtraction and background masking, furthermore it is capable of fusing opposing views of the same plane faster than real-time. I have shown that it is possible to reduce the registration of opposing camera views from a 3D alignment to a 2D alignment without any negative effects in image quality and resolution. This massively reduces the necessary computing resources, and allows the use of CUDA textures for faster than real-time image fusion. Processing speed of this implementation is 138 fps, a $18.3 \times$ increase compared to a single threaded CPU implementation.

Thesis Group III. *Real-time image compression.*

Thesis III/1. *I have developed a new image compression algorithm that enables noise dependent lossy compression of light microscopy images, and can reach a compression ratio of 100 fold while preserving the results of downstream data analysis steps. A fast CUDA implementation allows for real-time image compression of high-speed microscopy images.*

Corresponding publications: [J4], [C1], [C2], [C3]

Since many high-speed microscopy methods generate immense amounts of data, easily reaching terabytes per experiment, image compression is especially important to efficiently deal with such datasets. Existing compression methods suitable for microscopy images are not able to deal with the high data rate of modern sCMOS cameras ($\sim 800 \text{ MB/s}$).

I developed a GPU-based parallel image compression algorithm called B³D, capable of over 1 GB/s throughput, allowing live image compression. To further reduce the data size, I developed a noise dependent lossy compression that only modifies the data in a deterministic manner. The allowed differences for each pixel can be specified as a proportion of the inherent image noise, accounting for photon shot noise and camera readout noise. Due to the use of pixel prediction, the subjective image quality is higher than for other methods that simply quantize the square root of the images.

Thesis III/2. *I have shown that within noise level compression does not significantly affect the results of most commonly used image processing tasks, and it allows a $3.32 \times$ average increase in compression ratio compared to lossless mode.*

Corresponding publications: [J4], [C1], [C2], [C3]

As data integrity in microscopy is paramount for drawing the right conclusions from the experiments, using a lossy compression algorithm might be controversial. I have shown that the within noise level (WNL) mode of B³D does not significantly affect the results of several commonly used image analysis tasks. For light-sheet microscopy data I have shown that WNL compression introduces less variation to the image than the photon shot noise. When segmenting nuclei of *Drosophila* embryos and membranes of *Phallusia* embryos, the overlap of the segmented regions of uncompressed and WNL compressed datasets were 99.6% and 94.5% respectively, while compression ratios were 19.83 for *Drosophila* and 40.01 for *Phallusia* embryos. For single molecule localization microscopy data I have shown that WNL compression only introduces 4% increase in localization uncertainty, while the average compression ratio is increased from 1.44 (lossless) to 4.96 (WNL). I have also shown that change in localization error due to the compression does not depend on the SNR of the input images.

5.2 Application of the results

Both the new Dual Mouse-SPIM microscope and the GPU-based image processing and compression pipeline have direct applications in light-sheet imaging of embryonic development.

Multiple potential collaborators indicated their interest in using the Dual Mouse-SPIM for their studies in mouse embryonic development. The Hiiragi group, focusing on symmetry breaking events in the pre-implantation and early post-implantation stages would like to use this system for imaging larger specimens from multiple direction, which is not possible on their current microscopes, and could allow them to observe previously unknown mechanisms. The Ellenberg group is interested in investigating chromosome missegregation mechanisms in the first few divisions during embryonic development. The increased axial resolution of this system will allow to track each individual chromosome during the division process, which was not possible on their current setup due to the insufficient axial resolution.

The GPU-based image processing pipeline, especially the 2D fusion of opposing views is already being used on our lab's workhorse microscope, the MuVi-SPIM. Being able to fuse the two views of the opposing objectives during imaging not only results in considerable storage space savings, but significantly speeds up the data analysis as well.

The image compression algorithm, B³D, although was developed with light-sheet microscopy in mind, has a more wide-spread use-case. Any kind of high-speed, high-throughput light-microscopy experiment can benefit from the massive data reduction offered by the within noise level mode. Since the compression can also be done immediately during imaging, not only the storage requirements, but the data bandwidth is

5.2 Application of the results

reduced as well, which renders the use of high performance RAID arrays and 10 Gbit networks unnecessary, further reducing costs. Due to the similarly high decompression speed, reading the data is also accelerated, which can be beneficial for data browsing and 3D rendering applications. Several companies of different fields already expressed their interest in the compression library, including Bitplane AG (3D data analysis and visualization), Luxendo GmbH (light-sheet microscopy), and Hamamatsu Photonics K.K. (camera and sensor manufacturing).

Appendix

A Bill of materials

Optical components

- Lenses
 - 2×Nikon CFI75 Apo LWD 25x/1.10w water dipping objectives
 - 2×Nikon ITL200 200 mm tube lens
 - 2×200 mm x 25 mm Dia. achromatic lens (Edmund Optics, #47-645)
 - 2×400 mm x 40 mm Dia. achromatic lens (Edmund Optics, #49-281)
 - 3×75 mm x 25 mm Dia. achromatic lens (Edmund Optics, #47-639)
 - SILL 112751 1:2 beam expander
- Filters
 - 2×BrightLine quad-edge dichroic beam splitter (Semrock, Di03-R405/488/561/635-t3-25x36)
 - EdgeBasic 488 nm long pass filter (Semrock, BLP01-488R-25)
 - BrightLine 525/50 band pass filter (Semrock, FF03-525/50-25)
 - EdgeBasic 561 nm long pass filter (Semrock, BLP02-561R-25)
 - RazorEdge 647 nm long pass filter (Semrock, LP02-647RU-25)
- Mirrors
 - 6×1” Broadband Dielectric Elliptical Mirror (Thorlabs, BBE1-E03)
 - 2×30 mm Broadband 1/10λ Mirror (OptoSigma, TFMS-30C05-4/11)
 - 10 Pack of 1” Protected Silver Mirrors (Thorlabs, PF10-03-P01-10)
 - Knife-Edge Right-Angle Prism Dielectric Mirror (Thorlabs, MRAK25-E02)

Mechanical components

- 40 mm travel range pneumatic cylinder (Airtac, HM-10-040)
- 5/2-way electric valve (Airtac, M-20-510-HN)
- 2×25 mm extended contact bearing steel stage (OptoSigma, TSDH-251C)
- 30x90 mm stainless steel slide (OptoSigma, IPWS-F3090)
- close proximity gimbal mirror mount (Thorlabs, GMB1/M)
- 30 mm cage elliptical mirror mount (Thorlabs, KCB1E)
- Melles Griot Performance Plus Optical Breadboard
- 4×Newport Stabilizer, High Performance laminar Flow Isolator, I-2000 Series

Custom parts

All parts are (anodized) aluminium, unless stated otherwise.

- 2×mirror holder block
- Front plate for objective, chamber and mirror mounting
- Imaging chamber (PEEK)
- Wedge ring and matching threaded ring to fasten objectives
- Camera bridge
- Illumination splitter unit
- adapter plates to mount stages

Electronics

- Embedded system (National Instruments, cRIO-9068) equipped with:
 - 2×C series digital I/O card (NI 9401)
 - 1×C Series 100 kS/s 4-channel Voltage Output Module (NI 9263)
 - 1×C Series 25 kS/s 16-channel Voltage Output Module (NI 9264)
- Omicron SOLE-3 laser combiner, with 488, 561 and 638 nm laser lines
- Andor Zyla 4.2 sCMOS Camera
- Galvanometric scanner mirror (Cambridge Technology, 6210B)
- 6 position filter wheel (Ludl Electronic Products, 96A361)
- Filter wheel controller unit (Ludl Electronic Products, MAC5000)
- 2 piezoelectric stages (Nanos Instruments, LPS-30-30-1-V2_61-S-N)
- 2 stage controller boards (Nanos Instruments, BMC101)

B Supplementary Tables

B Supplementary Tables

Table B1: Data sizes in microscopy. Typical devices used for confocal microscopy, high-content screening, single-molecule localization microscopy and light-sheet microscopy and their data production characteristics. Data visualized on Figure 4.1

	imaging device	image size	frame rate	data rate	data size
SPIM	2x sCMOS camera (e.g. Hamamatsu ORCA Flash4.0)	2048x2048	50/s	800 MB/s	10 TB
SMLM	2x EMCCD camera (e.g. Andor iXon Ultra 897)	512x512	56/s	56 MB/s	500 GB
screening	CCD camera (e.g. Hamamatsu ORCA-R2)	1344x1024	8.5s/	22 MB/s	5 TB
confocal	Zeiss LSM 880, 10 channels	512x512	5/s	12.5 MB/s	50 GB

Table B2: Lossless compression performance. B³D is compared with various popular lossless image compression methods regarding write speed, read speed and compression ratio (original size / compressed size). Data visualized on Figure 4.13.

	write speed	read speed	CR	file size
B³D	1,115.08 MB/s	928.97 MB/s	9.861	100%
KLB	283.19 MB/s	619.95 MB/s	10.571	93.28%
JPEG2000	31.94 MB/s	26.38 MB/s	11.782	83.69%
TIFF uncompressed	202.32 MB/s	161.08 MB/s	1.00	986.1%
TIFF + LZW	40.85 MB/s	102.37 MB/s	5.822	169.37%

B Supplementary Tables

Table B3: Datasets used for benchmarking compression performance.

Dataset name	Imaging modality	Description	Size (MB)
drosophila	SPIM	dataset acquired in MuVi-SPIM of a <i>Drosophila melanogaster</i> embryo expressing H2Av-mCherry nuclear marker	494.53
zebrafish	SPIM	dataset acquired in MuVi-SPIM of a zebrafish embryo expressing b-actin::GCaMP6f calcium sensor	2,408.00
phallusia	SPIM	dataset acquired in MuVi-SPIM of a <i>Phallusia mammillata</i> embryo expressing PH-citrine membrane marker	1,323.88
simulation	SMLM	MT0.N1.LD-2D simulated dataset of microtubules labeled with Alexa Fluor 647 from SMLMS 2016 challenge	156.22
microtubules	SMLM	microtubules immuno-labeled with Alexa Fluor 674-bound antibodies in U2OS cells	1,643.86
lifeact	SMLM	actin network labeled with LifeAct-tdEOS in U2OS cells	3,316.15
dapi	screening	wide field fluorescence images of DAPI stained HeLa Kyoto cells [154]	1,005.38
vsvg	screening	wide field fluorescence images of CFP-tsO45G proteins in HeLa Kyoto cells [154]	1,005.38
membrane	screening	wide field fluorescence images of membrane localized CFP-tsO45G proteins labeled with AlexaFluor647 in HeLa Kyoto cells [154]	1,005.38

C Light collection efficiency of an objective

Let's define light collection efficiency η as the ratio of collected photons and all emitted photons:

$$\eta = \frac{N_{collected}}{N_{emitted}}$$

Since we can assume that the direction of photons emitted from a fluorescent molecule are random, the light collection efficiency will correspond to the solid angle subtended by the objective front lens at the focal point. To calculate this, let's consider the unit sphere centered at the focal point, and calculate the surface area of the spherical cap corresponding to the objective acceptance angle α (Fig. C1a). The area of the cap can be expressed as a function of the angle:

$$A_{cap} = 2\pi r^2(1 - \cos \alpha)$$

The surface area of the full sphere is calculated as:

$$A_{sph} = 4\pi r^2$$

For both equations r is the radius of the sphere. From here, the light collection efficiency can be calculated as:

$$\eta = \frac{N_{collected}}{N_{emitted}} = \frac{A_{cap}}{A_{sph}} = \frac{1 - \cos \alpha}{2}$$

As most objectives are characterized by the numerical aperture, we also plot η as a function of the NA on Figure C1b.

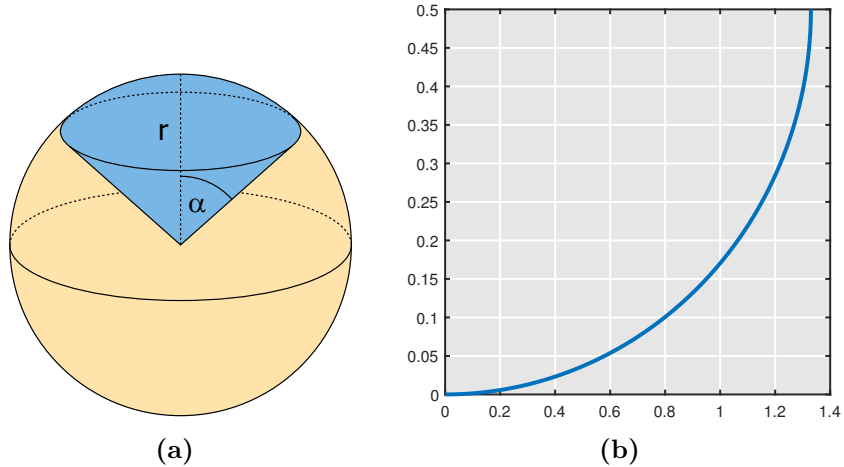


Figure C1: Light collection efficiency of an objective. (a) Light collection efficiency is the ratio of photons collected by the objective and all emitted photons. If the fluorophores are emitted randomly in all directions, it will be the surface ratio of the conical section (blue) to the whole sphere. (b) Light collection efficiency (η) as a function of the numerical aperture (NA).

D 3D model of Dual Mouse-SPIM

To view the 3D figure on the next page, Adobe Reader is required. Click on the figure to activate the 3D view.

Navigation:

- zoom: mouse wheel / right click and drag vertically
- rotate: left click and drag
- pan: left + right click and drag / Ctrl + click and drag

D 3D model of Dual Mouse-SPIM

Interactive 3D figure
Click to activate

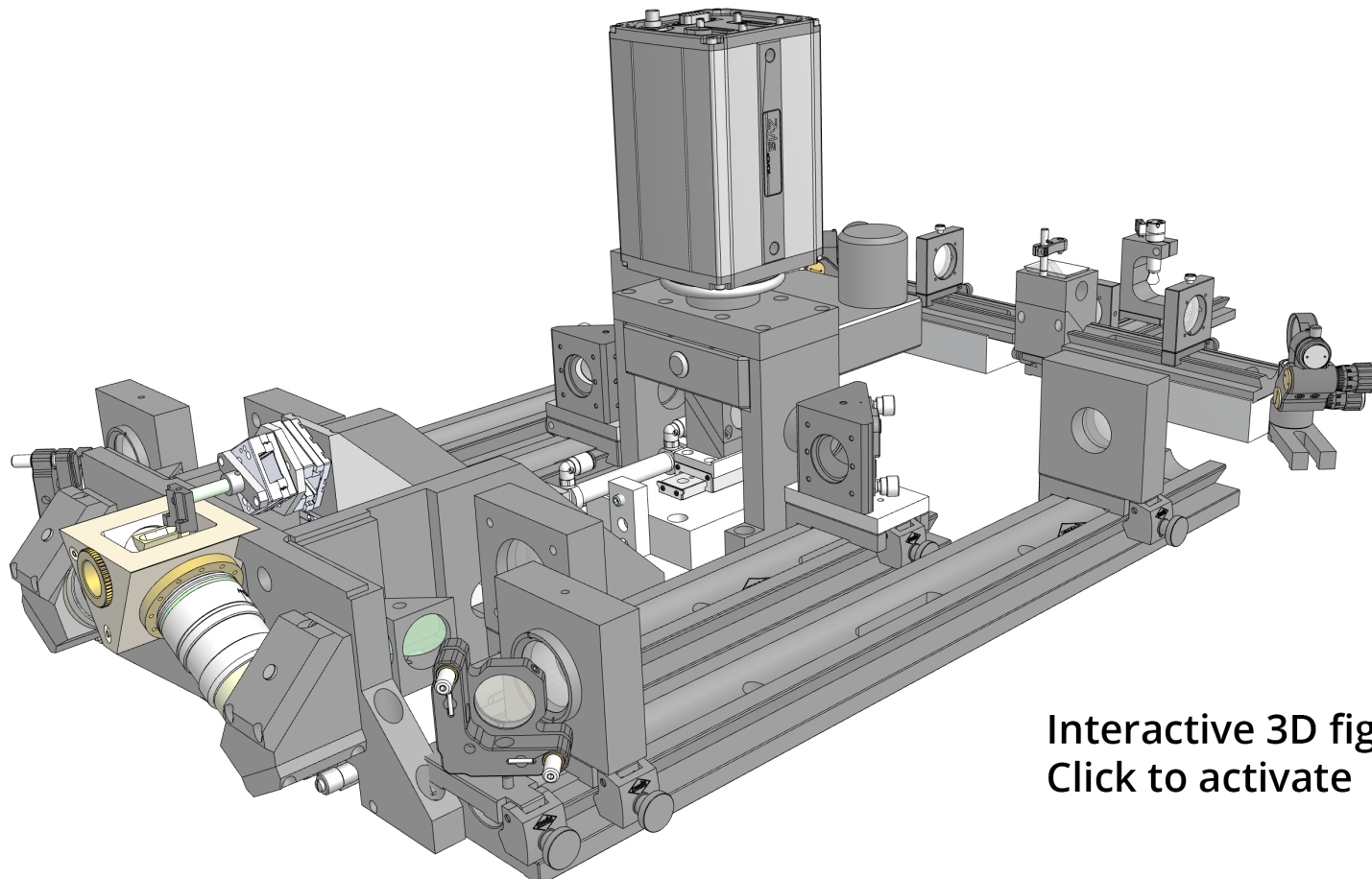


Figure D1: 3D model of DualMouse-SPIM.

References

The author's publications

- [J1] Patrick Hoyer, Gustavo de Medeiros, Bálint Balázs, Nils Norlin, Christina Besir, Janina Hanne, Hans-Georg Kräusslich, Johann Engelhardt, Steffen J. Sahl, Stefan W. Hell, and Lars Hufnagel. “Breaking the diffraction limit of light-sheet fluorescence microscopy by RESOLFT”. *Proceedings of the National Academy of Sciences* 113.13 (Mar. 2016), pp. 3442–3446. DOI: [10.1073/pnas.1522292113](https://doi.org/10.1073/pnas.1522292113) (cit. on pp. 16, 90).
- [J2] Petr Strnad, Stefan Gunther, Judith Reichmann, Uros Krzic, Balint Balazs, Gustavo de Medeiros, Nils Norlin, Takashi Hiragi, Lars Hufnagel, and Jan Ellenberg. “Inverted light-sheet microscope for imaging mouse pre-implantation development”. *Nature Methods* 13.2 (Feb. 2016), pp. 139–142. DOI: [10.1038/nmeth.3690](https://doi.org/10.1038/nmeth.3690) (cit. on pp. 15, 16, 23, 38, 90).
- [J3] Gustavo de Medeiros, Bálint Balázs, and Lars Hufnagel. “Light-sheet imaging of mammalian development”. *Seminars in Cell & Developmental Biology*. Mammalian development 55 (July 2016), pp. 148–155. DOI: [10.1016/j.semcdb.2015.11.001](https://doi.org/10.1016/j.semcdb.2015.11.001) (cit. on pp. 15, 90).
- [J4] Balint Balazs, Joran Deschamps, Marvin Albert, Jonas Ries, and Lars Hufnagel. “A real-time compression library for microscopy images”. *bioRxiv* (July 2017), p. 164624. DOI: [10.1101/164624](https://doi.org/10.1101/164624) (cit. on p. 91).

The author's others publications

- [J5] Zoltán Jakus, Edina Simon, Bálint Balázs, and Attila Mócsai. “Genetic deficiency of Syk protects mice from autoantibody-induced arthritis”. *Arthritis and Rheumatism* 62.7 (July 2010), pp. 1899–1910. DOI: [10.1002/art.27438](https://doi.org/10.1002/art.27438).

-
- [J6] Balázs Győrffy, Zsombor Benke, András Lánczky, Bálint Balázs, Zoltán Szállási, József Timár, and Reinhold Schäfer. “RecurrenceOnline: an online analysis tool to determine breast cancer recurrence and hormone receptor status using microarray data”. *Breast Cancer Research and Treatment* (July 2011). DOI: 10.1007/s10549-011-1676-y.
 - [J7] Weiwei Shi, Balint Balazs, Balazs Györffy, Tingting Jiang, W. Fraser Symmans, Christos Hatzis, and Lajos Pusztai. “Combined analysis of gene expression, DNA copy number, and mutation profiling data to display biological process anomalies in individual breast cancers”. *Breast Cancer Research and Treatment* 144.3 (Mar. 2014), pp. 561–568. DOI: 10.1007/s10549-014-2904-z.

The author’s conference presentations

- [C1] Bálint Balázs, Marvin Albert, and Lars Hufnagel. “GPU-based image processing for multiview microscopy data”. *Light Sheet Fluorescence Microscopy International Conference*. Sheffield, UK, Sept. 2016 (cit. on p. 91).
- [C2] Bálint Balázs, Marvin Albert, and Lars Hufnagel. “GPU-based image processing for multi-view microscopy data”. *Focus on Microscopy*. Taipei, Taiwan, Mar. 2016 (cit. on p. 91).
- [C3] Bálint Balázs, Marvin Albert, and Lars Hufnagel. “GPU-based image processing for multi-view microscopy data”. *Focus on Microscopy*. Bordeaux, France, Apr. 2017 (cit. on p. 91).

References cited in the thesis

- [1] Robert Hooke. *Micrographia: or Some Physiological Descriptions of Minute Bodies Made by Magnifying Glasses. With Observations and Inquiries Thereupon*. London: J. Martyn and J. Allestry, 1665 (cit. on p. 1).
- [2] Philipp J Keller and Ernst HK Stelzer. “Quantitative in vivo imaging of entire embryos with Digital Scanned Laser Light Sheet Fluorescence Microscopy”. *Current Opinion in Neurobiology* 18.6 (Dec. 2008). review, pp. 624–632. DOI: 10.1016/j.conb.2009.03.008 (cit. on p. 1).
- [3] Jan Huisken and Didier Y. R. Stainier. “Selective plane illumination microscopy techniques in developmental biology”. *Development* 136.12 (June 2009), pp. 1963–1975. DOI: 10.1242/dev.022426 (cit. on pp. 1, 15).
- [4] Michael Weber and Jan Huisken. “Light sheet microscopy for real-time developmental biology”. *Current Opinion in Genetics & Development* 21.5 (2011), pp. 566–572. DOI: 10.1016/j.gde.2011.09.009 (cit. on p. 1).
- [5] Raju Tomer, Khaled Khairy, and Philipp J Keller. “Shedding light on the system: studying embryonic development with light sheet microscopy”. *Current Opinion in Genetics & Development*. Developmental mechanisms, patterning and evolution 21.5 (Oct. 2011). Review from 2011, pp. 558–565. DOI: 10.1016/j.gde.2011.07.003 (cit. on p. 1).
- [6] Hans-Ulrich Dodt, Ulrich Leischner, Anja Schierloh, Nina Jährling, Christoph Peter Mauch, Katrin Deininger, Jan Michael Deussing, Matthias Eder, Walter Ziegglänsberger, and Klaus Becker. “Ultramicroscopy: three-dimensional visualization of neuronal networks in the whole mouse brain”. *Nature Methods* 4.4 (Mar. 2007), pp. 331–336. DOI: 10.1038/nmeth1036 (cit. on pp. 1, 15, 26).
- [7] Bi-Chang Chen et al. “Lattice light-sheet microscopy: Imaging molecules to embryos at high spatiotemporal resolution”. *Science* 346.6208 (Oct. 2014), p. 1257998. DOI: 10.1126/science.1257998 (cit. on pp. 1, 16, 63, 65).
- [8] P. Philippe Laissie, Rana A. Alghamdi, Pavel Tomancak, Emmanuel G. Reynaud, and Hari Shroff. “Assessing phototoxicity in live fluorescence imaging”. *Nature Methods* 14.7 (July 2017), pp. 657–661. DOI: 10.1038/nmeth.4344 (cit. on pp. 3, 4, 40).
- [9] Jeff W. Lichtman and José-Angel Conchello. “Fluorescence microscopy”. *Nature Methods* 2.12 (Dec. 2005), pp. 910–919. DOI: 10.1038/nmeth817 (cit. on p. 3).
- [10] Alberto Diaspro. *Optical Fluorescence Microscopy: From the Spectral to the Nano Dimension*. 1st ed. Springer-Verlag Berlin Heidelberg, 2011 (cit. on p. 3).
- [11] G. G. Stokes. “On the Change of Refrangi-bility of Light”. *Philosophical Transactions of the Royal Society of London* 142 (Jan. 1852), pp. 463–562. DOI: 10.1098/rstl.1852.0022 (cit. on p. 3).
- [12] *Spectra Viewer*. URL: <https://www.chroma.com/spectra-viewer> (visited on 09/11/2017) (cit. on p. 4).
- [13] Robert Bacallao, Morgane Bomsel, Ernst H. K. Stelzer, and Jan De Mey. “Guiding Principles of Specimen Preservation for Confocal Fluorescence Microscopy”. *Handbook of Biological Confocal Microscopy*. DOI: 10.1007/978-1-4615-7133-9_18. Springer, Boston, MA, 1990, pp. 197–205 (cit. on p. 5).
- [14] O. Shimomura, F. H. Johnson, and Y. Saiga. “Extraction, purification and properties of ae-quorin, a bioluminescent protein from the lu-minous hydromedusan, Aequorea”. *Journal of Cellular and Comparative Physiology* 59 (June 1962). first purification of GFP from jellyfish, pp. 223–239 (cit. on p. 5).
- [15] Douglas C. Prasher, Virginia K. Eckenrode, William W. Ward, Frank G. Prendergast, and Milton J. Cormier. “Primary structure of the Aequorea victoria green-fluorescent protein”. *Gene* 111.2 (Feb. 1992). cloning GFP cDNA, pp. 229–233. DOI: 10.1016/0378-1119(92)90691-H (cit. on p. 5).
- [16] M. Chalfie, Y. Tu, G. Euskirchen, W. W. Ward, and D. C. Prasher. “Green fluorescent protein as a marker for gene expression”. *Science* 263.5148 (Feb. 1994). GFP in *c. elegans* / nematodes, pp. 802–805. DOI: 10.1126/science.8303295 (cit. on p. 5).
- [17] Adam Amsterdam, Shuo Lin, and Nancy Hopkins. “The Aequorea victoria Green Fluorescent Protein Can Be Used as a Reporter in Live Zebrafish Embryos”. *Developmental Biology* 171.1 (Sept. 1995). first GFP zebrafish, pp. 123–129. DOI: 10.1006/dbio.1995.1265 (cit. on p. 5).

- [18] Masaru Okabe, Masahito Ikawa, Katsuya Kominami, Tomoko Nakanishi, and Yoshitake Nishimune. “‘Green mice’ as a source of ubiquitous green cells”. *FEBS Letters* 407.3 (May 1997), first EGFP mouse, pp. 313–319. doi: 10.1016/S0014-5793(97)00313-X (cit. on p. 5).
- [19] R Heim, D C Prasher, and R Y Tsien. “Wavelength mutations and posttranslational autoxidation of green fluorescent protein.” *Proceedings of the National Academy of Sciences of the United States of America* 91.26 (Dec. 1994), pp. 12501–12504 (cit. on p. 5).
- [20] Roger Heim and Roger Y Tsien. “Engineering green fluorescent protein for improved brightness, longer wavelengths and fluorescence resonance energy transfer”. *Current Biology* 6.2 (Feb. 1996), pp. 178–182. doi: 10.1016/S0960-9822(02)00450-5 (cit. on p. 5).
- [21] Brendan P. Cormack, Raphael H. Valdivia, and Stanley Falkow. “FACS-optimized mutants of the green fluorescent protein (GFP)”. *Gene. Flourescent Proteins and Applications* 173.1 (1996), pp. 33–38. doi: 10.1016/0378-1119(95)00685-0 (cit. on p. 5).
- [22] Robert F. Service. “Three Scientists Bask in Prize’s Fluorescent Glow”. *Science* 322.5900 (Oct. 2008), pp. 361–361. doi: 10.1126/science.322.5900.361 (cit. on p. 5).
- [23] E. Abbe. “Beiträge zur Theorie des Mikroskops und der mikroskopischen Wahrnehmung”. *Archiv für mikroskopische Anatomie* 9.1 (1873), pp. 413–418. doi: 10.1007/BF02956173 (cit. on p. 7).
- [24] Max Born and Emil Wolf. *Principles of Optics: Electromagnetic Theory of Propagation, Interference and Diffraction of Light*. Elsevier, June 2013 (cit. on pp. 8, 9, 63).
- [25] C. J. R. Sheppard and H. J. Matthews. “Imaging in high-aperture optical systems”. *JOSA A* 4.8 (Aug. 1987), pp. 1354–1360. doi: 10.1364/JOSAA.4.001354 (cit. on p. 8).
- [26] Lord Rayleigh F.R.S. “XXXI. Investigations in optics, with special reference to the spectroscope”. *Philosophical Magazine* 8.49 (Oct. 1879), pp. 261–274. doi: 10.1080/14786447908639684 (cit. on p. 9).
- [27] Jim Swoger, Jan Huisken, and Ernst H. K. Stelzer. “Multiple imaging axis microscopy improves resolution for thick-sample applications”. *Optics Letters* 28.18 (Sept. 2003), p. 1654. doi: 10.1364/OL.28.001654 (cit. on p. 11).
- [28] Jim Swoger, Peter Verveer, Klaus Greger, Jan Huisken, and Ernst H. K. Stelzer. “Multi-view image fusion improves resolution in three-dimensional microscopy”. *Optics Express* 15.13 (2007), p. 8029. doi: 10.1364/OE.15.008029 (cit. on pp. 11, 39).
- [29] Marvin Minsky. “Microscopy apparatus”. US3013467 A. U.S. Classification 356/432, 359/389, 348/79, 250/215; International Classification G02B21/00; Cooperative Classification G02B21/0024, G02B21/002; European Classification G02B21/00M4A, G02B21/00M4. Dec. 1961 (cit. on p. 11).
- [30] Paul Davidovits and M. David Egger. “Scanning Laser Microscope”. *Nature* 223.5208 (Aug. 1969), pp. 831–831. doi: 10.1038/223831a0 (cit. on p. 11).
- [31] Ernst H.K. Stelzer and Steffen Lindek. “Fundamental reduction of the observation volume in far-field light microscopy by detection orthogonal to the illumination axis: confocal theta microscopy”. *Optics Communications* 111.5–6 (Oct. 1994), pp. 536–547. doi: 10.1016/0030-4018(94)90533-9 (cit. on p. 13).
- [60] Ralph Gräf, Jens Rietdorf, and Timo Zimmermann. “Live Cell Spinning Disk Microscopy”. *Microscopy Techniques. Advances in Biochemical Engineering*. DOI: 10.1007/b102210. Springer, Berlin, Heidelberg, 2005, pp. 57–75 (cit. on pp. 14, 22).
- [62] G. S. Kino. “Intermediate Optics in Nipkow Disk Microscopes”. *Handbook of Biological Confocal Microscopy*. DOI: 10.1007/978-1-4615-7133-9_10. Springer, Boston, MA, 1990, pp. 105–111 (cit. on p. 14).
- [63] Akihiko Nakano. “Spinning-disk Confocal Microscopy — A Cutting-Edge Tool for Imaging of Membrane Traffic”. *Cell Structure and Function* 27.5 (2002), pp. 349–355. doi: 10.1247/csf.27.349 (cit. on p. 14).
- [36] H. Siedentopf and R. Zsigmondy. “Über Sichtbarmachung und Größenbestimmung ultramikroskopischer Teilchen, mit besonderer Anwendung auf Goldrubingläser”. *Annalen der*

- Physik* 315.1 (1902), pp. 1–39. doi: 10.1002/andp.19023150102 (cit. on p. 15).
- [37] A H Voie, D H Burns, and F A Spelman. “Orthogonal-plane fluorescence optical sectioning: three-dimensional imaging of macroscopic biological specimens”. *Journal of Microscopy* 170.Pt 3 (June 1993), pp. 229–36. doi: 8371260 (cit. on p. 15).
- [38] Arne H. Voie and Francis A. Spelman. “Three-dimensional reconstruction of the cochlea from two-dimensional images of optical sections”. *Computerized Medical Imaging and Graphics* 19.5 (Sept. 1995), pp. 377–384. doi: 10.1016/0895-6111(95)00034-8 (cit. on p. 15).
- [39] Eran Fuchs, Jules S. Jaffe, Richard A. Long, and Farooq Azam. “Thin laser light sheet microscope for microbial oceanography”. *Optics Express* 10.2 (Jan. 2002), pp. 145–154. doi: 10.1364/OE.10.000145 (cit. on p. 15).
- [40] Jan Huisken, Jim Swoger, Filippo Del Bene, Joachim Wittbrodt, and Ernst H. K Stelzer. “Optical Sectioning Deep Inside Live Embryos by Selective Plane Illumination Microscopy”. *Science* 305.5686 (2004), pp. 1007–1009 (cit. on pp. 15, 16, 18).
- [41] Jérémie Capoulade, Malte Wachsmuth, Lars Hufnagel, and Michael Knop. “Quantitative fluorescence imaging of protein diffusion and interaction in living cells”. *Nature Biotechnology* 29.9 (Sept. 2011), pp. 835–839. doi: 10.1038/nbt.1928 (cit. on p. 16).
- [42] Yicong Wu, Alireza Ghitani, Ryan Christensen, Anthony Santella, Zhuo Du, Gary Rondeau, Zhirong Bao, Daniel Colón-Ramos, and Hari Shroff. “Inverted selective plane illumination microscopy (iSPIM) enables coupled cell identity lineage and neurodevelopmental imaging in *Caenorhabditis elegans*”. *Proceedings of the National Academy of Sciences* 108.43 (Oct. 2011). iSPIM, tracking c. elegans nuclei, pp. 17708–17713. doi: 10.1073/pnas.1108494108 (cit. on pp. 15, 16).
- [43] Yicong Wu et al. “Spatially isotropic four-dimensional imaging with dual-view plane illumination microscopy”. *Nature Biotechnology* 31.11 (Nov. 2013), pp. 1032–1038. doi: 10.1038/nbt.2713 (cit. on pp. 16, 39).
- [44] Jan Huisken and Didier Y. R. Stainier. “Even fluorescence excitation by multidirectional selective plane illumination microscopy (mSPIM)”. *Optics Letters* 32.17 (2007), pp. 2608–2610. doi: 10.1364/OL.32.002608 (cit. on pp. 16, 20).
- [45] Uros Krzic, Stefan Gunther, Timothy E. Saunders, Sebastian J. Streichan, and Lars Hufnagel. “Multiview light-sheet microscope for rapid *in toto* imaging”. *Nature Methods* 9.7 (July 2012). MuVi-SPIM, pp. 730–733. doi: 10.1038/nmeth.2064 (cit. on pp. 16, 66–68, 73, 83, 84, 86).
- [46] Raju Tomer, Khaled Khairy, Fernando Amat, and Philipp J. Keller. “Quantitative high-speed imaging of entire developing embryos with simultaneous multiview light-sheet microscopy”. *Nature Methods* 9.7 (July 2012). SimView, pp. 755–763. doi: 10.1038/nmeth.2062 (cit. on p. 16).
- [47] Benjamin Schmid, Gopi Shah, Nico Scherf, Michael Weber, Konstantin Thierbach, Citlali Pérez Campos, Ingo Roeder, Pia Aanstad, and Jan Huisken. “High-speed panoramic light-sheet microscopy reveals global endodermal cell dynamics”. *Nature Communications* 4 (July 2013). zebrafish sphere projection + FEP tube. doi: 10.1038/ncomms3207 (cit. on p. 16).
- [48] Raghav K. Chhetri, Fernando Amat, Yinan Wan, Burkhard Höckendorf, William C. Lemon, and Philipp J. Keller. “Whole-animal functional and developmental imaging with isotropic spatial resolution”. *Nature Methods* 12.12 (Dec. 2015), pp. 1171–1178. doi: 10.1038/nmeth.3632 (cit. on p. 16).
- [49] Philipp J. Keller, Annette D. Schmidt, Joachim Wittbrodt, and Ernst H. K. Stelzer. “Reconstruction of Zebrafish Early Embryonic Development by Scanned Light Sheet Microscopy”. *Science* 322.5904 (Nov. 2008), pp. 1065–1069. doi: 10.1126/science.1162493 (cit. on pp. 15, 18, 20, 68).
- [50] Takehiko Ichikawa, Kenichi Nakazato, Philipp J. Keller, Hiroko Kajiura-Kobayashi, Ernst H. K. Stelzer, Atsushi Mochizuki, and Shigenori Nonaka. “Live Imaging of Whole Mouse Embryos during Gastrulation: Migration Analyses of Epiblast and Mesodermal Cells”. *PLoS ONE* 8.7 (July 2013). post implantation, e64506. doi: 10.1371/journal.pone.0064506 (cit. on pp. 15, 25).
- [51] Ryan S. Udan, Victor G. Piazza, Chih-wei Hsu, Anna-Katerina Hadjantonakis, and Mary E. Dickinson. “Quantitative imaging of cell dynamics in mouse embryos using light-sheet microscopy”. *Development* (Oct. 2014). post im-

References cited in the thesis

- plantation, dev.111021. DOI: 10 . 1242 / dev . 111021 (cit. on pp. 15, 25).
- [52] Abhishek Kumar et al. “Dual-view plane illumination microscopy for rapid and spatially isotropic imaging”. *Nature Protocols* 9.11 (Nov. 2014). diSPIM, pp. 2555–2573. DOI: 10 . 1038 / nprot . 2014 . 172 (cit. on p. 16).
- [53] Francesca Cella Zanacchi, Zeno Lavagnino, Michela Perrone Donnorso, Alessio Del Bue, Laura Furia, Mario Faretta, and Alberto Diaspro. “Live-cell 3D super-resolution imaging in thick biological samples”. *Nature Methods* 8.12 (Dec. 2011), pp. 1047–1049. DOI: 10 . 1038 / nmeth . 1744 (cit. on p. 16).
- [54] Mike Friedrich, Qiang Gan, Vladimir Ermolayev, and Gregory S. Harms. “STED-SPIM: Stimulated Emission Depletion Improves Sheet Illumination Microscopy Resolution”. *Biophysical Journal* 100.8 (Apr. 2011), pp. L43–L45. DOI: 10 . 1016 / j . bpj . 2010 . 12 . 3748 (cit. on p. 16).
- [55] Philipp J. Keller, Annette D. Schmidt, Anthony Santella, Khaled Khairy, Zhirong Bao, Joachim Wittbrodt, and Ernst H. K. Stelzer. “Fast, high-contrast imaging of animal development with scanned light sheet-based structured-illumination microscopy”. *Nature Methods* 7.8 (Aug. 2010), pp. 637–642. DOI: 10 . 1038 / nmeth . 1476 (cit. on pp. 16, 64).
- [56] Bo-Jui Chang, Victor Didier Perez Meza, and Ernst H. K. Stelzer. “csiLSFM combines light-sheet fluorescence microscopy and coherent structured illumination for a lateral resolution below 100 nm”. *Proceedings of the National Academy of Sciences* 114.19 (May 2017), pp. 4869–4874. DOI: 10 . 1073 / pnas . 1609278114 (cit. on pp. 16, 64).
- [57] K. Greger, J. Swoger, and E. H. K. Stelzer. “Basic building units and properties of a fluorescence single plane illumination microscope”. *Review of Scientific Instruments* 78.2 (Feb. 2007), pp. 023705–023705–7. DOI: doi : 10 . 1063 / 1 . 2428277 (cit. on p. 18).
- [58] Bahaa E. A. Saleh and Malvin Carl Teich. *Fundamentals of Photonics*. John Wiley & Sons, Mar. 2007 (cit. on p. 18).
- [67] Sonja Nowotschin, Anna Ferrer-Vaquer, and Anna-Katerina Hadjantonakis. “Chapter 20 - Imaging Mouse Development with Confocal Time-Lapse Microscopy”. *Methods in Enzymology*. Ed. by Paul M. Wassarman and Philippe M. Soriano. Vol. 476. Guide to Techniques in Mouse Development, Part A: Mice, Embryos, and Cells, 2nd Edition. Academic Press, 2010, pp. 351–377 (cit. on p. 22).
- [59] David M. Shotton. “Confocal scanning optical microscopy and its applications for biological specimens”. *Journal of Cell Science* 94.2 (Oct. 1989), pp. 175–206 (cit. on p. 22).
- [61] James Jonkman and Claire M. Brown. “Any Way You Slice It—A Comparison of Confocal Microscopy Techniques”. *Journal of Biomolecular Techniques : JBT* 26.2 (July 2015), pp. 54–65. DOI: 10 . 7171 / jbt . 15 - 2602 - 003 (cit. on p. 22).
- [32] Silvia Aldaz, Luis M. Escudero, and Matthew Freeman. “Live Imaging of Drosophila Imaginal Disc Development”. *Proceedings of the National Academy of Sciences* 107.32 (Aug. 2010), pp. 14217–14222. DOI: 10 . 1073 / pnas . 1008623107 (cit. on p. 22).
- [33] Jean-Léon Maître, Hervé Turlier, Rukshala Illukkumbura, Björn Eismann, Ritsuya Niwayama, François Nédélec, and Takashi Hiriragi. “Asymmetric division of contractile domains couples cell positioning and fate specification”. *Nature* 536.7616 (Aug. 2016), pp. 344–348. DOI: 10 . 1038 / nature18958 (cit. on p. 22).
- [34] Emmanuel G. Reynaud, Uroš Kržič, Klaus Greger, and Ernst H.K. Stelzer. “Light sheet-based fluorescence microscopy: more dimensions, more photons, and less photodamage”. *HFSP Journal* 2.5 (Oct. 2008), pp. 266–275. DOI: 10 . 2976 / 1 . 2974980 (cit. on p. 22).
- [35] Stelzer. “Contrast, resolution, pixelation, dynamic range and signal-to-noise ratio: fundamental limits to resolution in fluorescence light microscopy”. *Journal of Microscopy* 189.1 (Jan. 1998). This is also the reason why it is sufficient to store the square root of the count rate. That number will contain all the available information., pp. 15–24. DOI: 10 . 1046 / j . 1365 - 2818 . 1998 . 00290 . x (cit. on p. 22).
- [69] Adam S. Doherty and Richard M. Schultz. “Culture of Preimplantation Mouse Embryos”. *Developmental Biology Protocols*. Methods in Molecular Biology™. DOI: 10 . 1385 / 1 - 59259 - 685 - 1 : 47. Humana Press, 2000, pp. 47–52 (cit. on p. 23).

- [70] Jens-Erik Dietrich and Takashi Hiiragi. “Stochastic patterning in the mouse pre-implantation embryo”. *Development* 134.23 (Dec. 2007), pp. 4219–4231. doi: 10.1242/dev.003798 (cit. on p. 23).
- [71] W. Denk, J. H. Strickler, and W. W. Webb. “Two-photon laser scanning fluorescence microscopy”. *Science* 248.4951 (Apr. 1990), pp. 73–76. doi: 10.1126/science.2321027 (cit. on p. 23).
- [72] Jayne M. Squirrell, David L. Wokosin, John G. White, and Barry D. Bavister. “Long-term two-photon fluorescence imaging of mammalian embryos without compromising viability”. *Nature Biotechnology* 17.8 (Aug. 1999). low damage live-cell imaging with two-photon caser scanning hamster, pp. 763–767. doi: 10.1038/11698 (cit. on p. 23).
- [73] Katie McDole, Yuan Xiong, Pablo A. Iglesias, and Yixian Zheng. “Lineage mapping the pre-implantation mouse embryo by two-photon microscopy, new insights into the segregation of cell fates”. *Developmental Biology* 355.2 (July 2011), pp. 239–249. doi: 10.1016/j.ydbio.2011.04.024 (cit. on p. 23).
- [74] Kazuo Yamagata, Rinako Suetsugu, and Teruhiko Wakayama. “Long-Term, Six-Dimensional Live-Cell Imaging for the Mouse Preimplantation Embryo That Does Not Affect Full-Term Development”. *Journal of Reproduction and Development* 55.3 (2009), pp. 343–350. doi: 10.1262/jrd.20166 (cit. on p. 23).
- [75] Gustavo de Medeiros, Nils Norlin, Stefan Gunther, Marvin Albert, Laura Panavaite, Ulla-Maj Fiuba, Francesca Peri, Takashi Hiiragi, Uros Krzic, and Lars Hufnagel. “Confocal multiview light-sheet microscopy”. *Nature Communications* 6 (Nov. 2015), p. 8881. doi: 10.1038/ncomms9881 (cit. on pp. 25, 26, 68, 70, 78, 86).
- [76] Laura Panavaite, Balint Balazs, Tristan Rodriguez, Shankar Srinivas, Jerome Collignon, Lars Hufnagel, and Takashi Hiiragi. “3D-geec: a method for studying mouse peri-implantation development”. *Mechanisms of Development*. 18th International Congress of Developmental Biology 18-22 June, University Cultural Centre, National University of Singapore 145. Supplement (July 2017), S78–S79. doi: 10.1016/j.mod.2017.04.189 (cit. on p. 24).
- [77] Yu-Chih Hsu. “In vitro development of individually cultured whole mouse embryos from blastocyst to early somite stage”. *Developmental Biology* 68.2 (Feb. 1979). post-implantation culture, pp. 453–461. doi: 10.1016/0012-1606(79)90217-3 (cit. on p. 24).
- [78] Fu-Jen Huang, Tsung-Chieh J. Wu, and Meng-Yin Tsai. “Effect of retinoic acid on implantation and post-implantation development of mouse embryos in vitro”. *Human Reproduction* 16.10 (Oct. 2001). post-implantation culture, pp. 2171–2176. doi: 10.1093/humrep/16.10.2171 (cit. on p. 24).
- [79] Sonja Nowotschin and Anna-Katerina Hadjantonakis. “Cellular dynamics in the early mouse embryo: from axis formation to gastrulation”. *Current Opinion in Genetics & Development*. Developmental mechanisms, patterning and evolution 20.4 (Aug. 2010), pp. 420–427. doi: 10.1016/j.gde.2010.05.008 (cit. on p. 24).
- [80] Monica D. Garcia, Ryan S. Udan, Anna-Katerina Hadjantonakis, and Mary E. Dickinson. “Live Imaging of Mouse Embryos”. *Cold Spring Harbor Protocols* 2011.4 (Apr. 2011), pdb.top104. doi: 10.1101/pdb.top104 (cit. on p. 24).
- [81] Alessandro Bria and Giulio Iannello. “TeraStitcher - A tool for fast automatic 3D-stitching of teravoxel-sized microscopy images”. *BMC Bioinformatics* 13 (Nov. 2012), p. 316. doi: 10.1186/1471-2105-13-316 (cit. on p. 27).
- [82] Gergely Katona, Gergely Szalay, Pál Maák, Attila Kaszás, Máté Veress, Dániel Hillier, Balázs Chiovini, E. Sylvester Vizi, Botond Roska, and Balázs Rózsa. “Fast two-photon in vivo imaging with three-dimensional random-access scanning in large tissue volumes”. *Nature Methods* 9.2 (Feb. 2012), pp. 201–208. doi: 10.1038/nmeth.1851 (cit. on p. 27).
- [83] Hiroshi Hama, Hiroshi Kurokawa, Hiroyuki Kawano, Ryoko Ando, Tomomi Shimogori, Hisayori Noda, Kiyoko Fukami, Asako Sakae-Sawano, and Atsushi Miyawaki. “Scale: a chemical approach for fluorescence imaging and reconstruction of transparent mouse brain”. *Nature Neuroscience* 14.11 (Nov. 2011), pp. 1481–1488. doi: 10.1038/nn.2928 (cit. on p. 27).

- [84] Ali Ertürk, Klaus Becker, Nina Jährling, Christoph P. Mauch, Caroline D. Hojer, Jackson G. Egen, Farida Hellal, Frank Bradke, Morgan Sheng, and Hans-Ulrich Dodt. “Three-dimensional imaging of solvent-cleared organs using 3DISCO”. *Nature Protocols* 7.11 (Nov. 2012), pp. 1983–1995. doi: 10.1038/nprot.2012.119 (cit. on p. 27).
- [85] Ali Ertürk et al. “Three-dimensional imaging of the unsectioned adult spinal cord to assess axon regeneration and glial responses after injury”. *Nature Medicine* 18.1 (Jan. 2012), pp. 166–171. doi: 10.1038/nm.2600 (cit. on p. 27).
- [86] Meng-Tsen Ke, Satoshi Fujimoto, and Takeshi Imai. “SeeDB: a simple and morphology-preserving optical clearing agent for neuronal circuit reconstruction”. *Nature Neuroscience* 16.8 (Aug. 2013), pp. 1154–1161. doi: 10.1038/nn.3447 (cit. on p. 27).
- [87] Kwanghun Chung and Karl Deisseroth. “CLARITY for mapping the nervous system”. *Nature Methods* 10.6 (June 2013), pp. 508–513. doi: 10.1038/nmeth.2481 (cit. on p. 27).
- [88] Etsuo A. Susaki et al. “Whole-Brain Imaging with Single-Cell Resolution Using Chemical Cocktails and Computational Analysis”. *Cell* 157.3 (Apr. 2014), pp. 726–739. doi: 10.1016/j.cell.2014.03.042 (cit. on p. 27).
- [89] Nicolas Renier, Zhuhao Wu, David J. Simon, Jing Yang, Pablo Ariel, and Marc Tessier-Lavigne. “iDISCO: A Simple, Rapid Method to Immunolabel Large Tissue Samples for Volume Imaging”. *Cell* 159.4 (Nov. 2014), pp. 896–910. doi: 10.1016/j.cell.2014.10.010 (cit. on p. 27).
- [90] Kazuki Tainaka, Shimpei I. Kubota, Takeru Q. Suyama, Etsuo A. Susaki, Dimitri Perrin, Maki Ukai-Tadenuma, Hideki Ukai, and Hiroki R. Ueda. “Whole-Body Imaging with Single-Cell Resolution by Tissue Decolorization”. *Cell* 159.4 (Nov. 2014), pp. 911–924. doi: 10.1016/j.cell.2014.10.034 (cit. on p. 27).
- [91] Tongcang Li, Sadao Ota, Jeongmin Kim, Zi Jing Wong, Yuan Wang, Xiaobo Yin, and Xiang Zhang. “Axial Plane Optical Microscopy”. *Scientific Reports* 4 (Dec. 2014). doi: 10.1038/srep07253 (cit. on p. 27).
- [92] Matthew B. Bouchard, Venkatakaushik Voluti, César S. Mendes, Clay Lacefield, Wesley B. Grueber, Richard S. Mann, Randy M. Bruno, and Elizabeth M. C. Hillman. “Swept confocally-aligned planar excitation (SCAPE) microscopy for high-speed volumetric imaging of behaving organisms”. *Nature Photonics* 9.2 (Feb. 2015), pp. 113–119. doi: 10.1038/nphoton.2014.323 (cit. on p. 27).
- [93] Khalid Sayood. *Introduction to Data Compression, Fourth Edition*. 4th ed. The Morgan Kaufmann Series in Multimedia Information and Systems. Morgan Kaufmann, 2012 (cit. on pp. 29, 34).
- [94] David Salomon and Giovanni Motta. *Handbook of Data Compression*. 5th. Google-Books-ID: LHCY4VbiFqAC. Springer Science & Business Media, Jan. 2010 (cit. on pp. 29, 32).
- [95] Douglas W. Cromey. “Digital Images Are Data: And Should Be Treated as Such”. *Methods in molecular biology (Clifton, N.J.)* 931 (2013), pp. 1–27. doi: 10.1007/978-1-62703-056-4_1 (cit. on pp. 29, 76).
- [96] Claude E. Shannon. “A mathematical theory of communication”. *The Bell System Technical Journal* 27.4 (Oct. 1948), pp. 623–656. doi: 10.1002/j.1538-7305.1948.tb00917.x (cit. on pp. 29, 30).
- [97] Claude E. Shannon. “A mathematical theory of communication”. *The Bell System Technical Journal* 27.3 (July 1948), pp. 379–423. doi: 10.1002/j.1538-7305.1948.tb01338.x (cit. on p. 29).
- [98] Claude E. Shannon. “Prediction and entropy of printed English”. *Bell Labs Technical Journal* 30.1 (1951), pp. 50–64 (cit. on p. 29).
- [99] J. Rissanen and G. Langdon. “Universal modeling and coding”. *IEEE Transactions on Information Theory* 27.1 (Jan. 1981), pp. 12–23. doi: 10.1109/TIT.1981.1056282 (cit. on p. 30).
- [100] David A. Huffman. “A Method for the Construction of Minimum-Redundancy Codes”. *Proceedings of the IRE* 40.9 (Sept. 1952), pp. 1098–1101. doi: 10.1109/JRPROC.1952.273898 (cit. on p. 31).
- [101] N. Ahmed, T. Natarajan, and K. R. Rao. “Discrete Cosine Transform”. *IEEE Transactions on Computers* C-23.1 (Jan. 1974), pp. 90–93. doi: 10.1109/T-C.1974.223784 (cit. on p. 35).

- [102] Stephane G. Mallat. “A theory for multiresolution signal decomposition : the wavelet representation”. *IEEE Transaction on Pattern Analysis and Machine Intelligence* (1989) (cit. on p. 35).
- [103] Arne Jensen and Anders la Cour-Harbo. *Ripples in Mathematics*. DOI: 10.1007/978-3-642-56702-5. Berlin, Heidelberg: Springer Berlin Heidelberg, 2001 (cit. on p. 35).
- [104] William B. Pennebaker and Joan L. Mitchell. *JPEG: Still Image Data Compression Standard*. Springer Science & Business Media, Dec. 1992 (cit. on pp. 36, 37, 77).
- [105] M.J. Weinberger, G. Seroussi, and G. Sapiro. “The LOCO-I lossless image compression algorithm: principles and standardization into JPEG-LS”. *IEEE Transactions on Image Processing* 9.8 (Aug. 2000), pp. 1309–1324. doi: 10.1109/83.855427 (cit. on pp. 36, 37, 77, 79).
- [106] X. Wu and N. Memon. “Context-based, adaptive, lossless image coding”. *IEEE Transactions on Communications* 45.4 (Apr. 1997), pp. 437–444. doi: 10.1109/26.585919 (cit. on p. 36).
- [107] Roman Starosolski. “Simple fast and adaptive lossless image compression algorithm”. *Software: Practice and Experience* 37.1 (Jan. 2007), pp. 65–91. doi: 10.1002/spe.746 (cit. on pp. 36, 77).
- [108] Z. Wang, M. Klaiber, Y. Gera, S. Simon, and T. Richter. “Fast lossless image compression with 2D Golomb parameter adaptation based on JPEG-LS”. *Signal Processing Conference (EUSIPCO), 2012 Proceedings of the 20th European*. Aug. 2012, pp. 1920–1924 (cit. on pp. 36, 77).
- [109] Nazeeh Aranki, Didier Keymeulen, Alireza Bakhshi, and Matthew Klimesh. “Hardware Implementation of Lossless Adaptive and Scalable Hyperspectral Data Compression for Space”. *Proceedings of the 2009 NASA/ESA Conference on Adaptive Hardware and Systems*. AHS ’09. Washington, DC, USA: IEEE Computer Society, 2009, pp. 315–322. doi: 10.1109/AHS.2009.66 (cit. on p. 36).
- [110] Scott F. Gilbert. *Developmental Biology*. 10th. Sinauer Associates, 2013 (cit. on p. 38).
- [111] M. Temerinac-Ott, O. Ronneberger, P. Ochs, W. Driever, T. Brox, and H. Burkhardt. “Multiview Deblurring for 3-D Images from Light-Sheet-Based Fluorescence Microscopy”. *IEEE Transactions on Image Processing* 21.4 (Apr. 2012), pp. 1863–1873. doi: 10.1109/TIP.2011.2181528 (cit. on p. 39).
- [112] Stephan Preibisch, Fernando Amat, Evangelia Stamatakis, Mihail Sarov, Robert H. Singer, Eugene Myers, and Pavel Tomancak. “Efficient Bayesian-based multiview deconvolution”. *Nature Methods* 11.6 (June 2014), pp. 645–648. doi: 10.1038/nmeth.2929 (cit. on pp. 39, 61, 63).
- [113] Bálint Balázs. “Development of a symmetric single-plane illumination microscope”. Master’s Thesis. Hungary: Pázmány Péter Catholic University, 2013 (cit. on pp. 39, 51).
- [114] Sarah Frisken Gibson and Frederick Lanni. “Experimental test of an analytical model of aberration in an oil-immersion objective lens used in three-dimensional light microscopy”. *JOSA A* 9.1 (Jan. 1992), pp. 154–166. doi: 10.1364/JOSAA.9.000154 (cit. on p. 58).
- [115] Jizhou Li, Feng Xue, and Thierry Blu. “Fast and accurate three-dimensional point spread function computation for fluorescence microscopy”. *JOSA A* 34.6 (June 2017), pp. 1029–1034. doi: 10.1364/JOSAA.34.001029 (cit. on p. 58).
- [116] Johannes Schindelin et al. “Fiji: an open-source platform for biological-image analysis”. *Nature Methods* 9.7 (July 2012), pp. 676–682. doi: 10.1038/nmeth.2019 (cit. on pp. 59, 63, 84).
- [117] Janick Cardinale. *An ImageJ Plugin to Measure 3D Point Spread Functions*. 2010. URL: http://mosaic.mpi-cbg.de/Downloads/PSF_measurement_3D.pdf (visited on 10/04/2017) (cit. on p. 59).
- [118] Daniel Sage, Lauréne Donati, Ferréol Soulez, Denis Fortun, Guillaume Schmit, Arne Seitz, Romain Guiet, Cédric Vonesch, and Michael Unser. “DeconvolutionLab2: An open-source software for deconvolution microscopy”. *Methods. Image Processing for Biologists* 115 (Feb. 2017), pp. 28–41. doi: 10.1016/j.ymeth.2016.12.015 (cit. on p. 59).
- [119] Pierre Gönczy. “Towards a molecular architecture of centriole assembly”. *Nature Reviews Molecular Cell Biology* 13 (2012). doi: 10.1038/nrm3373 (cit. on p. 60).

- [120] Stephan Preibisch, Stephan Saalfeld, Johannes Schindelin, and Pavel Tomancak. “Software for bead-based registration of selective plane illumination microscopy data”. *Nature Methods* 7.6 (June 2010), pp. 418–419. DOI: 10.1038/nmeth0610-418 (cit. on pp. 63, 69).
- [121] H. Kirshner, D. Sage, and M. Unser. “3D PSF Models for Fluorescence Microscopy in ImageJ”. *Proceedings of the Twelfth International Conference on Methods and Applications of Fluorescence Spectroscopy, Imaging and Probes (MAF'11)*. ImageJ PSF generator. Strasbourg, French Republic, Sept. 2011, p. 154 (cit. on p. 63).
- [122] M. Rauzi. “Probing tissue interaction with laser-based cauterization in the early developing *Drosophila* embryo”. *Methods in Cell Biology*. Cell Polarity and Morphogenesis 139 (Jan. 2017), pp. 153–165. DOI: 10.1016/bs.mcb.2016.11.003 (cit. on p. 64).
- [123] Kevin M. Dean, Philippe Roudot, Carlos R. Reis, Erik S. Welf, Marcel Mettlen, and Reto Fiolka. “Diagonally Scanned Light-Sheet Microscopy for Fast Volumetric Imaging of Adherent Cells”. *Biophysical Journal* 110.6 (Mar. 2016), pp. 1456–1465. DOI: 10.1016/j.bpj.2016.01.029 (cit. on p. 64).
- [124] Anne E. Carpenter and David M. Sabatini. “Systematic genome-wide screens of gene function”. *Nature Reviews Genetics* 5.1 (Jan. 2004), pp. 11–22. DOI: 10.1038/nrg1248 (cit. on p. 66).
- [125] Christophe J. Echeverri and Norbert Perrimon. “High-throughput RNAi screening in cultured cells: a user’s guide”. *Nature Reviews Genetics* 7.5 (May 2006), pp. 373–384. DOI: 10.1038/nrg1836 (cit. on p. 66).
- [126] Rainer Pepperkok and Jan Ellenberg. “High-throughput fluorescence microscopy for systems biology”. *Nature Reviews Molecular Cell Biology* 7.9 (Sept. 2006), pp. 690–696. DOI: 10.1038/nrm1979 (cit. on p. 66).
- [127] Eric Betzig, George H. Patterson, Rachid Sougrat, O. Wolf Lindwasser, Scott Olenych, Juan S. Bonifacino, Michael W. Davidson, Jennifer Lippincott-Schwartz, and Harald F. Hess. “Imaging Intracellular Fluorescent Proteins at Nanometer Resolution”. *Science* 313.5793 (Sept. 2006), pp. 1642–1645. DOI: 10.1126/science.1127344 (cit. on p. 66).
- [128] Samuel T. Hess, Thanu P. K. Girirajan, and Michael D. Mason. “Ultra-High Resolution Imaging by Fluorescence Photoactivation Localization Microscopy”. *Biophysical Journal* 91.11 (Dec. 2006), pp. 4258–4272. DOI: 10.1529/biophysj.106.091116 (cit. on p. 66).
- [129] Michael J. Rust, Mark Bates, and Xiaowei Zhuang. “Sub-diffraction-limit imaging by stochastic optical reconstruction microscopy (STORM)”. *Nature Methods* 3.10 (Oct. 2006), pp. 793–796. DOI: 10.1038/nmeth929 (cit. on p. 66).
- [130] Roy Wollman and Nico Stuurman. “High throughput microscopy: from raw images to discoveries”. *Journal of Cell Science* 120.21 (Nov. 2007), pp. 3715–3722. DOI: 10.1242/jcs.013623 (cit. on p. 66).
- [131] Emmanuel G. Reynaud, Jan Peychl, Jan Huisken, and Pavel Tomancak. “Guide to light-sheet microscopy for adventurous biologists”. *Nature Methods* 12.1 (Jan. 2015), pp. 30–34. DOI: 10.1038/nmeth.3222 (cit. on p. 66).
- [132] Jeffrey M. Perkel. “The struggle with image glut”. *Nature* 533.7601 (Apr. 2016), pp. 131–132. DOI: 10.1038/533131a (cit. on p. 66).
- [133] John Nickolls, Ian Buck, Michael Garland, and Kevin Skadron. “Scalable Parallel Programming with CUDA”. *Queue* 6.2 (Mar. 2008), pp. 40–53. DOI: 10.1145/1365490.1365500 (cit. on p. 66).
- [134] Gustavo Q. G. de Medeiros. “Deep tissue light-sheet microscopy”. PhD thesis. Germany: Ruperto-Carola University of Heidelberg, 2016 (cit. on p. 67).
- [135] Eugen Baumgart and Ulrich Kubitscheck. “Scanned light sheet microscopy with confocal slit detection”. *Optics Express* 20.19 (2012), pp. 21805–21814. DOI: 10.1364/OE.20.021805 (cit. on p. 68).
- [136] Uroš Kržič. “Multiple-view microscopy with light-sheet based fluorescence microscope”. PhD thesis. Germany: Ruperto-Carola University of Heidelberg, 2009 (cit. on p. 69).
- [137] Stephan Preibisch, Stephan Saalfeld, Torsten Rohlfing, and Pavel Tomancak. “Bead-based mosaicing of single plane illumination microscopy images using geometric local descriptor matching”. Ed. by Josien P. W. Pluim and Benoit M. Dawant. Feb. 2009, 72592S. DOI: 10.1117/12.812612 (cit. on p. 69).
- [138] The HDF Group. *Hierarchical Data Format, version 5*. 1997 (cit. on p. 72).

- [139] Fernando Amat, Burkhard Höckendorf, Yinan Wan, William C. Lemon, Katie McDole, and Philipp J. Keller. “Efficient processing and analysis of large-scale light-sheet microscopy data”. *Nature Protocols* 10.11 (Nov. 2015), pp. 1679–1696. doi: 10.1038/nprot.2015.111 (cit. on pp. 73, 81).
- [140] G. W. Zack, W. E. Rogers, and S. A. Latt. “Automatic measurement of sister chromatid exchange frequency”. *The Journal of Histochemistry and Cytochemistry: Official Journal of the Histochemistry Society* 25.7 (July 1977), pp. 741–753. doi: 10.1177/25.7.70454 (cit. on p. 73).
- [141] Loïc A. Royer, William C. Lemon, Raghav K. Chhetri, Yinan Wan, Michael Coleman, Eugene W. Myers, and Philipp J. Keller. “Adaptive light-sheet microscopy for long-term, high-resolution imaging in living organisms”. *Nature Biotechnology* 34.12 (Dec. 2016), pp. 1267–1278. doi: 10.1038/nbt.3708 (cit. on p. 75).
- [142] Michael D. Adams. *The JPEG-2000 still image compression standard*. 2001 (cit. on pp. 76, 77).
- [143] International Telecommunications Union. *H.265 : High efficiency video coding*. Dec. 2016. URL: <http://www.itu.int/rec/T-REC-H.265-201612-I/en> (visited on 10/02/2017) (cit. on p. 76).
- [144] *x265 HEVC Encoder / H.265 Video Codec*. URL: <http://x265.org/> (visited on 10/11/2017) (cit. on p. 76).
- [145] Marc Treib, Florian Reichl, Stefan Auer, and Rüdiger Westermann. “Interactive Editing of GigaSample Terrain Fields”. *Computer Graphics Forum* 31.2pt2 (May 2012), pp. 383–392. doi: 10.1111/j.1467-8659.2012.03017.x (cit. on pp. 77, 78).
- [146] M. Treib, K. Burger, F. Reichl, C. Meneveau, A. Szalay, and R. Westermann. “Turbulence Visualization at the Terascale on Desktop PCs”. *IEEE Transactions on Visualization and Computer Graphics* 18.12 (Dec. 2012), pp. 2169–2177. doi: 10.1109/TVCG.2012.274 (cit. on p. 78).
- [147] Robert A. Gowen and Alan Smith. “Square root data compression”. *Review of Scientific Instruments* 74.8 (Aug. 2003), pp. 3853–3861. doi: 10.1063/1.1593811 (cit. on p. 79).
- [148] Gary M. Bernstein, Chris Bebek, Jason Rhodes, Chris Stoughton, R. Ali Vanderveld, and Penshu Yeh. “Noise and bias in square-root compression schemes”. *Publications of the Astronomical Society of the Pacific* 122.889 (Mar. 2010). arXiv: 0910.4571, pp. 336–346. doi: 10.1086/651281 (cit. on p. 79).
- [149] R. M. Gray and D. L. Neuhoff. “Quantization”. *IEEE Transactions on Information Theory* 44.6 (Oct. 1998), pp. 2325–2383. doi: 10.1109/18.720541 (cit. on p. 80).
- [150] C. Sommer, C. Straehle, U. Köthe, and F. A. Hamprecht. “Ilastik: Interactive learning and segmentation toolkit”. *2011 IEEE International Symposium on Biomedical Imaging: From Nano to Macro*. Mar. 2011, pp. 230–233. doi: 10.1109/ISBI.2011.5872394 (cit. on pp. 83, 86).
- [151] Tobias Pietzsch, Stephan Saalfeld, Stephan Preibisch, and Pavel Tomancak. “Big-DataViewer: visualization and processing for large image data sets”. *Nature Methods* 12.6 (June 2015), pp. 481–483. doi: 10.1038/nmeth.3392 (cit. on p. 84).
- [152] Joran Deschamps, Markus Mund, and Jonas Ries. “3D superresolution microscopy by supercritical angle detection”. *Optics Express* 22.23 (Nov. 2014), pp. 29081–29091 (cit. on pp. 86, 87).
- [153] Joran Deschamps, Andreas Rowald, and Jonas Ries. “Efficient homogeneous illumination and optical sectioning for quantitative single-molecule localization microscopy”. *Optics Express* 24.24 (Nov. 2016), pp. 28080–28090. doi: 10.1364/OE.24.028080 (cit. on pp. 86, 87).
- [154] Jeremy C. Simpson et al. “Genome-wide RNAi screening identifies human proteins with a regulatory function in the early secretory pathway”. *Nature Cell Biology* 14.7 (July 2012), pp. 764–774. doi: 10.1038/ncb2510 (cit. on pp. 86, 97).
- [155] Thorvald Julius Sørensen. *A method of establishing groups of equal amplitude in plant sociology based on similarity of species content and its application to analyses of the vegetation on Danish commons*. København: I kommission hos E. Munksgaard, 1948 (cit. on p. 87).
- [156] Lee R. Dice. “Measures of the Amount of Ecologic Association Between Species”. *Ecology* 26.3 (July 1945), pp. 297–302. doi: 10.2307/1932409 (cit. on p. 87).

-
- [157] Romain Fernandez, Pradeep Das, Vincent Mirabet, Eric Moscardi, Jan Traas, Jean-Luc Verdeil, Grégoire Malandain, and Christophe Godin. “Imaging plant growth in 4D: robust tissue reconstruction and lineageing at cell resolution”. *Nature Methods* 7.7 (July 2010), pp. 547–553. DOI: 10.1038/nmeth.1472 (cit. on p. 87).
- [158] Mike Heilemann, Sebastian van de Linde, Mark Schüttelz, Robert Kasper, Britta Seefeldt, Anindita Mukherjee, Philip Tinnefeld, and Markus Sauer. “Subdiffraction-Resolution Fluorescence Imaging with Conventional Fluorescent Probes”. *Angewandte Chemie International Edition* 47.33 (Aug. 2008), pp. 6172–6176. DOI: 10.1002/anie.200802376 (cit. on p. 87).
- [159] I. Izeddin, J. Boulanger, V. Racine, C. G. Specht, A. Kechkar, D. Nair, A. Triller, D. Choquet, M. Dahan, and J. B. Sibarita. “Wavelet analysis for single molecule localization microscopy”. *Optics Express* 20.3 (Jan. 2012), pp. 2081–2095 (cit. on p. 87).
- [160] Carlas S. Smith, Nikolai Joseph, Bernd Rieger, and Keith A. Lidke. “Fast, single-molecule localization that achieves theoretically minimum uncertainty”. *Nature Methods* 7.5 (May 2010), pp. 373–375. DOI: 10.1038/nmeth.1449 (cit. on p. 87).

Acknowledgements

The work presented in this thesis has been carried out in the Hufnagel group at the European Molecular Biology Laboratory (EMBL) in Heidelberg, Germany. I would like to thank Lars Hufnagel for this unique opportunity to work in the field of microscopy, and for his continuous support through the project.

I am very grateful to the members of my thesis advisory committee: Jonas Ries, Takashi Hiiragi and Balázs Rózsa; thank you for the support and the fruitful discussions.

I would also like to thank Prof. Péter Szolgay for the opportunity to be part of the Roska Tamás Doctoral School of Sciences and Technology at Pázmány Péter Catholic University.

I would like to thank Gustavo Quintas Glasner de Medeiros and Nils Norlin for the microscope building and debugging sessions, and for sharing all their experience and knowledge. A big thank you to Marvin Albert and Joran Deschamps for their help with the compression algorithm, and also for sharing the ups and downs of EMBL PhD life.

Many thanks to all friends and colleagues who helped me throughout my four years: Dimitri Kromm, Ulla-Maj Fiuzza, Li-Ling Yang, Stefan Günther, Lucía Durrieu, Patrick Hoyer, Laura Panavaite, Uroš Kržič, Petr Strnad, Sebastian Streichan, Aldona Nowicka, Christina Besir, Tatjana Schneidt, Judith Reichmann, Yu Lin, Nils Florian Wagner, Christian Tischer; it has been a truly memorable time.

Development of the microscope would not have been possible without the expert help of Alfons Riedinger, Alejandro Gil Ortiz, Leo Burger, Sascha Blättel, Tim Hettinger and all other members of the EMBL electronic and mechanical workshops.

Special thanks goes to Judit Tóth, István Gärtner and Attila Mócsai for introducing me to the world of natural sciences, and Prof. Szabad János for showing me EMBL for the first time.

I am eternally grateful to my parents and my first scientific advisors, Béla Balázs and Ilona Fige, and my sister, Eszter for their unconditional support.

Finally, Melánia: Thank you for your infinite patience, support and love.